AFOSR·TR· 88 - 0 3 1 7

FINAL TECHNICAL REPORT

AD-A192 944

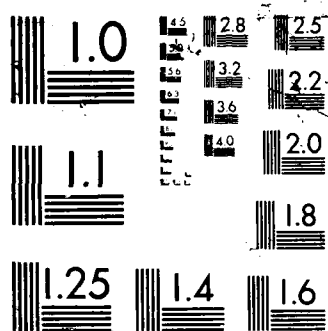"Cloud Simulation Warm Cloud Experiments:

Droplet Growth and Aerosol Scavenging

AFOSR85-0071

DTIC
ELECTE
MAR 3 0 1988

H

D.R. White, D.E. Hagen, and J.C. Carstens

Graduate Center for Cloud Physics Research

University of Missouri at Rolla

Rolla, MO 65401

March 2, 1988

88 3 28 175

AD A192944

REPORT DOCUMENTATION PAGE

1a. REPORT SECURITY CLASSIFICATION UNCLASSIFIED	1b. RESTRICTIVE MARKINGS
2a. SECURITY CLASSIFICATION AUTHORITY	3. DISTRIBUTION / AVAILABILITY OF REPORT
2b. DECLASSIFICATION / DOWNGRADING SCHEDULE	Approved for public release, distribution unlimited

4. PERFORMING ORGANIZATION REPORT NUMBER(S)	5. MONITORING ORGANIZATION REPORT NUMBER(S)
	AFOSR·TR· 88-0317

6a. NAME OF PERFORMING ORGANIZATION University of Missouri	6b. OFFICE SYMBOL (If applicable)	7a. NAME OF MONITORING ORGANIZATION AFOSR/NC

6c. ADDRESS (City, State, and ZIP Code) Rolla, MO 65401	7b. ADDRESS (City, State, and ZIP Code) Bldg 410 Bolling AFB DC 20332-6448

8a. NAME OF FUNDING / SPONSORING ORGANIZATION AFOSR	8b. OFFICE SYMBOL (If applicable) NC	9. PROCUREMENT INSTRUMENT IDENTIFICATION NUMBER AFOSR-85-0071

8c. ADDRESS (City, State, and ZIP Code)
Bldg 410
Boiling AFB DC 20332-6448

10. SOURCE OF FUNDING NUMBERS			
PROGRAM ELEMENT NO.	PROJECT NO.	TASK NO.	WORK UNIT ACCESSION NO.
61102F	2310	A1	

11. TITLE (Include Security Classification)
Cloud Simulation Warm Cloud Experiments: Droplet Growth and Aerosol Scavenging

12. PERSONAL AUTHOR(S)
D.R. White, D.E. Hagen, and J.C. Carstens

13a. TYPE OF REPORT FINAL	13b. TIME COVERED FROM _____ TO _____	14. DATE OF REPORT (Year, Month, Day)	15. PAGE COUNT

16. SUPPLEMENTARY NOTATION

17. COSATI CODES			18. SUBJECT TERMS (Continue on reverse if necessary and identify by block number)
FIELD	GROUP	SUB-GROUP	

19. ABSTRACT (Continue on reverse if ...)
During the research period starting January 1, 1985 and ending December 31, 1987 the following research objectives were achieved: (1) the Proto II facility is operating according to original specifications, including its capability of reaching temperatures sufficiently low (- 36 degrees C) to homogeneously nucleate ice from supercooled water drops; (2) the warm cloud experiments, designed to measure the condensation coefficient of water, have been completed as well as the analysis. It has been found that the condensation coefficient tends to decrease from a value near unity to a significantly low value, .01, as the drop grows from submicron size range to several microns, radius; (3) the problem of chamber humidification, the resolution of which became a major research objective during the course of these investigations, has been solved and we are now able to determine initial relative humidities to required accuracy; (4) the larger Romulus chamber is now producing cloud. The scavenging experiment has not been completed, although considerable progress has been made in its design and implementation. We should be producing results on scavenging by summer 1988.

20. DISTRIBUTION / AVAILABILITY OF ABSTRACT ☒ UNCLASSIFIED/UNLIMITED ☒ SAME AS RPT ☐ DTIC USERS	21. ABSTRACT SECURITY CLASSIFICATION UNCLASSIFIED
22a. NAME OF RESPONSIBLE INDIVIDUAL Lt Col James P. Koermer	22b. TELEPHONE (Include Area Code) (202) 767-4960	22c. OFFICE SYMBOL NC

DD FORM 1473, 84 MAR
83 APR edition may be used until exhausted.
All other editions are obsolete.

TABLE OF CONTENTS

A. REPRINT: White, et al., 1987: University
    of Missouri-Rolla cloud simulation facility:
    Proto II chamber, Rev. Sci. Instrum. 58(5),
    826-834.

B. LIST OF SYMBOLS

C. PREPRINT: Hagen, et al., 1988: Condensation
    method for humidity mesurement in the UMR cloud
    simulation chamber, accepted for publ.
    National Bureau of Standards J.

D. PREPRINT: Hagen, et al., 1988: Hydration
    properties of combustion aerosols, accepted
    for publ. Aerosol Sci. & Tech.

E. Model of drop growth under conditions of
    partial contaminant coverage of drop surface.

DTIC
COPY
INSPECTED
1

I. Summary

During the research period starting January 1, 1985 and ending December 31, 1987 the following research objectives were achieved: (1) the Proto II facility is operating according to original specifications, including its capability of reaching temperatures sufficiently low ($\approx$ -36°C) to homogeneously nucleate ice from supercooled water drops; (2) the warm cloud experiments, designed to measure the condensation coefficient of water, have been completed as well as the analysis. It has been found that the condensation coefficient tends to decrease from a value near unity to a significantly low value, $\approx$.01, as the drop grows from submicron size range to several microns, radius; (3) the problem of chamber humidification, the resolution of which became a major research objective during the course of these investigations, has been solved and we are now able to determine initial relative humidities to required accuracy; (4) the larger Romulus chamber is now producing cloud.

The scavenging experiment has not been completed, although considerable progress has been made in its design and implementation. We should be producing results on scavenging by summer 1988.

II. Research Objectives

The goals of the initially proposed research are as follows:

A. A systematic study of drop growth/evaporation under carefully controlled conditions with the major purpose of determining the values or set of values of the accommodation coefficients of water.

B.   A determination of particulate scavenging efficiency for the phoretic (thermo and diffusiophoresis) mechanism under in-cloud conditions.

There has been some change in emphasis in A. (1) Recent measurements of Sageeve et al. (J. Coll. Int. Sci., 113, 1986, p. 421), have caused us to postpone the separation of condensation and thermal accommodation coefficient. (2) When the research was first proposed we were not sufficiently aware of the pivotal importance of the humidification system. Thus this aspect of the work has not only received added emphasis, but work devoted to it has been regarded as a piece of research in its own right.

III.   Proto II and Romulus Chambers

A.   Proto II.

The proposed research is the first experimental program to be undertaken by the simulation facility. The proposed program was envisioned as providing a series of experiments that would thoroughly test the operating capabilities of the chamber. This purpose has largely been fulfilled with Proto II, and this chamber is currently producing very well controlled cloud, with drop motions suppressed to the point where the cloud sample is normally kept within the viewing volume throughout the experiment. The major problems revealed by these experiments were (1) the unexpected behavior of the humidification system, and (2) the discovery of a problem in the interior thermometer mountings which led to inconsistent dynamic temperature readings (and hence to interior cloud motion that detracted from experiments). Both problems have been solved, the former by an analysis that essentially uses the chamber as a hygrometer (see

Appendix C of this section) and the latter by a careful control of the thermal contact between the thermometers and interior wall.

We were pleasantly surprised to observe the relatively smooth operation of this system below $-35°C$.

Progress made to date on the operational characteristics of this chamber is provided by White et al., "University of Missouri-Rolla Cloud Simulation Facility: Proto II Chamber", Rev. Sci. Instrum., 58(5) which constitutes Appendix A.

B. Romulus.

Progress on the larger "Romulus" chamber has lagged that of Proto II. Indeed Romulus only produced its first cloud in November 1987. The initial experiments planned (summer 1988) for Romulus involve testing the effectiveness of a powerful laser in evaporating "holes" through clouds. This work will be done in collaboration with Las Alamos Laboratory.

Progress made to date on the operational characteristics of the Romulus chamber is provided by the following (unpublished) description which is culled from the UMR Technical Report, "UMR Cloud Simulation Facility".

The Romulus chamber (Fig. 1) is a cooled wall expansion cloud chamber. It is a 12 sided vertical cylinder with a flat to flat internal dimension of approximately 58.4 cm. The chamber is designed with 40.6 cm tall sections and can be operated with any number of sections from a minimum of three (122 cm internal height, Fig. 3) to a maximum of seven (284.5 cm internal height).

The basic concept for the Romulus chamber is similar to that of Proto II. The interior chamber wall surface is cooled (or
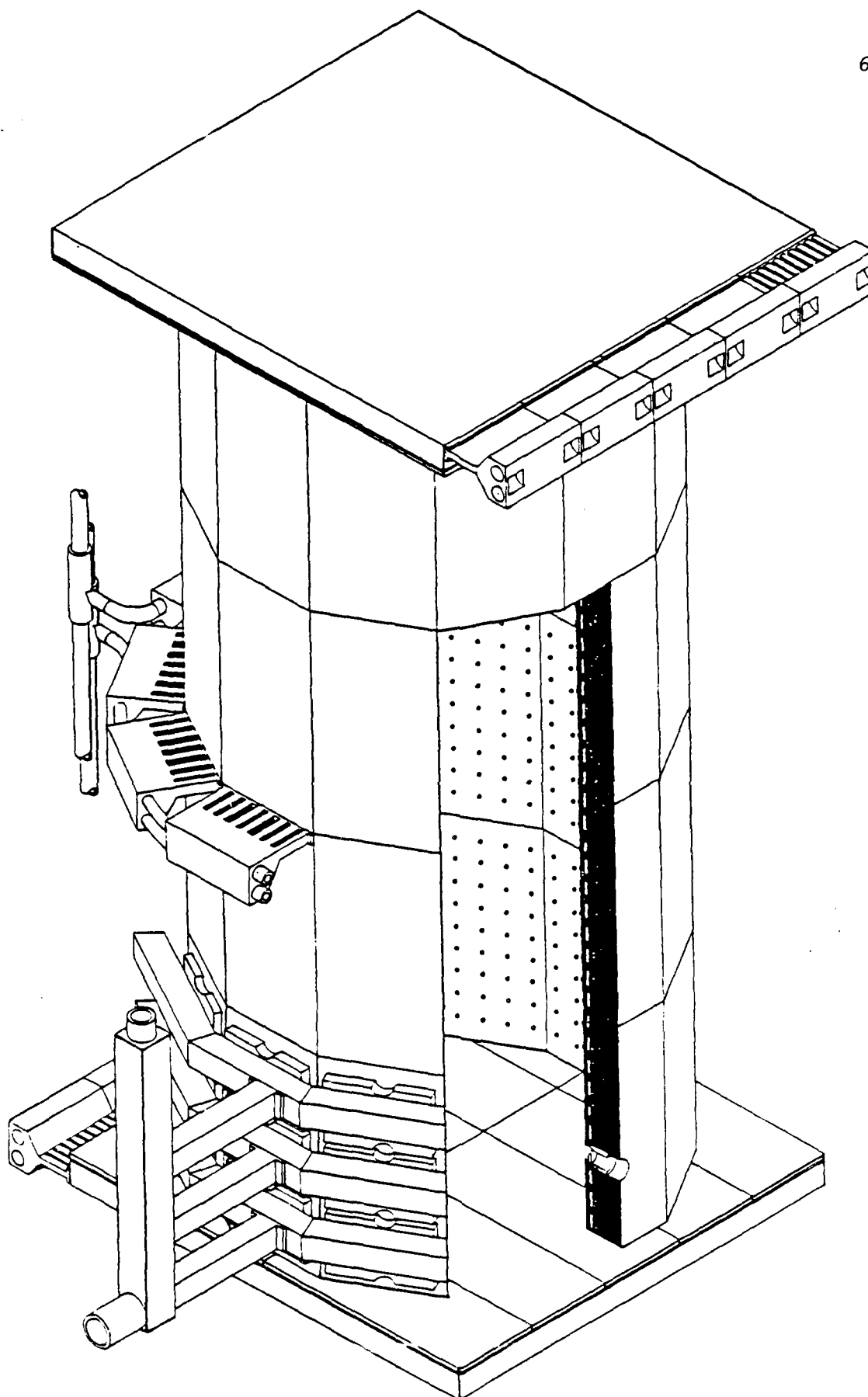
Fig. 1. Romulus Chamber

heated) by TEM's (Thermal Electric Modules, see the description in Appendix A) to provide a continuous temperature match with the expansion cooled (or compression-heated) sample gas in the chamber sensitive volume. A similar inner wall plate and outer liquid thermostated heat sink design (sandwiching the TEM's between them) is used to achieve an operational temperature range of $\pm40°C$.

Improvements over the Proto II design include the improved symmetry of a 12 sided chamber, making the heat sink of each side wall section from a single piece of aluminum for improved ease of sealing and better heat conduction, and a reduction of the area of an individually controlled wall section to 15.25x20.32 cm. The smaller control areas allow an increase in maximum cooling rate from 10°C/min for the Proto II chamber to 15°C/min for Romulus. The increased height will provide longer fall paths for collision studies and increased optical path length, e.g., for light scattering and attenuation studies. The active control has also been changed from analog to digital for increased flexibility of both control and maintenance. It is possible in Romulus to create and accurately control temperature non-uniformities on the walls.

Temperature Measurements

Temperatures are measured with thermometers developed in-house as described in Appendix A (White, et al., 1987).

The Romulus chamber digital control system requires that all of its 400 thermometers be read by the Romulus host computer (DEC PDP 11/23) at least once a second and still have sufficient CPU time for other required control and data acquisition tasks. This

has necessitated a redesign and repackaging of the thermometer electronics to conserve space and to include high speed multiplexing and A/D conversion capabilities. Provision has been made also to eliminate the manual calibration and to perform the required calibration with computer software.

Temperature Control

The digital control system utilizes one PDP 11/23 microcomputer as a host computer for temperature-data acquisition, processing and storage, and overall control of the chamber wall temperature (Fig. 2). The number of control sections can vary between 112 and 208 depending on the number of side wall sections in use. Four LSI 11/23 microcomputers are used as slave computers to interface between the host computer and the individual programmable switching power supplies which power the TEM's in the chamber walls. Each slave computer controls and monitors approximately a quarter of the power supplies. If any of the eight monitored power supply parameters varies outside their established ranges, the controlling slave computer will respond in one of a number of ways: it may merely note the irregularity; it may take direct action to shut down the individual power supplies being affected and notify the host computer of this condition; or it may notify the host computer of the need to turnoff all incoming power.

The temperature of the Romulus heat sink is maintained by a closed loop fluid system circulating the fluid between the chamber heat sink and a 70 kW refrigeration chiller unit. The chiller unit contains a 1900 liter coolant reservoir which can be placed into or removed form the main circulation loop during
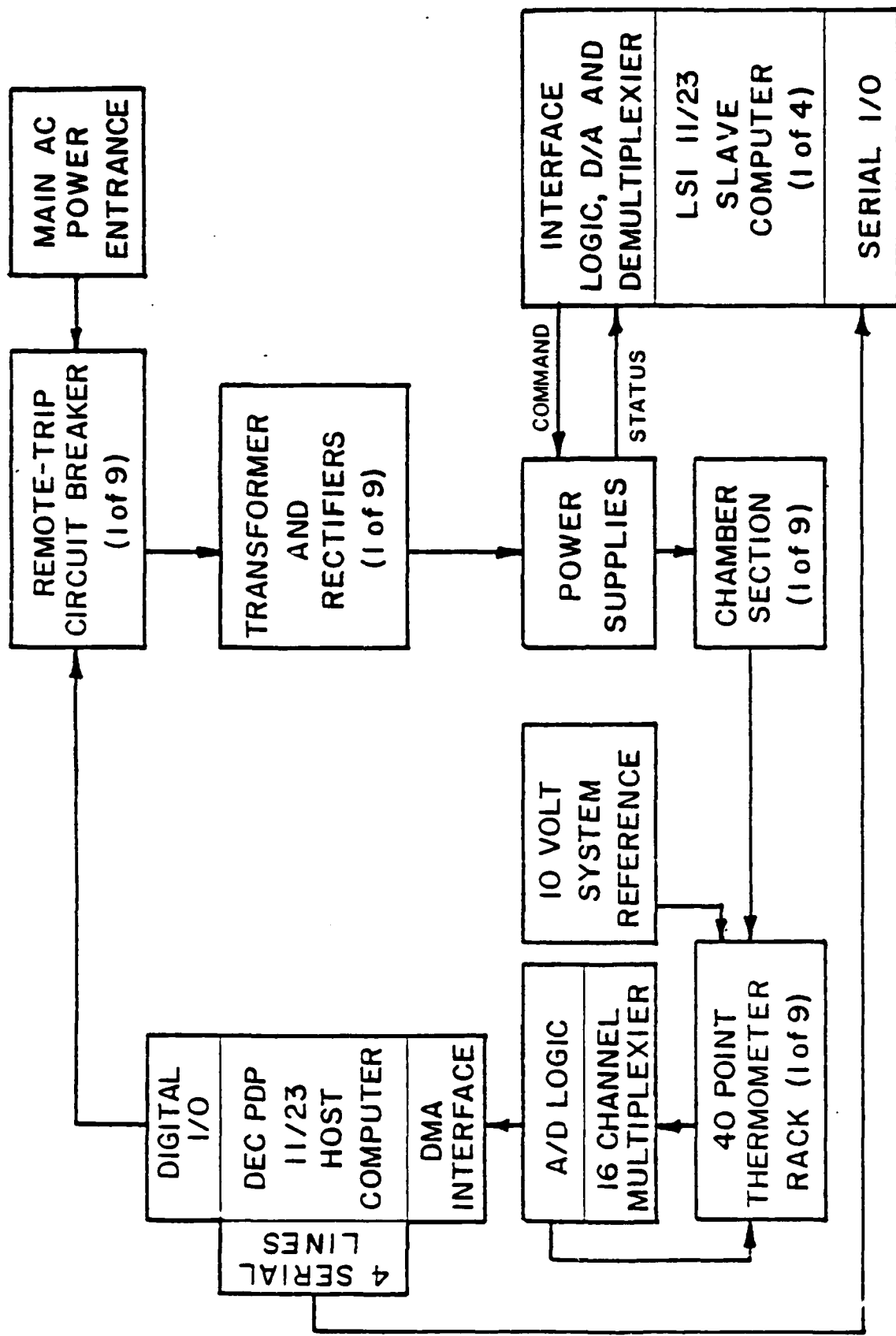
Fig. 2. Romulus Wall Thermometry/Temperature Control System

operation of the Romulus chamber. The reservoir serves two purposes. First, when used as an active part of the main circulation loop, the cooling coils located in the reservoir provide increased heat removal capacity, and the large thermal mass of the reservoir fluid slows the increase in system temperature during periods of rapid chamber cooling when heat production exceeds the design removal rate. Second, when isolated from the main fluid loop, the reservoir fluid can be cooled to a temperature well below that of the heat sink during sample flushing; then after the chamber is closed the sudden addition of a large mass of low temperature fluid to the system causes a rapid cooling of the heat sink during the stilling period. This extends the range of both the maximum cooling rate and the minimum attainable temperature compared to those attained when working against a fixed heat sink temperature. The latter mode of operation is important for large expansions since the temperature of the heat sink must be above the dew or frost point temperature of the sample during the flushing to prevent loss of vapor (in the heat sink) by condensation or freezing. When the reservoir is out of the main fluid loop, heat sink temperature control is provided by a set of cooling coils located in the reservoir bypass line.

The temperature of both the reservoir and the bypass are set by the NOVA 840 control computer. Valves for switching the reservoir into or out of the fluid loop are also controlled for the overall facility operation when either expansion chamber is operating. This, together with the fact that the two chambers share some of the same switching power supplies used for wall

cooling, prevents simultaneous operation of both expansion chambers.

Expansion System

The interior expansion ports of the Romulus chamber are distributed over the entire side wall area. Each 15.25x40.64 cm side wall plate has 36 ports (3.58 mm dia.) in a 4x9 array distributed uniformly over its surface. All of the ports connect to the external surface of the heat sink where they are joined to a common manifold system bolted to the exterior surface of the chamber.

The individual sections of manifold are interconnected horizontally around the chamber and to four external vertical collection pipes equally spaced around the chamber. The vertical collection pipes are connected to the expansion manifold located under the chamber which in turn is connected to the digital expansion control valve. As with the Proto II chamber, the system is designed for balanced flows in the lines so that flow into and out of the sensitive volume will be uniform over the vertical walls.

During expansions the digital control valve is connected to a large mechanical vacuum pump (1500 ℓ/min). The pump is located some distance from the chamber and the 5.08 cm pipe used to connect them also serves as a ballast tank. The Romulus chamber uses the same recompression system as Proto II.

Computer System

The NOVA 840 minicomputer provides overall control and data acquisition for the Romulus chamber (Fig. 3). It provides all the same control and data acquisition functions as described
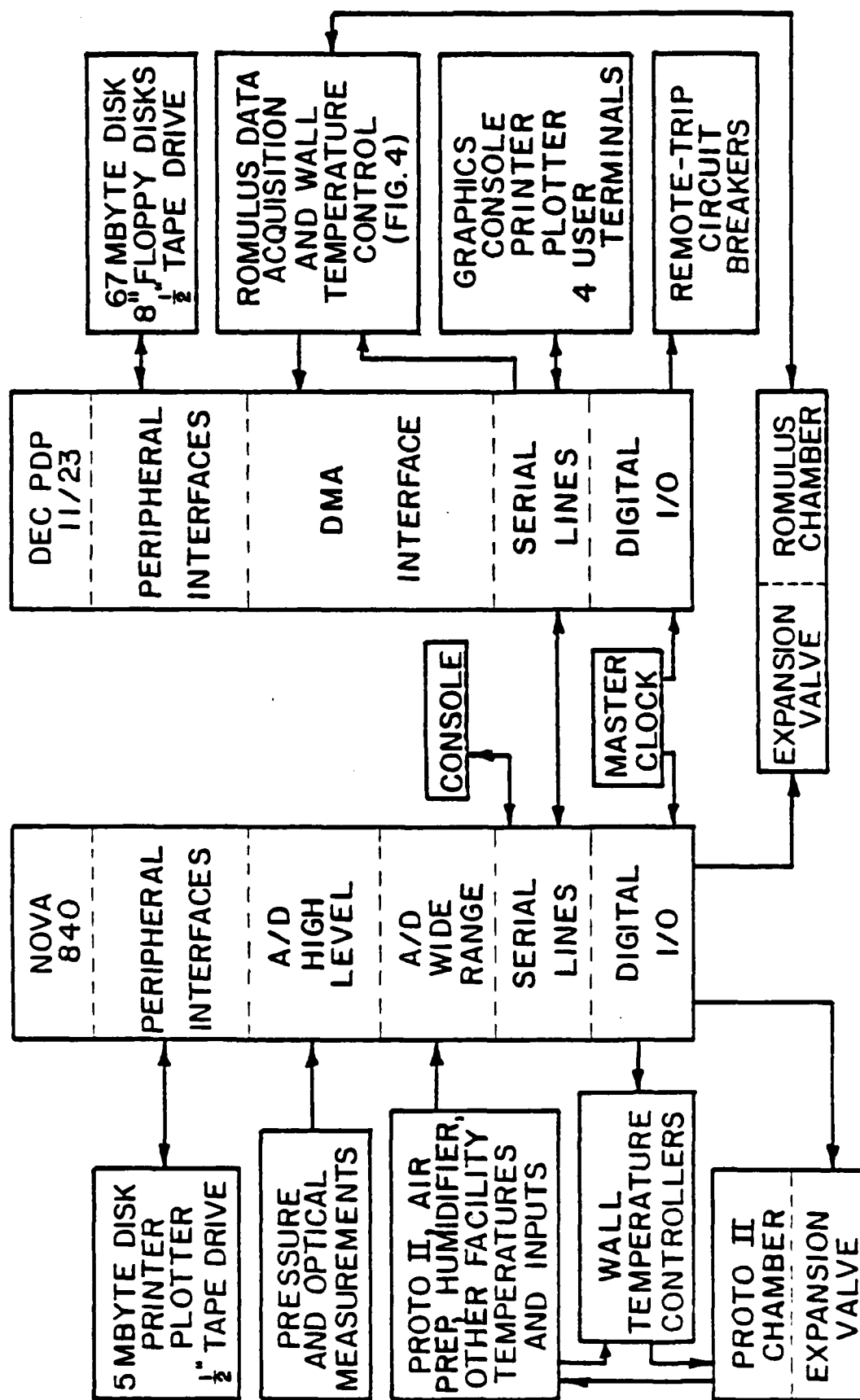
Fig. 3. Data Acquisition and Control System

above with the exception of chamber wall temperature data acquisition and control. Chamber temperature data acquisition and control is performed by a EC PDP 11/23 computer.

Once the operator selects and loads the control profile to be used the temperature portion is transferred by a serial line from the NOVA 840 to the PDP 11/23. At the beginning of the actual expansion, when control passes to the control profile an enable signal is sent from the NOVA 840 to the PDP 11/23. Synchronization by having both computers read the same external elasped time clock.

The PDP 11/23 has a multiuser-multitasking operating system with one megabyte of memory which allows for many concurrent tasks to be in memory at one time. While Fortran 77 is the language of choice for most applications the system also supports Basic, assembler, Modula 2 and C. Assembler is used when communicating with non-standard interfaces or for time-critical functions.

Chamber Flushing

Sample flushing in the Romulus chamber utilizes its expansion system. A flow of sample air from the preparation system enters the inlet manifold above the chamber which is connected to the four external vertical collection lines of the expansion system. During sample flushing the four expansion lines are closed by one set of valves just below their connections to the top side wall section and a second set just above the connections to the bottom side wall section. With these valves close, the sample flows from the inlet manifold down the expansion lines to the top side wall section and into the chamber through the expansion system.

The sample then flows through the chamber sensitive volume and out to the external expansion lines through the expansion system in the bottom side wall section. The lower ends of the external expansion lines are located under the simulation chamber, which during chamber flushing is open to the exhaust line.

Update on Romulus

The chamber currently (February 1988) consists of three rings and the top and bottom plates. There are 112 control points run by 3 slave computers, five racks of thermometers and one central data acquisition (host) computer. The remaining six thermometer racks and the fourth control (slave) computer are constructed and will be employed in the system as the need arises.

As designed, the desired wall temperature will come from a table of time, pressure, and temperature values downloaded prior to the experiment from the Nova 840. Synchronization of the two machines will be accomplished by a common real time clock. The table of values is presently used by the Nova to control Proto II chamber pressure and send the desired wall temperature to the analog controllers via a D/A output channel. This Nova output channel has been routed to the Romulus host computer A/D input where it is read and used as the desired wall temperature. By using the Nova's D/A output as input to the 11/23's data acquisition system the present Nova software (with only minor modifications) can be used to drive either chamber. Since this occurs in real time it also serves to synchronize the two machines.

The system software is designed to provide a great deal of flexibility. An ASCII configuration file has been implemented

that completely describes the desired system. It can be changed quickly to reflect the current interconnect state of the control system. The file associates a particular power supply with the correct slave computer and wall temperature thermometer and provides a means to turn on or off control to individual wall plates. At present the control system implements a simple proportional control algorithm with a gain of about 10. Not surprisingly this system exhibits large (.2C) steadystae errors and dynamic errors with 1/T inputs on the order of 1.5C. On the other hand this system is unconditionally stable and gives us a reliable means of verifying the operaion of the rest of the chamber. As the need for more critical control becomes apparent the software can be modified to accommodate control algorithms with varying degrees of sophistication and optimized for a particular temperature regime or profile.

The performance of the Romulus chamber is as good or better than predicted by design data. So far the power supply output has been constrained by the software to be 1/2 the available voltage. Thus only 1/4 of the total power is available or about 30,000 watts. At this power level the control system is able to follow a standard 10 degree/min. ramp for 60 seconds and open loop can generate an almost 20C difference from heatsink and about 12C/min. cooling rate. As the power constraints are relaxed system performance will easily reach 15C/min. ramp rate with almost 40C differene from heat sink.

IV. WARM CLOUD EXPERIMENTS: CONDENSATION COEFFICIENT.

This section constitutes a record of progress made (as well as a status report) on the measurement of the condensation coefficient. With minor alterations it will form the core of an article to be submitted (probably March 1988) to the Journal of Atmospheric Sciences.

A. Experimental overview.

All the experiments described herein were conducted in the Proto II chamber, and all measurements were made on a monodispersed cloud, formed by nucleating on a monodisperse NaCl aerosol.

The cloud forms when the sample of moist aerosol laden air experiences a supersaturation due to a controlled isentropic expansion. Further cloud growth or evaporation is induced through further expansion or compression. The cloud drop size as a function of time is measured. The corresponding droplet growth rate is compared with growth theory to evaluate a condensation coefficient, β. Two different types of profiles are employed: (1) a 'ramp' profile in which a 10°C/min cooling rate is initiated and then held constant; and (2) an 'oscillating' profile produced by a series of expansion/compressions which repeatedly form and then evaporate the cloud. A ramp expansion produces an especially well-controlled temperature and pressure profile which allows the tracking of droplet growth to large drop sizes (about 12 μm radius). An oscillating expansion allows repeated drop growth measurements on the same sample of droplets, for the study of memory effects.

B. Monodispersed Clouds

The reason for using a monodispersed cloud is the need to make precision drop size vs. time measurements. The results from monodispersed clouds can be combined to simulate any polydispersed system, and one can readily measure the size of drops in a monodispersed system. The method for this latter measurement is to observe the characteristic Mie theory maxima and minima of light scattering from the cloud droplets. This technique does not permit us to <u>directly</u> observe size spectrum evolution, but involves <u>all</u> the relevant physics of the cloud-growth process in the condensation regime. Both chamber and atmospheric drop populations are always sufficiently low that the only "interaction" among drops takes place through their commonly experienced (ambient) vapor pressure and temperature fields, where each growing drop contributes to a uniform decrease in ambient supersaturation. All of the physics is tied up in the droplet growth rate as a function of drop size, temperature, pressure, and supersaturation. Once this is known from monodisperse experiments, the condensational behavior of polydisperse clouds can be accurately predicted. Monodispersed clouds are obtained by starting with a monodispersed aerosol (NaCl) and subjecting the sample to a fast expansion when the supersaturation is near 100%. When this is done, all of the CCN activate at about the same time and grow in a similar manner. Our aerosol system produces a quite monodisperse aerosol through the use of a four-furnace aerosol generator (White, et al., 1987; Alofs, et al., 1979) followed by electric mobility size classification. The geometric standard deviation of the aerosol size distribution is usually 10% of the mean size. All of our

experiments are designed such that the expansion rate was
10°C/min when the sample crossed through S (supersaturation
ratio) = 1. During the subsequent growth, the droplet size
distribution becomes more monodispersed since, as is well known,
diffusively controlled condensational growth naturally sharpens
the size distribution. We estimate from the sharpness of the Mie
scattering peaks (see below) that the drops are routinely
monodispersed to within 0.1 μm.

C. Introduction of the aerosol.

The aerosol is introduced into the middle of the flow of
clean moist air supplied by the humidifier system. The (humid
air flow)/(aerosol air flow) ratio is adjusted to produce an
aerosol concentration in the simulation chamber between 25 and
150 particles per cubic centimeter and is always kept at values
greater than 100:1. The aerosol concentration in the simulation
chamber during the flushing period is determined by withdrawing a
continuous sample from the chamber and measuring the total
aerosol concentration with the alternate gradient continuous flow
diffusion chamber (AGCFD). The chamber is flushed with a sample
flow from top to bottom for at least 15 minutes or until a stable
usable aerosol concentration is measured for 5 minutes. At that
time the appropriate (for the measured aerosol concentration)
computer control profile is selected for use and the chamber
inlet and outlet valves closed. Once the inlet and outlet valves
are closed the pressure control is activated and a slow
isothermal compression or expansion brings the chamber to the
required starting pressure of 972.2 mb. The wall temperature

control has been operating before the sample flush and holds the walls constant at the desired initial temperature.

D. Preparation of humidified air.

Air for the experiments is taken from outside the laboratory building at a flow rate of approximately 1 l/s. The air is dried by both refrigeration and desiccant driers and filtered with both particle and activated charcoal filters (White, et al, 1987). The resulting clean dry air is then passed through a precision flowing water humidifier (White, et al., 1987; Hagen, et al., 1988) to establish a known water vapor content. The aerosol is then added at the output of the humidifier.

E. Humidity measurement.

The relative humidity in the simulation chamber prior to expansion is a key parameter in virtually any experiment since it controls the humidity at all later points in the experiment. In this work the cloud chamber itself is used as a condensation type hygrometer to calibrate the humidifier to an precision of one part per thousand in mixing ratio (Appendix C, Hagen, et al., 1988, JNBS). Two distinct methods are employed. One is based on multiple measurement of droplet growth rate; the other is based on the fact that cloud is observable almost immediately after the gas sample is brought through 100% relative humidity. In the former method the influence of the condensation coefficient is eliminated by using the fact that the initial mixing ratio is a constant. In the latter method the condensation coefficient enters only as a minor correction. The two methods agree well. The average difference in calculated initial mixing ratio is 1×10^{-5} grams of water per gram of dry air (corresponding to

about 8 parts in 10^4), with a standard deviation of 0.7×10^{-5} grams/gram-air. This corresponds to a dew point difference of $0.012°C$ at $17°C$. This is a state-of-the-art humidity measurement. For comparison, the manufacturer's claimed accuracy for a commercial humidity measurement device, the Cambridge Systems dew point hygrometer model 992, is about plus or minus $1°F$. As will be discussed later, our small uncertainty in mixing ratio does lead to the largest experimental uncertainty in the condensation coefficient.

F. Cloud observations: motion in the viewing volume.

Conditions in the central volume of the simulation chamber are monitored using a low light level video camera capable of detecting individual drops with radii of $2.5 \mu m$ and larger. Illumination is by the laser beam used for the $4°$ forward Mie scattering system which also measures the average drop radius as a function of time. The video camera is located at the chamber window at $72°$ from the forward direction of the laser beam and views a horizontal cylindrical volume in the center of the chamber approximately 2 cm in diameter and 6 cm long. The volume observed by the video camera and the Mie scattering volume are approximately coincident. Visual observation of the clouds shows the droplets to be either stationary or moving together (1 to 2 cm/s) in a uniform organized manner during the time interval for which Mie scattering data can be interpreted. Experience has shown that the degree to which the cloud droplets are stationary is closely related to the accuracy with which the computer control profile matches the actual chamber conditions. The gas and wall temperatures must be matched to better than a tenth of a

degree Centigrade in order to suppress convection. Our gas
pressure and temperature control profiles are calculated in
advance of the experiment using the a numerical cloud model
(Hagen, 1979). Since the condensation coefficient, β, exerts some
control over the release of latent heat of condensation, which
largely determines the temperature, a good knowledge of β is a
prerequisite for performing the experiment. We accomplished the
task of measuring β in an experiment in which a knowledge of β
was a pre-requisite, by repeating the experiment many times. At
each repetition our knowledge of β improved, and with it our
chamber control. Since the influence of β enters into the
control scheme only through latent heat release, its influence is
felt only towards the latter part of the experiment when the
drops are several microns in size. During the early experiments
our knowledge of β was relatively poor, and convection interfered
with the measurements relatively early. As our knowledge of β
improved, convection could be suppressed longer, and measurements
could be extended to larger drop sizes. The results shown here
are based on our best estimates of β, which did prove sufficient
to suppress convection. The suppression of convection gives
evidence that our cloud model, using the condensation coefficient
shown here, did satisfactorily track the growth of the cloud
drops.

G. Measurement of drop radius vs. time.

The size of the drops as a function of time are measured by
analysis of Mie light scattering at 4° from the forward
direction. Illumination for the 4° Mie scattering system is
provided by the beam-expanded 488 nm line of an argon-ion CW

laser. The beam is expanded to a diameter of approximately 1.5 cm and enters through one of the three chamber windows. As the beam enters the chamber it passes through an optical wedge which deflects it upward at an angle of 2°. The photomultiplier tube detector views the center of the chamber through an identical optical wedge, located in the chamber window directly opposite the laser entrance window, which deflects its viewing direction up by 2°. This results in the photomultiplier tube receiving light which has been scattered at approximately 4° from the forward direction by a small volume of droplets in the center of the simulation chamber. A pin-hole aperture in front of a photomultiplier tube restricts the acceptance angle of scattered light to a 1° viewing angle which intersects the laser beam in the center of the chamber. The output of the photomultiplier tube is amplified and recorded on a photographic paper oscillograph (D.C. to 5 KHz response). Prior to the beginning of the cloud formation, but after the recorder has started, a computer controlled shutter is closed in front of the photomultiplier tube to provide an absolute correlation between the recorder time and the computer time. A second recorder channel records a bilevel signal which changes state with each update of the pressure control system. The computer also records the times of each pressure control update and these times together with the shutter time are used to synchronize the recorder trace with the computer time.

Trace analysis. A plot of the Mie scattering intensity as a function of droplet size for scattering angles around 4° provides a very distinct system of peaks and valleys. A sample scattering

intensity vs. droplet size plot is shown in Fig. 4. Correlation of droplet size and scattering intensity was made only for the local maxima and minima of the recorded intensity vs. time trace. Computer computations of the scattering intensity vs. droplet radius have been plotted for scattering angles between 3.0° and 5.0° at 0.25° intervals. The intensity was integrated over a 1° acceptance angle to duplicate the optics of the photomultiplier tube. Study of these plots show local extrema with frequencies of 2 to 4 per micron of droplet radius with a slower modulation of the maxima with a period of 3 to 4 micron. It is the changes in the locations (with respect to drop size) of the minima in the slower modulation, which permit traces from the growth of droplets to be used to determine the actual scattering angle as opposed to the extremely difficult task of physically measuring it. Experience has shown that the scattering angle changes only when adjustments have been made on the optical system; however, the angle is checked as part of the start-up procedure for each day of data taking.

Once the scattering angle has been determined, the appropriate computer-generated plot is used to determine the corresponding droplet radius for each of the local extrema. The light beam recorder trace combined with the computer recorded time of the shutter closing, which produces a very distinct offset in the trace when the background light is cut off is used to establish an absolute time on the trace. From there the time of the next pressure update trace state change is determined and the times of succeeding state changes are determined by making a one to one correlation between state changes and the computer
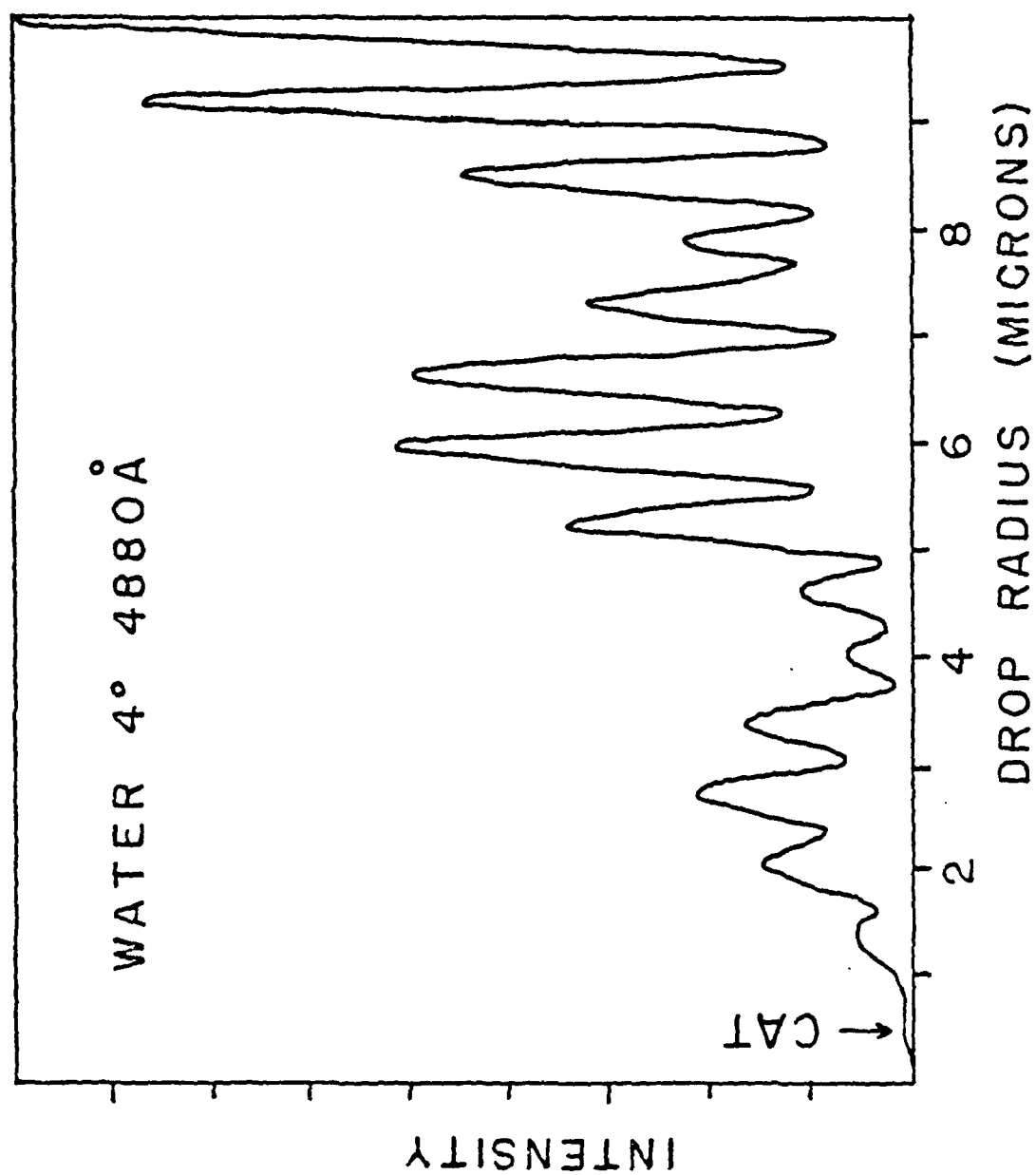
Fig. 4. Light scattering intensity vs. drop radius as
calculated via Mie theory for water and 4° from
the forward scattering angle.

recorded pressure update times. By interpolation between known times on the trace the corresponding computer time is determined for each of the local extrema of the scattering intensity trace.

H. Theoretical relations used to determine condensation coefficient.

Condensational droplet growth theory as developed by Carstens (1979) and discussed by Hagen (1979) is used in the analysis of this data. In this analysis we invoke the common assumption that the thermal accommodation coefficient is unity, and the condensation coefficient (β) is the one and only experimental unknown. Two different implementations of the theory are employed depending on whether or not the driving supersaturation is high enough to lead to a significant difference between the ambient gas temperature and the cloud drop temperature. For experiments in the cloud simulation chamber, all of which are done at relatively low supersaturations (usually the maximum supersaturation is around 5 or 6%), the difference between the ambient temperature and that of the drop is slight enough that the saturation vapor pressure may be inferred, with acceptable accuracy, by a linear fit spanning these two temperatures. For this simple case, the droplet growth theory (Carstens, 1979) can be algebraically inverted to give β as a function of growth rate:

$$\beta = \frac{s_1}{\dfrac{r_0 - s_3}{r_0 + (1 - s_3)} - s_2}$$

where

$$s_1 = e_{eq}(T) \; \dot{a} \; CD_{eff}/pg \; \sqrt{\bar{T}}$$

$$s_2 = e_{eq}(T) \; \dot{a} \; D_{eff}(\ell_\alpha B\theta_p - C/2T^{1/2})/pg + e_{eq}(S_c + a \; \dot{a}/g)/p$$

$$s_3 = \frac{4\pi}{3} \; Na^3/\epsilon$$

$$g = D_{eff} \; \rho_s$$

$$C = \sqrt{2\pi M_v/R}$$

$$\theta_p = M_v L/KRT$$

$$\frac{1}{D_{eff}} \; \frac{1}{D} + \frac{BL}{KRT_a}$$

$$\ell_\alpha = \frac{16K \; (\frac{\gamma-1}{\gamma+1})}{\alpha \; n(T_a)(\frac{8RT_a}{\pi M_a})^{1/2}R}$$

(See Appendix B for a list of symbols.)

For the case of high supersaturations such as those encountered in the piston-driven fast expansion chambers, the linearization technique (valid for low, in-cloud, supersaturations) must be abandoned. Here the inversion of the droplet growth equations to find β cannot be done algebraically due to the dependence of the drop temperature on β. The inversion must be done numerically.

I. Comparison with other drop growth theories.

The model used for our analysis, (Carstens, 1979), has been successfully tested against older results in the literature (Hagen, 1979) and against the NASA Analytic Simulator (Plooster, 1979). Anderson, Hallett, and Beesley (1981) presented an extended solution to the droplet growth problem and intercompared the leading theories. They concluded that Carsten's (1979) solution of the droplet growth problem produced valid results. This is the formalism on which our cloud model is based. Furthermore Anderson, et. al. (1981) presented numerical results from their extended model for numerous test cases. We re-calculated these cases with our model and agree with their results to within 2% for drop size. Note that in this application only the differential form of droplet growth theory is used. Theory is also used to provide a value for the instantaneous growth rate for a given environmental condition (temperature, pressure, and supersaturation). Integration of the droplet growth equations over time, as is done in a full cloud model, is not required or used here.

J. Determination of temperature, pressure, and supersaturation.

In this condensation coefficient analysis there is no integration of droplet growth equations. Since the drop size a(t) is directly measured via Mie light scattering. The pressure p(t) is also directly measured via a wide bandwidth pressure transducer. The temperature T(t) is calculated from the first law of thermodynamics, assuming an isentropic expansion, from the measured p(t) and a(t) profiles and the initial value of temperature, T_o. From these measured parameters, the supersaturation can be directly calculated (Hagen, 1979):

$$S = [p/e_{eq}(T)]/(1+\epsilon/r),$$

where r denotes the current mixing ratio as determined from the initial mixing ratio, drop concentration and current drop size.

K. <u>Temperature and pressure profiles</u>.

Figure 5 shows the temperature and pressure as functions of time profiles for a ramp expansion. After a short start-up period the temperature falls at a constant rate of 10°/min. With this profile the cloud forms, its growth is observed, and the experiment ends when control prediction errors lead to a temperature mismatch between the gas and walls which induces cloud non-uniformities and convection. Typically the cloud can be measured to a size of 12 to 15 micron radius. Figure 6 shows profiles for an oscillating expansion. For this latter profile we get cloud formation followed by evaporation for each of the cycles. The last cycle does not turn around into a compression, but rather continues into a standard 10°C/min ramp. Note that the first cycle is not as deep as the subsequent ones. After experimentation we discovered that the cloud drops grow much more rapidly during the first expansion, and so we reduced its depth to grow the drops to about the same size on each cycle. With this type of expansion profile it is possible to study repeated droplet growth behavior on fresh vs. aged cloud drops, using the same CCN-gas sample.

L. <u>Results</u>.

<u>Ramp experiments</u>. These use the profiles shown in Fig. 5. In these experiments a number of runs were done on the same day, and the results are superimposed on the same graph. In this way
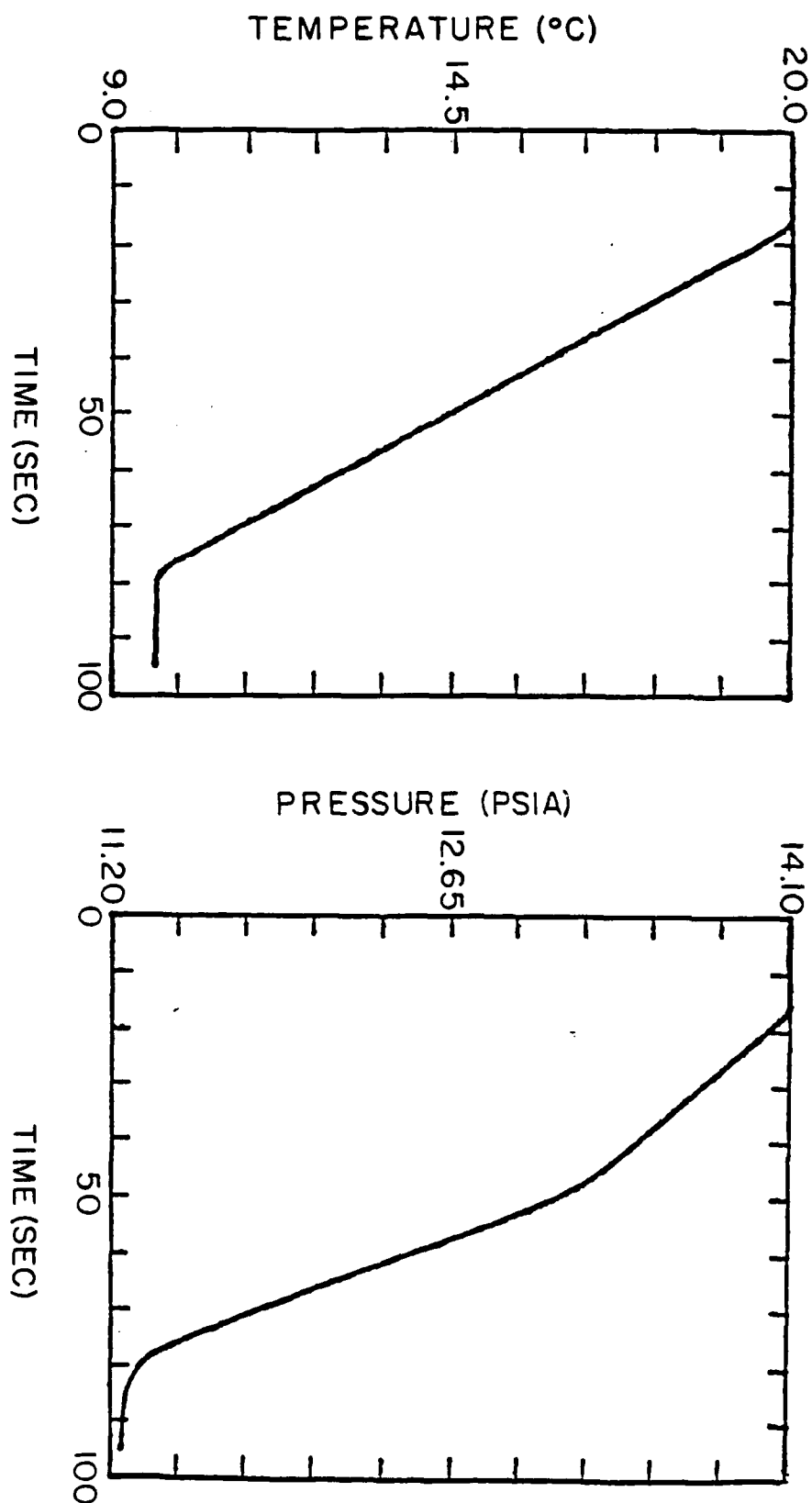
Fig. 5. Expansion chamber temperature (a)
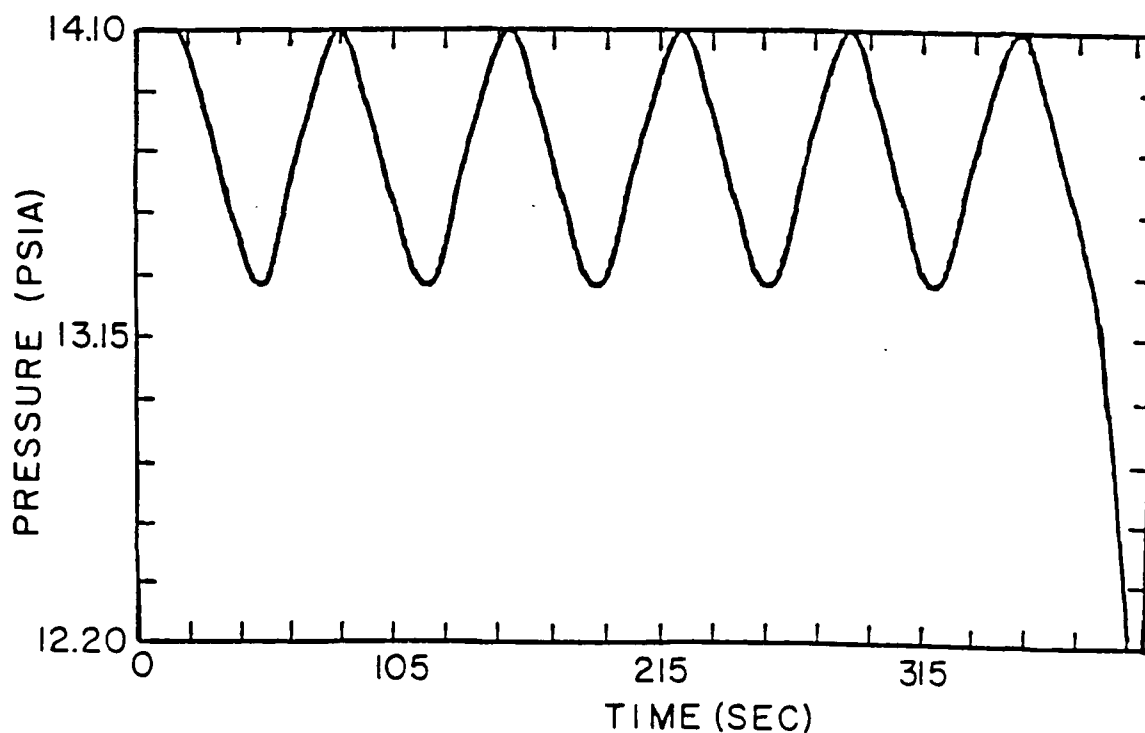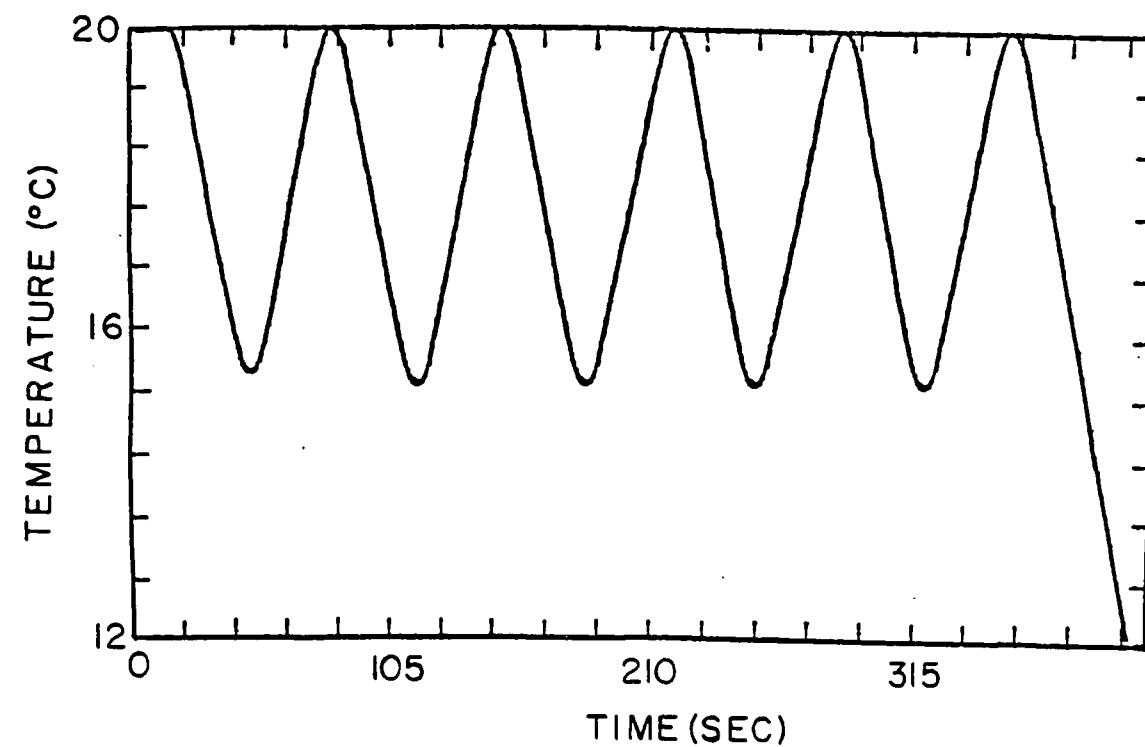and pressure (b) vs. time profiles
for 'ramp' expansions.

Fig. 6. Expansion chamber temperature (a) and pressure
(b) vs. time profiles for 'oscillating' expansions.

experimental noise is averaged out and the trends in the data are most apparent. The condensation coefficient, β, is inferred from measured droplet growth. Because growth can be repeatedly determined throughout the course of the experiment, so too can β be repeatedly determined from each growth rate value. We find that β changes with time. It is found useful to plot β vs. droplet size, a, not because we expect an explicit β vs. a dependence, but rather because drop radius reflects the duration of the imposed driving force experienced by the growing drops. Plots for three sets of experiments are shown in Figs. 7,8,9. Each figure represents a superposition of the results from one day's experiments, using $10°C/min$ ramps. Several features stand out in the graphs. The results at large β exhibit a relatively large amount of scatter. This is a consequence of the fact that when β is large, it has only a small effect on droplet growth. Hence small errors in growth rate translate into very large errors in β. β is seen to start out near unity for fresh drops (i.e., drops which have not been previously activated). This is an expected result for pure water drops with fresh surfaces (Pruppacher and Klett, 1978; Cammenga, 1980). Now as the drop grows (ages) β begins to decrease significantly. Near the end of the experiment β is near 0.01. This is sufficiently small for β to have significant atmospheric implications. Here we have shown three sets (days' of experiments; numerous other ramp experiment data sets exhibit the same trends.

Similar experiments were performed in a completely different cloud chamber facility, a piston type expansion cloud chamber (Schmitt, 1981). Here the expansion is much faster than in the

Fig. 7.   Superposition of condensation coefficient, β, vs.
cloud drop size, a, for cloud simulation chamber
experiment series 091086.
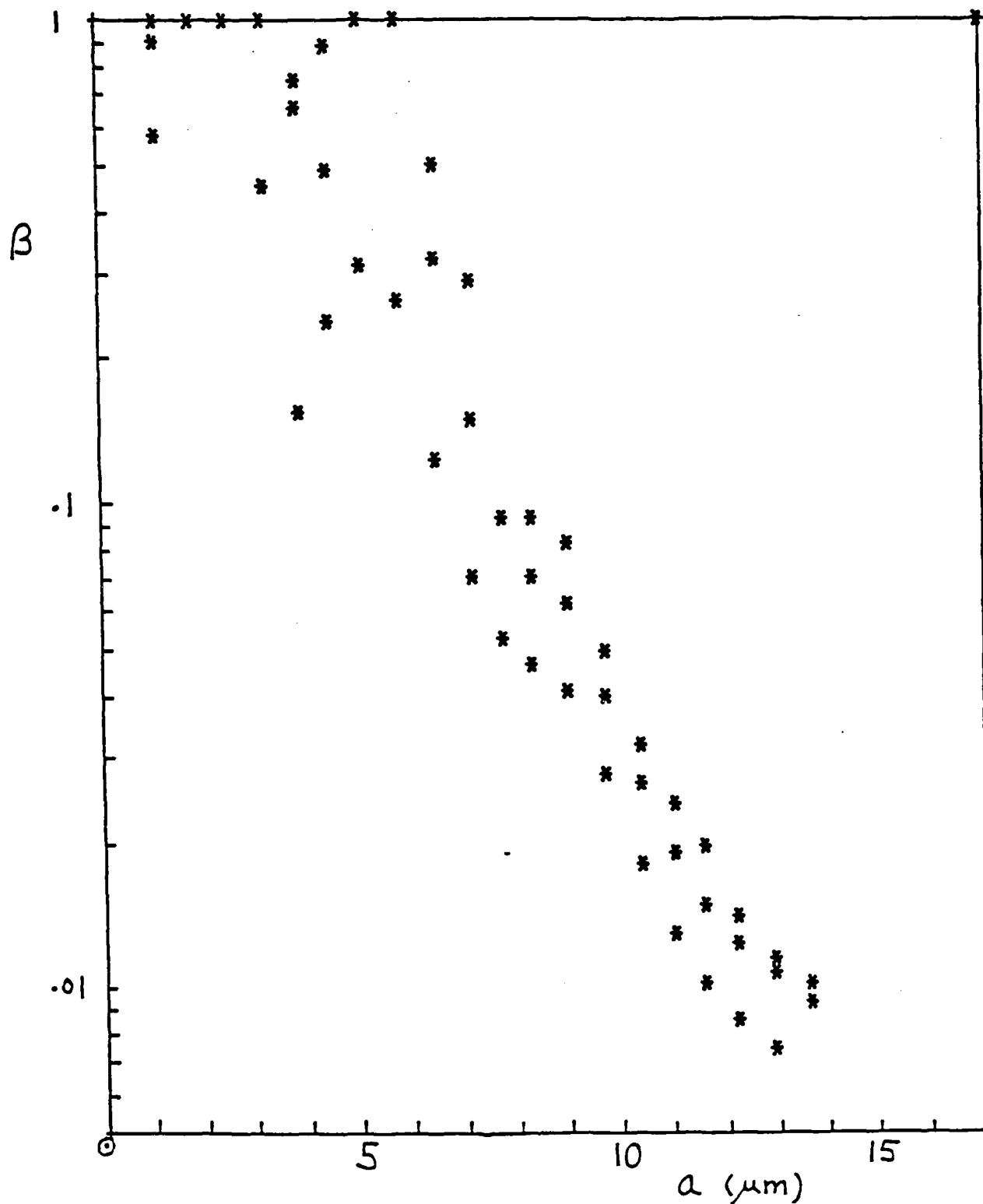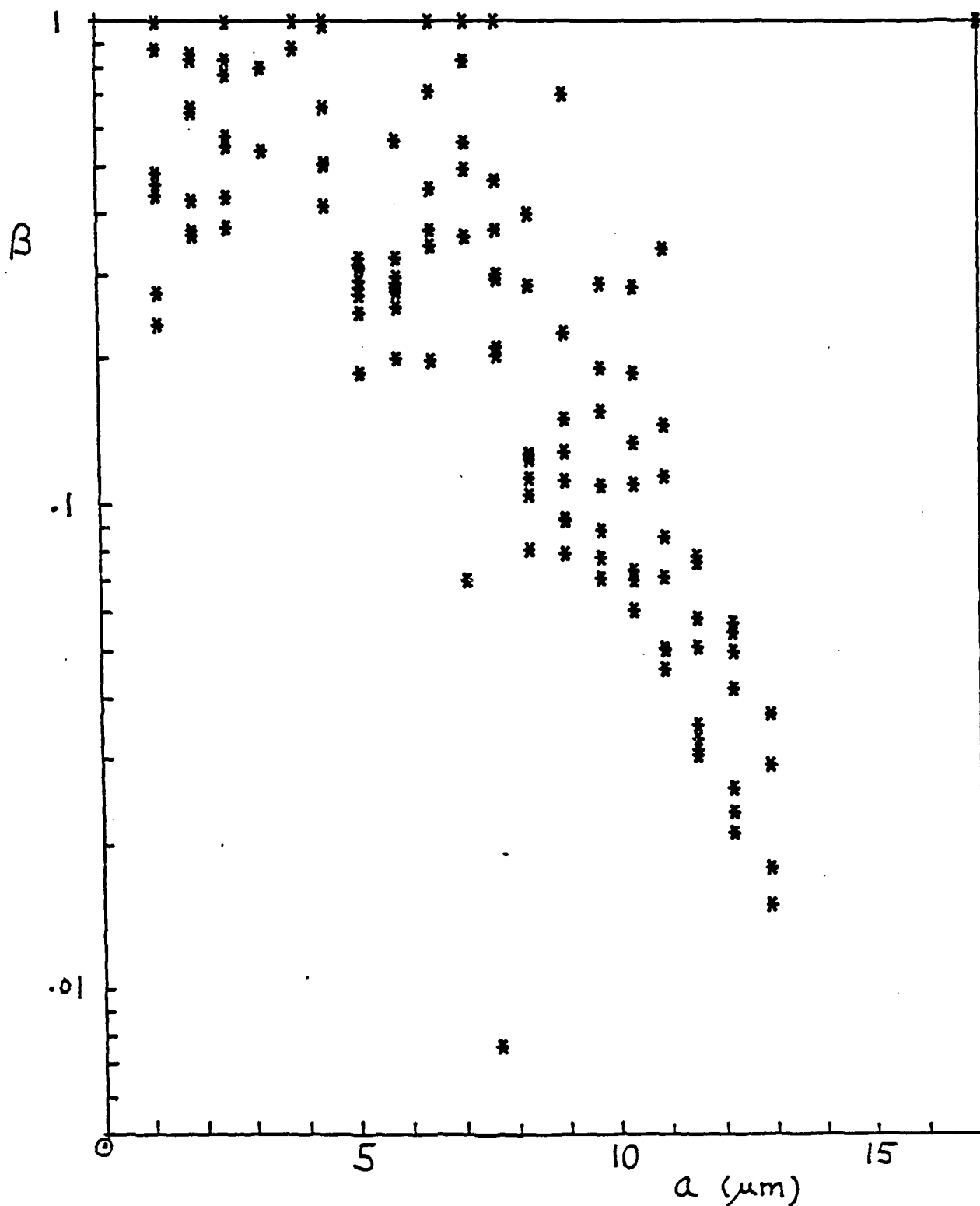
Fig. 8.   Superposition of condensation coefficient, β, vs.
           cloud drop size, a, for cloud simulation chamber
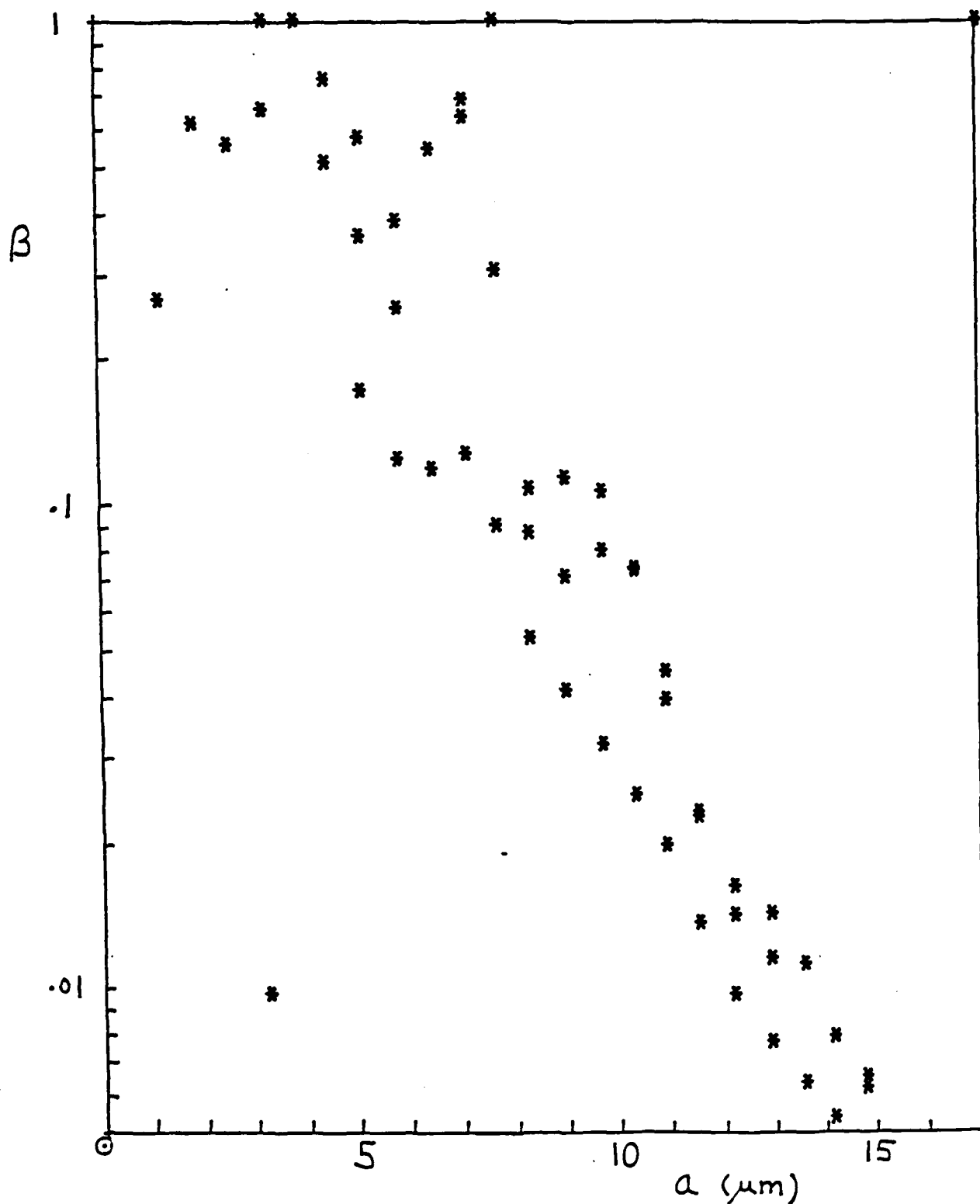   experiment series 121786.

Fig. 9.   Superposition of condensation coefficient, β, vs.
          cloud drop size, a, for cloud simulation chamber
          experiment series 111886.

cloud simulation chamber, the cycle lasting only on the order of a few seconds. Droplet growth rate measurements are made for a few seconds following the expansion. Any condensation nuclei can be removed from this chamber by nucleating on them at supersaturations slightly less than that required for homogeneous nucleation (e.g., 400-500% relative humidity). The subsequent homogeneously nucleated drops are then pure water and their growth is observed via Mie scattering. Results for one typical experiment are shown in Fig. 10, for the growth of homogeneously nucleated water drops in argon. The results are strikingly similar to those from the cloud simulation chamber which operates on a much slower time scale. β starts off near unity and then falls off as the droplet grows. A striking feature of this fast expansion chamber is its cleanliness. The drops are homogeneously nucleated so there is no CCN aerosol required in the system. Chamber surfaces are Teflon, stainless steel, and glass and can be rigorously cleaned. Data were taken with this chamber before and after a thorough cleaning with an extended application of reagent grade acetone followed by vacuum evaporation. Data taken after the cleaning is shown in Fig. 10. Data taken before the cleaning looks similar to that in Fig. 10 but it converges to about $\beta=0.2$ in the small drop size limit, suggesting that contaminants can indeed lower the value of β.

Other drop growth data is available from Wagner (1982), again for homogeneously nucleated droplets in a high speed piston expansion cloud chamber. This expansion chamber operates on a very short time scale; it is roughly a factor ten faster than the expansion chamber (Schmitt, 1981) at the University of Missouri
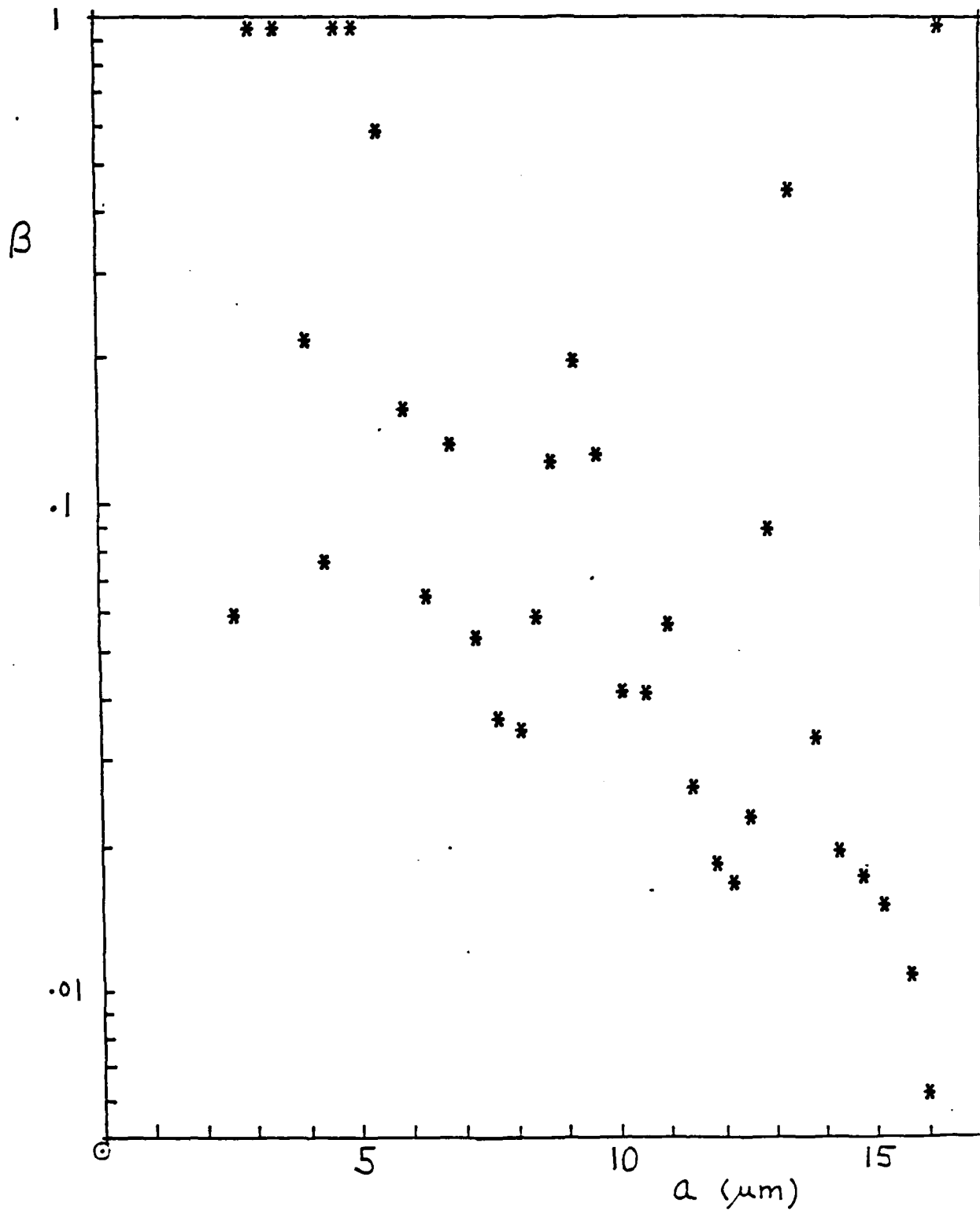
SCH122486.43

Fig. 10.   Condensation coefficient, β, vs. cloud drop size,
a, for fast piston expansion chamber experiment
121486.

discussed above. Three experiments were presented (Wagner, 1982). Wagner followed the common approach of fitting one value of β to an entire data set, rather than allowing it to change its value during the course of an experiment. He found $\beta=1$ to give the best fit. We reanalyzed the data using our method which gives a β value for each drop size measurement point. In two of his experiments, those with the highest expansion rates and shortest durations, we also find $\beta=1$ for all points. In the last experiment with the slowest expansion rate and longest duration, we find $\beta=1$ for the early points, and then found β to fall off reaching $\beta=.06$ for the latter points. This indicates that the same trend for β (to begin near unity for fresh drops and then fall off with time) is observed in another completely different cloud chamber system.

Our next experiments are those using the oscillating profiles shown in Fig. 6. Here the sample is subjected to repeated cloud growth and evaporation cycles. Fig. 11 shows results for the first two cloud forming phases of a particular oscillating experiment (run 080787.03). These results are typical. The *-points show results for the first growth period, and the o-points show them for the second growth period. During the first growth period, β starts off near unity and then falls. During the second growth period, β starts off near the β value where the first expansion left off, and then decreases from there. This behavior is typical and was reported earlier (Hagen, et al., 1986, Snowmass). The droplets are "changed" during the first cloud forming experience, their β is lowered, and they do not recover their fresh-drop properties when they are evaporated.
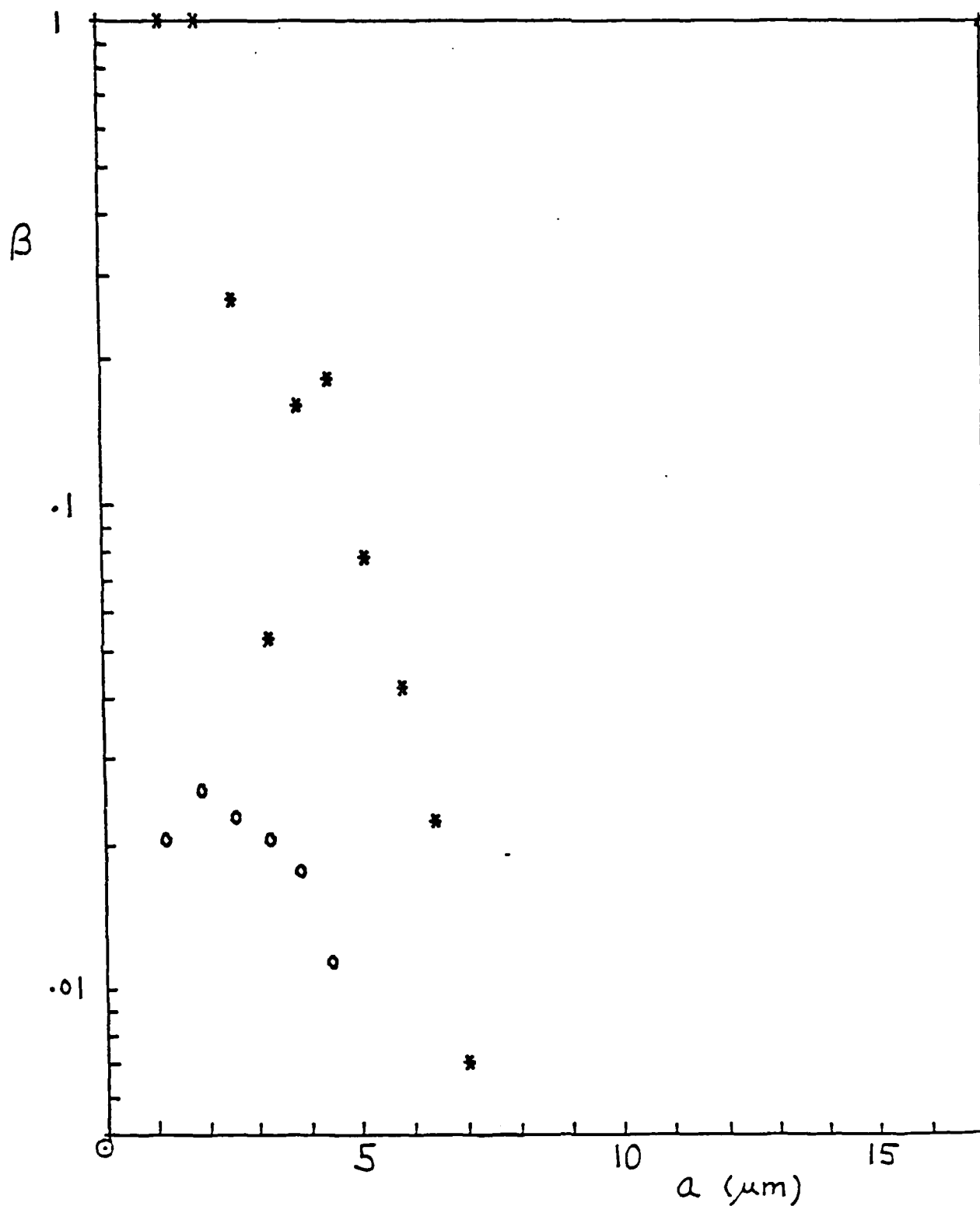
Fig. 11.   Condensation coefficient, β, vs. cloud drop size, a,
for the first expansion (*) and for the second expan-
sion (o) in the cloud simulation chamber 'oscillating
type' experiment 080787.

Data for several oscillating experiments are shown in Fig. 12 where we have plotted results for the separate growth phases (the first point depicts growth phase 1, the second point depicts growth phase 2, etc.). For each phase we have calculated and plotted the average value of β for that phase, and then constructed error bars corresponding to the standard deviation about that average. These error bars reflect the range of values experimentally found. In the calculation the natural logarithm of beta rather than β itself was averaged. Individual experiments consist of six or less growth phases. Nine different experiments are shown. These data show the following trends. During the first growth phase the average β is large, typically around 0.2. It exhibits relatively large error bars, and this is due partly to the fact that β is changing substantially during the course of the phase. Subsequent growth phases typically show a much lower β, with an overall average $\beta = 0.01$, and have much smaller error bars. On some occasions growth phase 2 shows a higher β than the following growth phases, but is usually significantly lower than β for the first growth. Recall that all the growth phases for a given experiment use the same sample of moist aerosol laden air. Growth phases 2 and greater are clearly different than growth 1. Even without the benefit of analysis, this effect is evident in the raw data. At similar points in the expansion the cloud droplets are simply growing slower in the subsequent growth phases as compared to first growth. This likewise can be seen in the raw a(t) data. Note that the average β for aged drops is 0.01, which is in a region which makes it sufficiently rate controlling to give beta significant
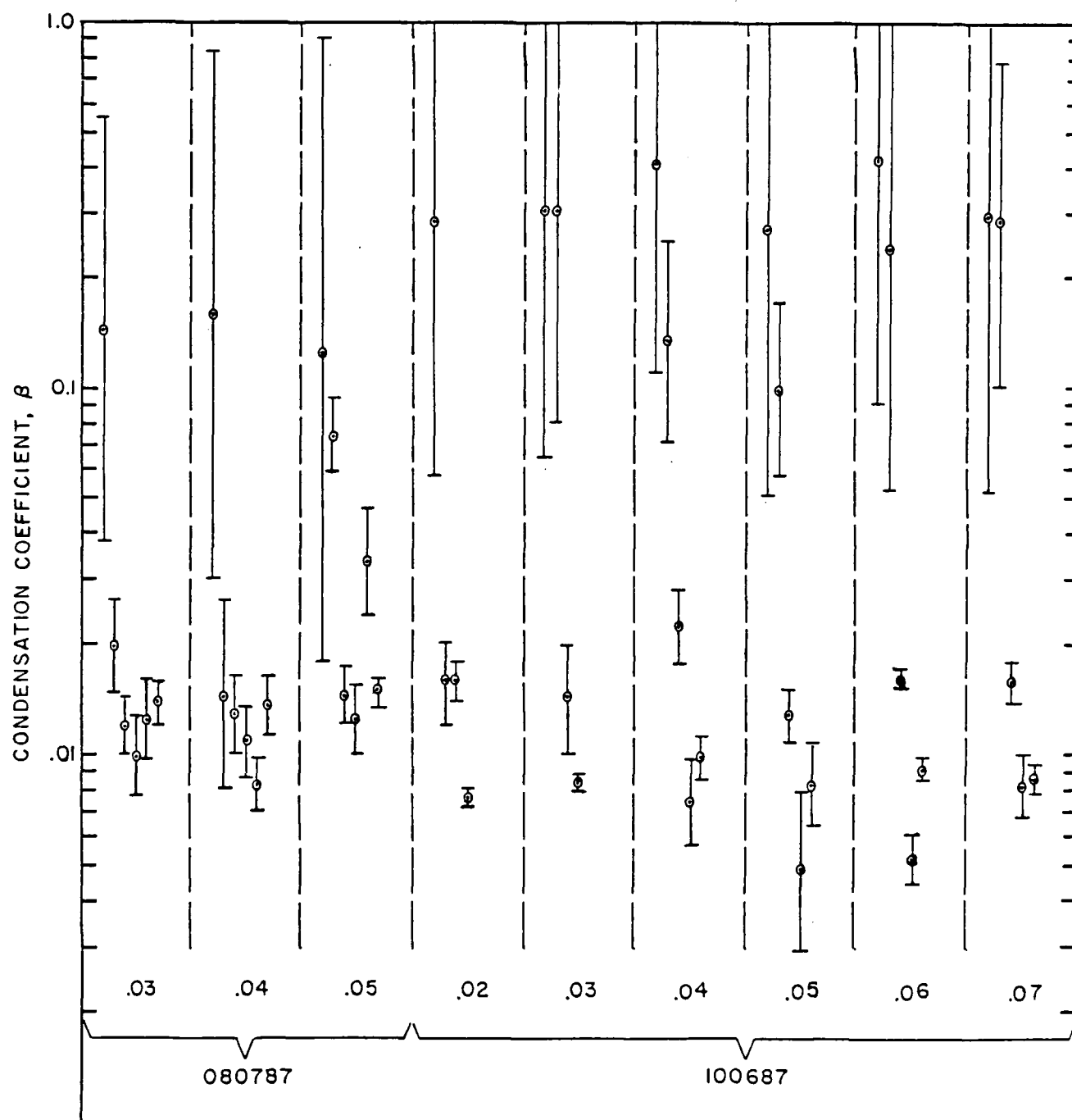
Fig. 12. Condensation coefficients, β, and corresponding 'error' bars resulting from the various cloud drop growth phases of the 'oscillating type' cloud simulation chamber experiment series 080787 and 100687.

atmospheric importance (Chodes, et al., 1974).

Some data were taken for the evaporation phases of the experiment. Usually our chamber control is not as good during the evaporation phases of the experiment, and the Mie light scattering traces are noticeably inferior. Data were therefore only analyzed for the first evaporation phase. They showed larger error bars than growth phase 1, and the magnitude of the error bars can be attributed to scatter as opposed to systematic change in β with time. The overall average β for evaporation phase 1 was 0.13, which is between the averages for growth phase 1 and the subsequent growth phases.

M. Error propagation.

The major uncertainties in the β analysis arise from two sources: uncertainty in droplet size (a) measurement, and the uncertainty in the determination of initial water vapor mixing ratio (r_0) which controls the supersaturation. Reasonable error estimates for these variables are delta-a = 0.025 μm and delta-r_0 = 0.000007 (Hagen, et al., 1988). The error in a is random, while the uncertainty in r_0 is systematic. Numerical analyses were performed using test cases to determine the propagation of these two errors into the final result for β. We found that a random 0.025 μm error in drop size measurement leads to an error in β of 11% for large β (near unity), and of 2% for small β (near 0.03). The delta-r_0 = 0.000007 leads to a systematic error in β of 47% for large β, and of 7% for small β. Clearly the largest source of uncertainty lies in delta-r_0, but its contribution is sufficiently small for the data to be meaningful. However it is

clear that excellent humidity measurement is a pre-requisite for condensation coefficient measurement studies.

N. Discussion.

Contamination hypothesis. The behavior of β for condensing drops has been an unexpected and perplexing result of these experiments. Although there are many measurements of low coefficients for β [e.g., Pruppacher and Klett (1978)], the consensus appears to be that β should be unity for a pure surface (Mozurkewich, 1986; Palmer, 1981; Cammenga, 1980; Sherwood, et al., 1975; Hickman, 1966), and there have been a number of measurements to support this consensus (Schulze and Cammenga, 1980; Rubel and Gentry, 1985; Wagner, 1982; see also Pruppacher and Klett's compilation, 1978). Narasawa and Springer (1975) distinguished between a fresh surface, for which a value near 0.2 was measured, and a "stagnant" surface which exhibited a coefficient of 0.038. The trend of the data reported here are consistent with the conjecture that trace contaminants, probably from the gas, play an important role in the condensation of micron-size drops. Indeed Cammenga (1980) echos the concern of other researchers in stating that "most phase transitions, especially evaporation and condensation at liquid surfaces, are extremely sensitive to minute contaminants which are very difficult to exclude". Nor is their effect confined to the phenomenon of condensation: Lucassen-Reynolds and Lucassen (1969) have reported substantial damping of water waves by surfactants at well below the concentration needed to form monolayer coverage. The trace contaminant most effective in retarding condensation rates (lowering β) would appear to be

surfactants. Their role in retarding hydrometeor growth/evaporation has received considerable attention (Bigg, 1986; Toossi and Novakov, 1984; Gill et al., 1983; Weschler, 1981; Garrett, 1978; Bullrich and Hanel, 1977), and a number of investigations have focused on the extreme retardation associated with complete coverage, (e.g., Rubel and Gentry, 1984, 1985; Derjaguin et al., 1966; LaMer, 1962). Comparatively few studies have been addressed to analyzing or measuring the effects of partial coverage (Carstens and Podzimek, 1986; Rubel and Gentry, 1984; Derjagen et al., 1982; see Appendix E). These studies suggest that partial coverage by trace surfactants can affect the magnitude of although it is hard to justify quantitative estimates of the effect. In the work described herein we have taken precautions to ensure system and sample purity. Particular care has been taken with the fast expansion chamber both in its construction (all interior surfaces are Teflon, glass, or stainless steel) as well as its cleaning (Bake out at $190°F$, followed by cleaning with reagent grade acetone, and prolonged spraying of the interior with Burdich and Jackson high purity water). At this point we are not able to identify (much less monitor) trace contaminants that may remain in these systems after the cleaning process. If it is indeed trace contaminants that cause the decrement in β, observed in both the fast expansion and simulation chambers, it is likely that such levels of contamination exist in real atmospheric conditions as well as in most "normal" laboratory conditions.

Implications of droplet ageing (contamination). A real atmospheric aerosol is likely to be a mixture of fresh and aged

particles, including evaporated hydrometeors. The above results imply that the aged component will respond more slowly to imposed high humidity conditions (Bigg, 1986). Cloud drop evaporation at a cloud's side boundary for example will be a source of aged aerosol. A major source may be evaporation of drops entrained from cloud top. When the aerosol, resulting from cloud drop evaporation, is mixed with fresh aerosol and reingested into cloud base the fresh aerosol will have the opportunity to activate before the aged aerosol and thereafter grow faster than otherwise because of reduced competition from the aged aerosol droplets. These will be smaller because they activated later and have lower growth rates after activation. Hence the fresh aerosol CCN can produce larger drops. Combustion aerosol injected into the atmosphere in large fire plumes can be another source of aged aerosol. A major fraction of such aerosol passes through a non-precipitating cap cloud which often forms at the top of the fire smoke plume. The CCN activate, form small drops, and then evaporate. Their subsequent evolution will be as aged aerosol particles and will exhibit the smaller condensation coefficient associated with aged drops. This ageing effect will extend their lifetime in the atmosphere.

Thermal accommodation coefficient. In this analysis the thermal accommodation coefficient has been assumed to be unity. All of the burden for slowing down droplet growth has been assigned to the condensation coefficient. Even though these two coefficients enter into the droplet growth rate via a single length parameter ℓ, they do exhibit different temperature and pressure dependencies, and hence it is feasible to separate them

in the analysis by treating data from experiments performed at widely different temperatures and/or pressures (the major disadvantage in reducing pressure, as previously pointed out, is that it brings the transport phenomenon into the transition regime). However this has not been done here. All of the present experiments were done at about the same temperature (near 16°C) and pressure (near 13 psi). In addition recent water drop growth measurements (Sageev, et al., 1986) on drops held in an electrodynamic balance imply a thermal accommodation coefficient that is near unity, leading to a minimal influence of thermal accommodation on droplet growth.

O. Conclusions.

In this study cloud drop growth observations are made under well-known temperature, pressure, and supersaturation conditions and then analyzed to determine condensation coefficient with the assumption that the thermal accommodation coefficient is unity. β, the condensation coefficient, is found to be near unity for fresh drops. It then falls off with time. β decreases with increasing $\int \dot{a} dt$. Data taken in fast piston expansion cloud chambers, employing vastly different supersaturations and time scales, exhibit trends similar to those found in the cloud simulation chamber. Once a droplet has been aged (probably contaminated) it retains its lower β value even when evaporated, and the lower β is exhibited when it is subsequently subjected to cloud formation and growth. The average β for aged drops is 0.01, as determined from growth cycles two through six in our oscillating profile experiments. This is in agreement with Garnier et al. (1987). The trend of a much smaller β for aged

drops cannot just be an artifact associated with the theory or the analysis, because it can be seen in the raw a(t) data. Growth is much slower for aged drops than for fresh drops under the same conditions. A β near 0.01 is sufficiently small to have a significant effect on the broadening of the size distribution of cloud drops in a developing cloud.

V. SCAVENGING EXPERIMENTS

The scavenging experiment has not yet been completed. Much of the preliminary work has been done however (see preprint of the study on hydration properties of laser dyes included in this report as Appendix D) and we should be completing these experiments by summer 1988. Here we present a report on the current status of this effort.

A. Description of scavenging experiment

Figure 13 is a schematic of the experiment. Two kinds of aerosol are generated simultaneously. A fairly monodisperse NaCl aerosol is generated by the furnace technique. An electrostatic classifier (EC) strips away all particles but those within a very narrow size range, with diameter centered about 0.05 μm. This aerosol will then have a critical supersaturation (S_c) of about 0.3%. Meanwhile a nuclei counter monitors the concentration of this aerosol so that it can be kept close to the desired value. Simultaneously a standard Collison nebulizer (CN) produces an aerosol of a fluorescent laser dye. The monodisperse output of the EC is an aerosol with a particle diameter (D_p) of about 0.03 μm and an $S_c \geq 1.0\%$.

These two aerosols are merged and diluted by about 100:1 by the filtered, humidified air from the air preparation system. After about twenty minutes of continuous flow through the simulation chamber (SC), it can be considered to have a homogeneous sample inside. The SC is closed off, allowed to equilibrate aerodymically and thermodynamically, and then expanded. During this expansion, the supersaturation never exceeds 0.9%.

Cloud drops will form, therefore, on the NaCl aerosol but not on the laser dye aerosol. The expansion is arrested so that the drops formed on the NaCl nuclei remain at a constant diameter of about 3 μm. This condition is maintained for perhaps 1000 seconds.

The following three species now coexist in the chamber: unactivated dye particles of $D_p \approx 0.03$ μm, water drops of diameter ≈ 3.0 μm (activated NaCl nuclei) and water drops (activated NaCl nuclei) that have scavenged a 0.03 μm dye particle.

The question to be answered is this: What fraction of the 3.0 μm water drops will scavenge one or more of the 0.03 μm dye particles in the 1000 sec?

To answer this, we proceed with the next phase of the experiment. At the end of the 1000 seconds, a small flow of gas is withdrawn from the SC and passed through the Fluorescent Aerosol Optical Particle Counter (FAOPC). The FAOPC is composed of an ellipsoidal mirror, an Argon ion laser, and two photomultiplier tubes (Fig. 26). The photomultiplier tube on the left, PMT 1, is at one of the foci of the mirror and is shielded by a Schott glass filter that will pass only wavelengths greater than 5400 A. The photomultiplier tube on the right, PMT 2 is unshielded. The beam of the Argon ion laser passes through the other focus of the mirror as does the air withdrawn from the SC.

The two types of water drops will scatter much more light (4880 A) than the small dye particles and can, therefore, be distinguished from them. They can be distinguished from one

another because only those that scavenged a dye particle will fluoresce (at wavelengths $\geq$ 5400 A) and hence trigger PMT 1.

Five requirements must be fulfilled to insure success in these experiments.

1. The dye aerosol must be excited by the 4880 A line of the Argon ion laser.

2. The dye dissolved in water must be strongly fluorescent.

3. We must be able to generate monodisperse aerosols of the dye with mean diameters between .02 μm and 0.20 μm.

4. Monodisperse aerosols described in 3 must not activate in the SC expansion and hence need to have $S_c \geq 1.0\%$.

5. The FAOPC must be able to discriminate between unactivated dye particles, water drops formed on NaCl aerosols, and water drops (formed on NaCl aerosols) that scavenged one or more of the dye particles.

We have purchased nine laser quality dyes that are pumped by the 4880 A line of the Argon ion laser. Clearly we have met requirements 1 and 2. Six of these are readily soluble in water and the remaining three are soluble in alcohol. These solutions, when nebulized, will produce aerosols to satisfy requirement 3.

Of course one would hope that a monodisperse aerosol of pure laser dye particles (of at least one of the nine dyes) would satisfy requirement 4. Unfortunately such a simple solution was not to be. Using pure dye particles, requirement 4 is satisfied only if $D_p \geq .06$ μm. For particles with $D_p \geq .06$ μm hybrid particles composed of an inert core of monodisperse polystyrene latex (PSL) spheres with a thin coating of dye material are

necessary. But first we shall discuss the simpler case of pure laser dye particles.

B. Measurements of S_c vs D_p for Aerosols of Pure Laser Dyes

Experiments were performed to measure the critical supersaturation (S_c) vs dry diameter (D_p) for pure laser dye particles using the setup shown in Figure 14. Compressed breathing air or compressed N_2 passes through a diffusion dryer (DD), through an absolute filter, and then atomizes the laser dye solution. The solution strengths were typically 2×10^{-5} gm dye/CC H_2O.

The resulting dye aerosol then passes through another DD. A Thermo Systems, Inc. Electrostatic Classifier (EC) then extracts an aerosol of very narrow size range centered about the diameter D_p. All the particles in this aerosol are charged positively, so to avoid spurious losses to grounded metal tubing, a second Bipolar Charger (BC) follows. This BC brings the aerosol into equilibrium with the charge distribution described by the Maxwell-Boltzmann distribution. [The first BC is internal to the EC.]

From there the aerosol flows past the CFD/IT where a small sample ($\approx .01$ lpm) is withdrawn for testing. This CFD/IT operates in either of two modes. In the continuous flow diffusion (CFD) mode it operates as a vertical flow thermal diffusion chamber and is capable of imposing on the test aerosol any S between 0.10% and 8.0%. An optical particle counter (OPC) is used to count the activated nuclei. For S between 0.013% and 0.10% the CFD/IT chamber operates in the isothermal mode (IT) and makes use of the sizing capability of the OPC to arrive at S_c.

The IT applies S = 0% (relative humidity of 100%) to the nuclei and so obviously does not activate them. The nuclei do, however, take on water and grow to an equilibrium size D_{100}. The correspondence between D_{100} and S_c is provided by the Laktionov relation

$$S_c(\%) = \frac{0.08}{d_{100}(\mu m)}$$

Figure 15 is a schematic of the chamber. The sample air enters at the top, passing through a tube 0.5 mm diameter by 6 cm long and then through a tube 0.25 mm diameter by 2.5 cm long. These two tubes are coaxial, and are positioned as shown in Fig. 15, where they are labeled as the sample metering tube. The pressure drop across the sample metering tube meters the sample flow rate, which is usually in the range 4-16 cm^3 min^{-1}. Filtered air also enters the chamber at the top, through the wing-shaped portions of the chamber (Fig. 15), which are filled with 1 mm diameter glass beads to break up the larger vortices. The sample air blends with the filtered air and flows down between the parallel plates in such a way that the sample air remains midway between the plates in a narrow coherent stream.

The parallel plates together with the rubber side walls enclose a rectangular space 100 cm long in the vertical direction, with a 0.8 cm by 13 cm rectangular cross section. Each plate is constructed of a piece of rectangular aluminum tube of 3 mm wall thickness through which thermostated water flows at a rate of 30 ℓmin^{-1} to keep each plate isothermal. When operated as a thermal diffusion chamber, one plate is kept hotter than the

other, and the inside surfaces of each plate are covered with filter paper continuously saturated with water. In order to avoid transient supersaturations, the top 15 cm of the hot plate is kept dry.

The development of the temperature and vapor pressure profiles in the entrance region of the chamber has been analyzed. This analysis shows that the profiles are fully developed within a length of 12 to 20 cm for filtered air flow rates between 5 and 10 ℓmin^{-1}, respectively. Downstream of this length there are no gradients in the flow direction, while both temperature and vapor pressure decrease linearly with distance from the hot plate. This produces a supersaturation profile of approximately parabolic distribution, with the maximum or operating supersaturation midway between the plates, and saturation at the plates.

At the bottom of the chamber, where water drops have grown on the active nuclei, the sample air plus some of the filtered air is sucked into the optical counter through a tube 1.3 mm diameter by 12 cm long. The largest portion of the filtered air, however, does not go into this tube, but instead flows down past it into a bottom plenum chamber (Fig. 15). It was found that this design causes the crossover region of the convection loop to move down into the bottom plenum chamber.

The alternating gradient chamber (ALGR) shown in Figure 16 also samples the test aerosol. It is operated at an $S > S_c$. The ALGR is composed of a stack of twenty five 1.0 inch tall brass cylinders with an axial 0.5 inch diameter hole in their centers. The top, third, fifth, seventh, etc., cylinders are

thermostated at 27.5'C. The second, fourth, sixth, eighth, etc., cylinders are thermostated at 5°C. The 0.5 inch diameter axial hole passing through the whole stack is lined with filter paper which is continuously saturated with distilled water.

The test aerosol is metered into the top by a hypodermic needle tube.

The S in the 0.5 inch diameter air passage is fairly constant over the cross section of this passage. Therefore small misalignments in the position of the aerosol metering tube or small serpentine wanderings of the aerosol stream down the 0.5 inch air passage do not cause any problem in the ALGR.

As long as the filtered air flow rate Q_f is kept large enough, no small convection cells will develop between adjacent brass cylinders, even at very high S values.

With these and other features, the ALGR functions best at high values of S. We typically operate ours at about S = 18%. This is high enough to easily activate all aerosol particles we study and hence we use it as a total particle counter to normalize the concentration measured by the CFD. Thus any time variations in the overall output of the CN are cancelled out.

In a typical experiment using the CFD/IT in the CFD mode, the two plates of the CFD were started at a large temperature difference so that the S it imposes is greater than the critical supersaturation S_c of the test aerosol. Then all particles activate and are easily counted by the OPC.

Simultaneously the ALGR is also measuring the concentration of the aerosol. The apparent concentrations of the aerosol as seen by the two chambers is, of course, about equal. The S

imposed by the CFD is lowered in a stepwise fashion and the ratio of the concentration as measured by the CFD, C_{CFD}, to the concentration as measured by the ALGR, C_{ALGR}, ($F = C_{CFD}/C_{ALGR}$) is then plotted vs the S_{CFD}. The value of F remains fairly constant at about 1.0 until it approaches S_c at which time it falls abruptly to zero as S passes through and goes lower than S_c. A typical plot of F vs S is shown in Figure 17. This experiment is repeated at different D_p values to cover the whole range of S available from the CFD. The result of these experiments for disodium fluorescein is shown in Figure 18.

As mentioned before the IT chamber makes use of the sizing capability of the OPC to arrive at the S_c of a particular nucleus. First a solution of NaCl is atomized. Again the EC withdraws a monodisperse aerosol which is then sampled by the IT. Since we know the D_p from the EC setting, Kohler theory allows calculation of S_c.

The output pulses from the OPC are categorized into 1024 channels of a Nuclear Data pulse height analyzer (PHA). This is repeated at several sizes D_p (or values of S_c, if you prefer) to calibrate the PHA.

Next the dye solution is atomized, a monodisperse aerosol of the dye passed to the IT, and the S_c of this aerosol determined from the calibration curve of the PHA. The experiment is then repeated for several different D_p values. The result of these experiments for disodium fluorescein is shown in Figure 18.

A few experiments were done to measure the S_c of disodium fluorescein (sometimes called uranine) at high S using only the ALGR. These points can also be seen plotted in Figure 18.

The fact that the data from the three techniques merge so well lends credibility to all three instruments. Figures 19, 20, 21, and 22 show similar data for other pure dye particles. The behavior of NaCl is shown for comparison.

The Kohler equations applied to these plots allow us to extract more information about the dye particles. The Kohler equation for the S_c of a nucleus of diameter D_p is

$$\log S_c = \frac{-3}{2} \log D_p + \frac{1}{2} \log \left[0.0658\ A^3\ \frac{M_s}{\nu \rho_s \phi} \right]$$

where

S_c – critical supersaturation of a nucleus of diameter D_p

A – a constant = 1.10×10^{-7} at $23°C$

M_S – molecular weight of the salt (or dye)

ν – number of ions into which the salt dissociates

ρ_s – density of the salt

ϕ – osmotic coefficient of the salt

D_p – diameter of dry salt particle

The Kohler theory predicts that a plot of $\log S_c$ vs $\log D_p$ should be a straight line and have a slope of -1.5 and an intercept given by the second term above. Slopes and intercepts of Figures 18, 19, 20, 21, and 22 are in Table 1.

Note that the slopes are indeed close to -1.5. The values in the ν column are the best guesses of a helpful organic chemist (Dr. Stoffer). We have recently discovered a technique to measure the density of the dry particles using a vibrating

orifice monodisperse aerosol generator (VOMA). We have a VOMA in the Center and plan to determine ρ_s so that we can then arrive at ϕ.

Note also that for sulforhodamine B and sulforhodamine 640, there is a slight deviation from Kohler behavior for $D_p \geq .03 \ \mu m$. At this time we think this is because the critical drop size for these particles is also about $0.03 \ \mu m$ and so several of the simplifying assumptions regarding dilute solutions are no longer valid. There seems to be interesting work ahead here.

Recalling requirement 4 and referring to Figures 18, 19, 20, 21 and 22, one realizes that the scavenging experiments of Figure 13 using pure dye particles can only be performed for dye aerosols with $D_p \leq .06 \ \mu m$. For $D_p \geq .06 \ \mu m$ we need to somehow keep the mass of the soluble material in the scavengeable particle about what it would be for a pure particle of $D_p \leq .06 \ \mu m$. The next section addresses this question.

C. Measurements of S_c vs D_p for Hybrid Particles

In this technique we add a few drops of PSL solution to the dye solution being atomized in Figure 14. Now the typical water droplet exiting the nebulizer jet will contain one PSL sphere and some amount of dye. After the water evaporates, one is left with a PSL sphere with a very thin coating of dye. By setting the EC to extract hybrid particles with an overall diameter just slightly greater than that of the PSL sphere, the volume of this spherical shell (and hence mass of dye) will be so small that this hybrid particle will have an $S_c \geq 1.0\%$. Since the PSL are very monodisperse, we can be confident that the amount of dye will be fairly constant from hybrid particle to hybrid particle.

Figure 23 illustrates such a hybrid particle, where D_{eff} is the diameter of the sphere of pure dye one would obtain by scraping the dye off the PSL and forming it into its own tiny sphere.

Figure 24 is the result of one such experiment. PSL with D_1 = 0.277 μm were used and the EC was set at 0.295 μm. This means that D_{eff} = .164 μm. Reference to Fig. 22 leads one to estimate that the predicted critical supersaturation $S_{C,\{RED}$ = 0.280%. Inspection of Figure 24 shows that the observed critical supersaturation $S_{c,OBS}$ = 0.290% (3.5% deviation).

Figure 25 is the result of another such experiment. Here PSL with D_1 = 0.109 μm were used and the EC was set at 0.120 μm. This means that D_{eff} = 0.076 μm. Reference to Figure 18 leads one to estimate that $S_{C.PRED}$ = 0.51%. Inspection of Figure 25 shows that $S_{c,OBS}$ = 0.50% (2% deviation). Note that there is a second knee in the curve. Assuming that these are pure dye particles, i.e., that they came from water drops in the nebulizer which did not contain a PSL sphere, one would estimate from inspecting Figure 18 that $S_{c,PRED}$ = 0.255%. Inspection of Figure 25 shows that $S_{c,OBS}$ = 0.255% (0% deviation) so indeed these must be pure dye particles.

Table 2 shows both actual results of experiments already performed and predicted S_c's for future experiments. Recall that the whole purpose in going to hybrid particles was to obtain large particles yet retain an $S_c \geq 1.0\%$. Clearly we have not yet done that, but this is because we have so far just used PSL we have on hand.

The third group of data in Table 2 is for proposed experiments using sulforhodamine 640 and PSL we have not yet

purchased. By purchasing the correct size of PSL and tuning the EC to a size just larger than that, we feel we will be able to make hybrid particles as large as D_p = 0.2 μm and still have $S_c \geq$ 1.0%.

The foregoing discussion allows us to conclude that requirement 4 can be met.

D. Fluorescent Aerosol Optical Particle Counter (FAOPC)

Refer to Figure 13 and recall that the FAOPC must distinguish between the unactivated dye particles, the water drops of $D \approx$ 3.0μm formed on NaCl nuclei, and drops of $\approx D$ $3\mu0$ m (formed on NaCl nuclei) that have scavenged one or more dye particles (or hybrid particles).

To test the performance of the FAOPC, we installed it under the CFD in place of the ordinary OPC shown in Figure 26.

First the behavior of PMT 1 and PMT 2 when unactivated dye particles passed through the FAOPC was determined by keeping the CFD set below the S_c of the dye particles. PMT 2 gave pulses of less than 0.1 V and PMT 1 gave nothing.

Second we investigated the behavior of PMT 1 and PMT 2 when 3.0 μm water drops formed on NaCl passed through the FAOPC. PMT 2 gave 7.5 V pulses and surprisingly PMT 1 gave 0.25 V pulses (see Table 2). This probably means that the Schott glass filter does allow some 4880 A light through so we take this as the noiselevel in PMT 1.

Third we investigated the behavior of PMT 1 and PMT 2 when 3 μm water drops formed on a dye particle passed through. For rhodamine 575 with the EC set at 0.2 μm, PMT 1 gave 0.6 V pulses

and PMT 2 gave 10 V pulses. Similarly for rhodamine 590 chloride and disodium fluorescein.

Clearly then we can distinguish between the three species passing through the FAOPC.

A parting criticism must not be omitted. We have previously stated that the dye particles must have $S_c \geq 1\%$ ($D_{eff} \leq .05 \ \mu m$). Obviously we have violated that in these last experiments. Therefore we will need to refine the FAOPC. Translators can better align the laser and optimize the PMT 1 signal. Perhaps the Schott glass filter itself is fluorescing and we should try something different. The photomultiplier tubeswe used were ones we took out of old equipment. We might gain asmuch as a factor of 10 or even 100 on the PMT 1 signal by upgrading here.

F. Update on FAOPC

The first prototype of the FAOPC had several inherent design flaws and so a second prototype has been built which overcomes these shortcomings.

An optical table large enough to hold both the Argon ion laser and the mirror housing/PMT mounts has been found. Proper alignment (X,Y,Z) of the laser beam is achieved by adjusting screws on/alongside the laser mount.

The inadvertent air leaks into the sensing volume due to improper construction have been eliminated.

The volume of air (inside the FAOPC) whose pressure responds to changes in the flows into/out of the FAOPC has been significantly reduced. This makes the response time of the flows to one another much less.

The coincidence counting capability is currently being designed and constructed. This feature will ensure that only those pulses from PMT 1 are counted as being a fluorescent drop. Otherwise a noise pulse from PMT 2 could be counted as a fluorescent drop.

TABLE 1

INFORMATION ON PURE LASER DYE PARTICLES

DYE	SLOPE	M_S	$\nu\rho\phi$	ν	$\rho\phi$
Sulforhodamine 640	−1.56	606.7	1.577	2	0.788
Fluorescein 548	−1.30	401.2	0.838	1	0.838
Rhodamine 590 Chloride	−1.50	479.0	1.286	2	0.643
Disodium Fluorescein	−1.53	376.3	3.553	3	1.184
Sulforhodamine B	−1.53	558.7	1.474	2	0.737

TABLE 2

INFORMATION ON S_C HYBRID PARTICLES

D_1 (μm)	D_2 (μm)	D_{EFF} (μm)	$S_{C,PRED}$ (%)	$S_{C,OBS}$ (%)	DEVIATION (%)
DISODIUM FLUORESCEIN					
.109	.15	.128	.22	.23	4
	.13	.096	.357	.347	3
	.12	.076	.51	.50	2
	.11	.039	1.32	1.23	7
SULFORHODAMINE 640					
.277	.32	.226	.173	.150	14
	.31	.204	.205	.222	8
	.295	.164	.28	.29	4
	.277	.145	.35	.36	3
SULFORHODAMINE 640					
.109	.12	.076	1.09		
.132	.14	.076	1.09	NOT DONE YET	
.154	.16	.076	1.09		
.175	.18	.076	1.09		

TABLE 3

RESULTS OF TESTING FAOPC

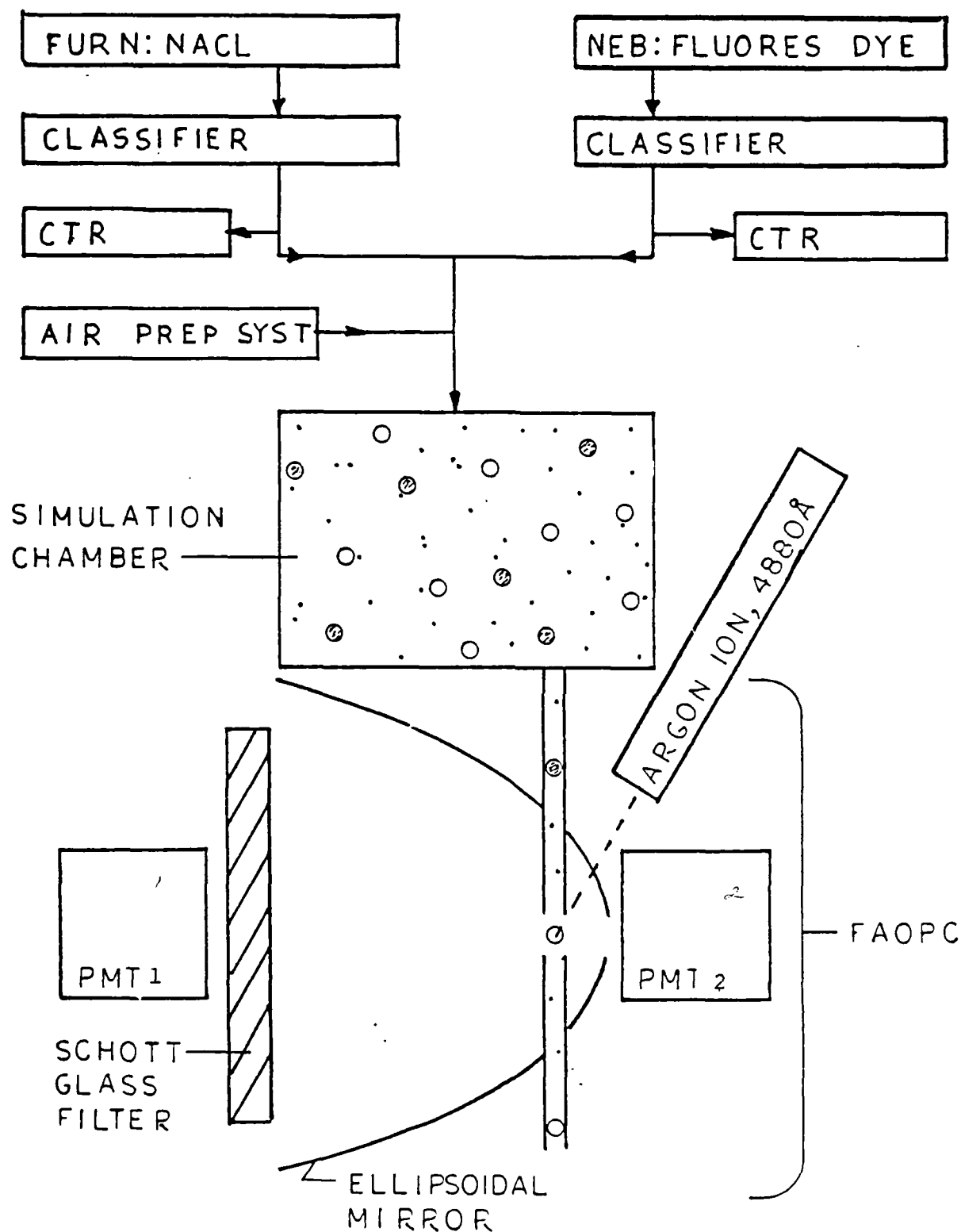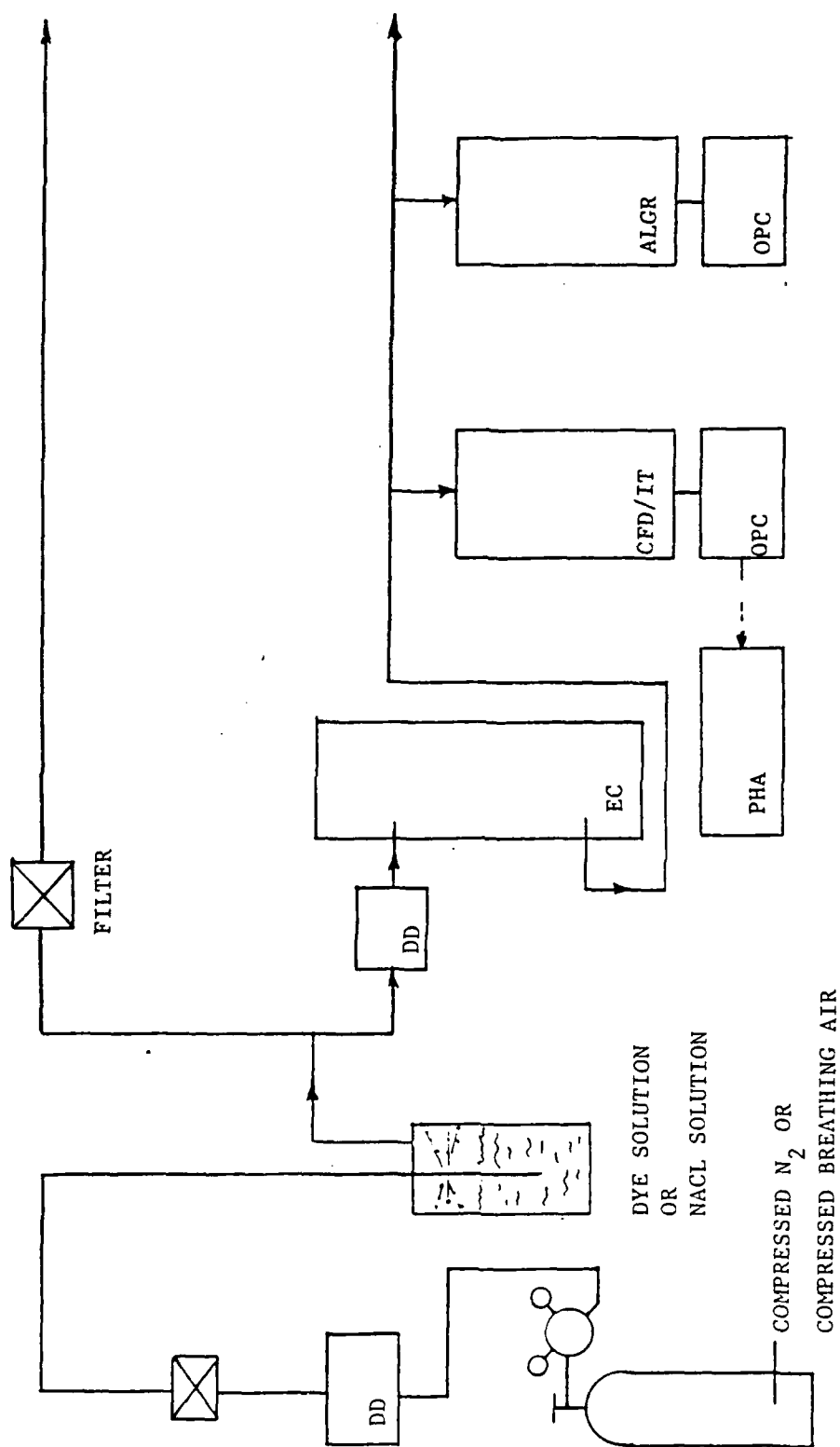| AEROSOL	D_P (μm)	PMT1 (VOLTS)	PMT2 (VOLTS)	SIGNAL/NOISE (NO UNITS)
NACL	0.4	.25	7.5	--
RHODAMINE 575	0.2	.6	10.	2.4
	0.4	.6	10.	2.4
RHODAMINE 590 CHLORIDE	0.2	.8	5	3.2
	0.3	1.1	7	4.4
	0.4	1.0	7	4.0
DISODIUM FLUORESCEIN	0.1	.8	20	3.2
	0.2	.8	13	3.2

Fig. 13. Schematic of scavenging experiment.

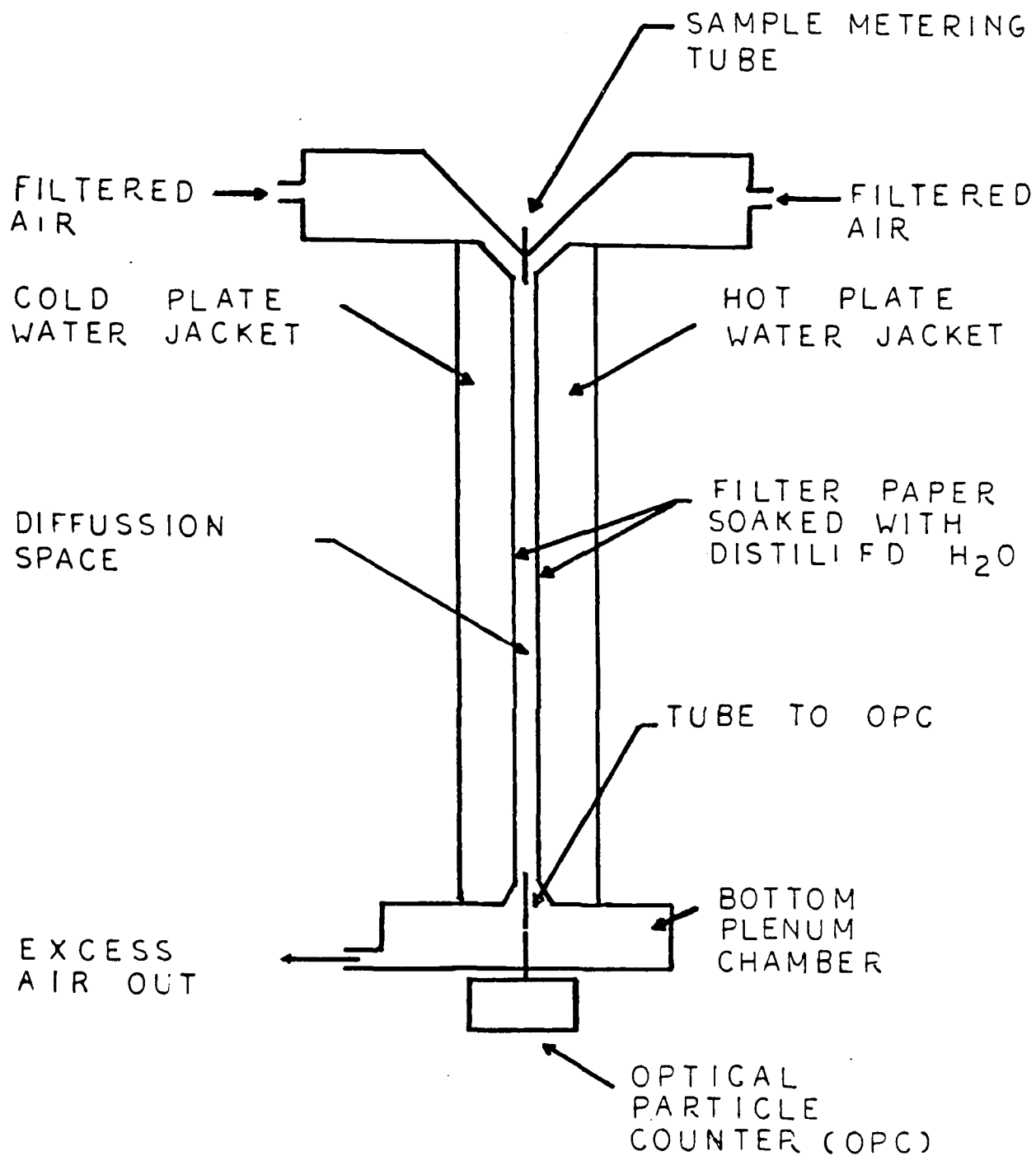Fig. 14. Setup for measurement of critical supersaturation vs. dry diameter for laser dye particles.

Fig. 15.
CONTINUOUS FLOW DIFFUSION CHAMBER (CFD)

AEROSOL

FILTERED
AIR

ΔP

WET FILTER PAPER

$T_C=5^{\circ}C$

$T_H=27.5^{\circ}C$

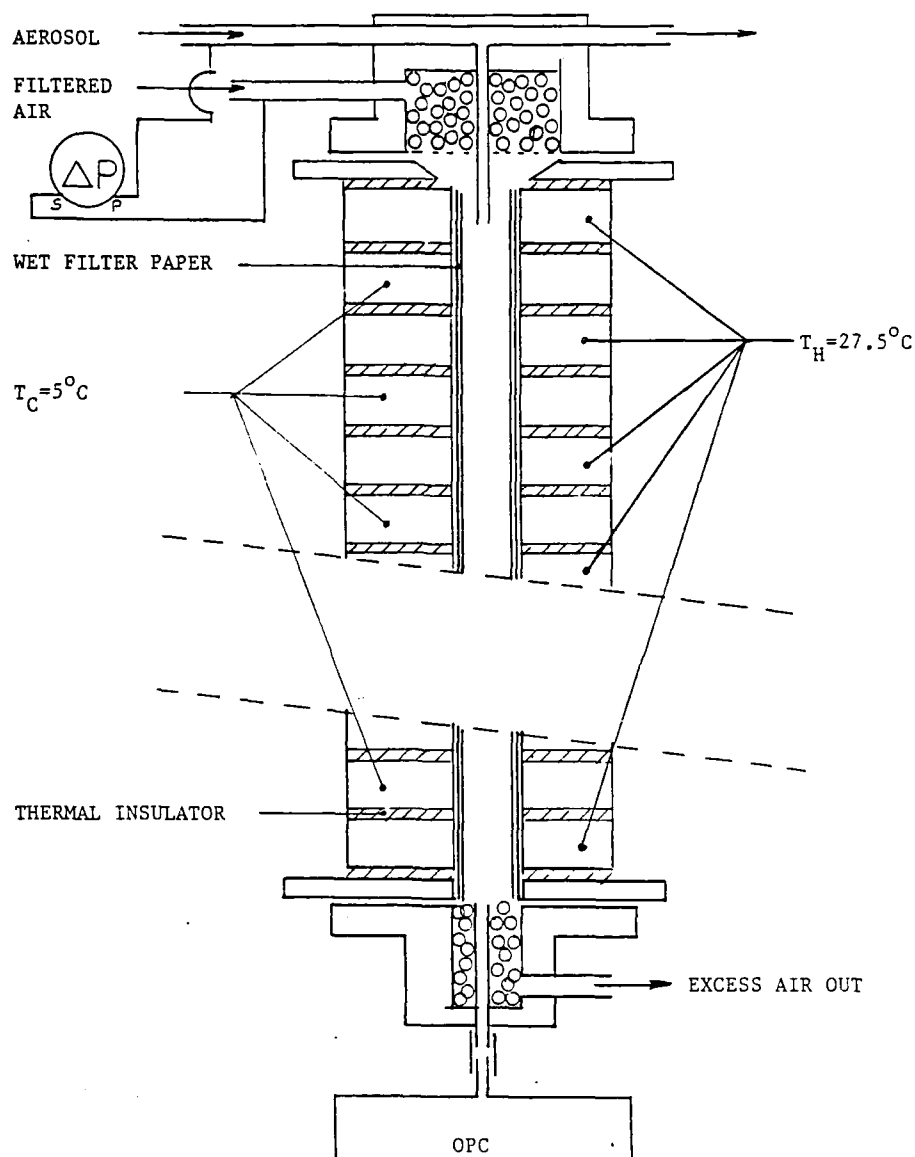THERMAL INSULATOR

EXCESS AIR OUT

OPC

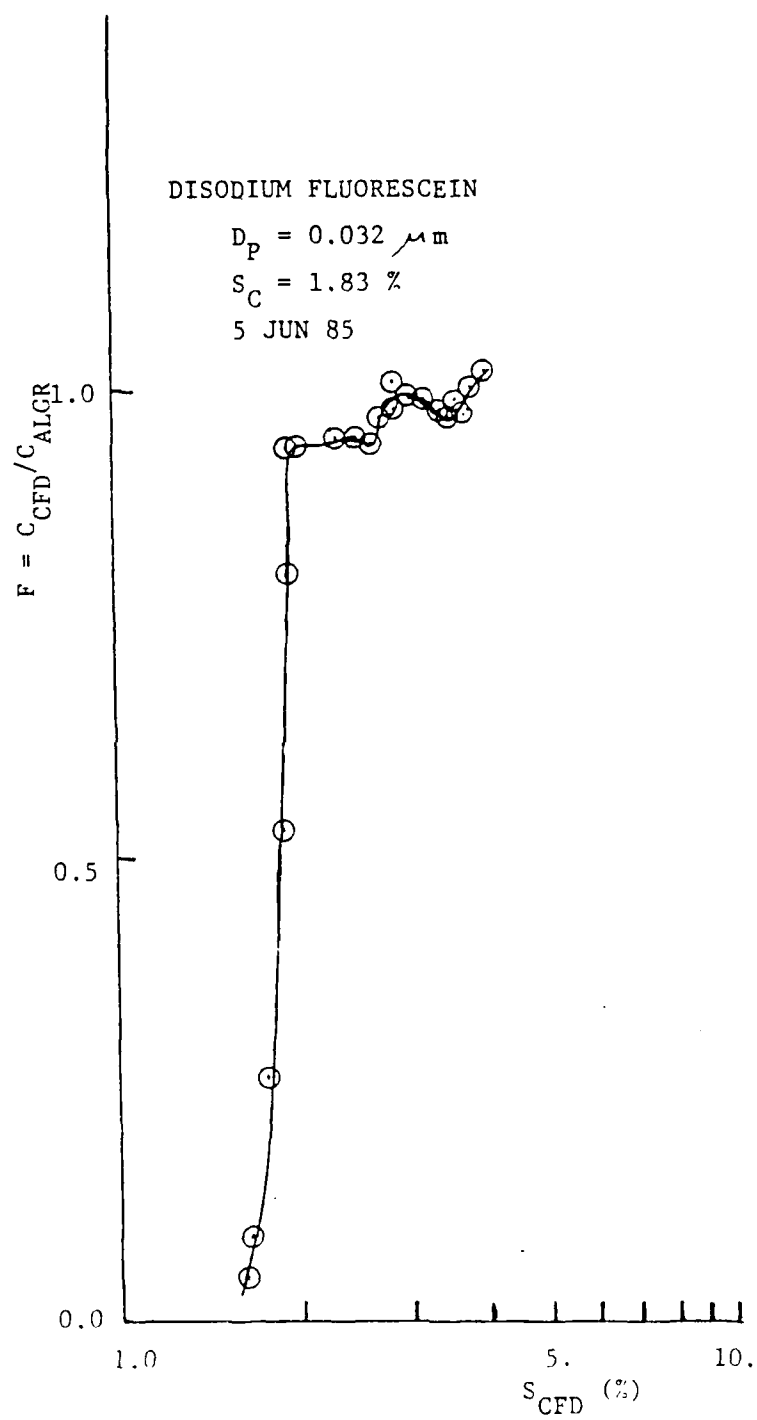Fig. 16. ALTERNATING GRADIENT CHAMBER

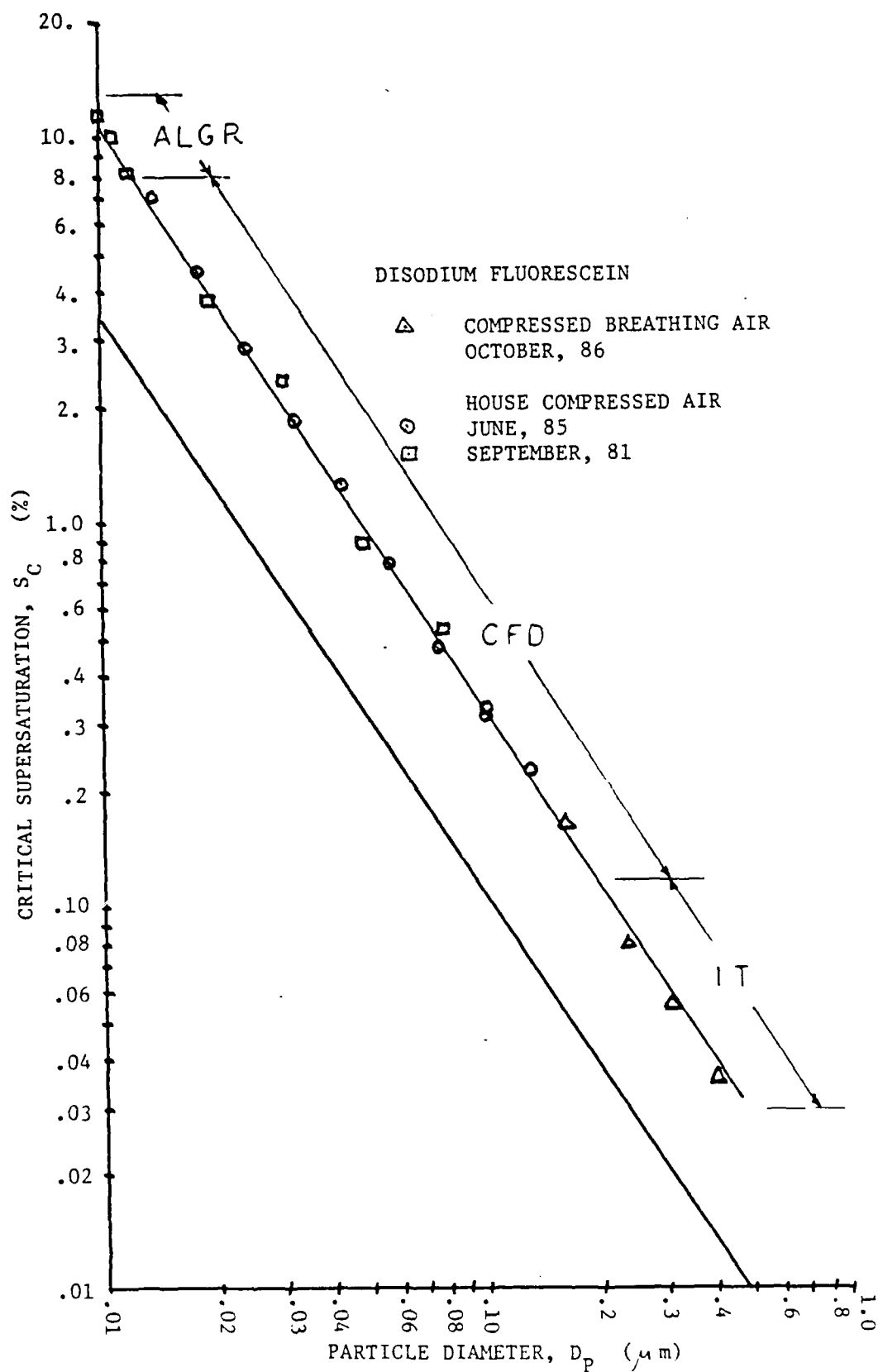Fig. 17. Ratio of concentrations measured by CFD and ALGR vs. supersaturation of CFD.

Fig. 18. Critical supersaturation vs. particle diameter.

Fig. 19

FLUORESCEIN 548

⊙   COMPRESSED N_2

△   COMPRESSED BREATHING AIR

CFD

CRITICAL SUPERSATURATION, S_C (%)

PARTICLE DIAMETER, D_P (μm)
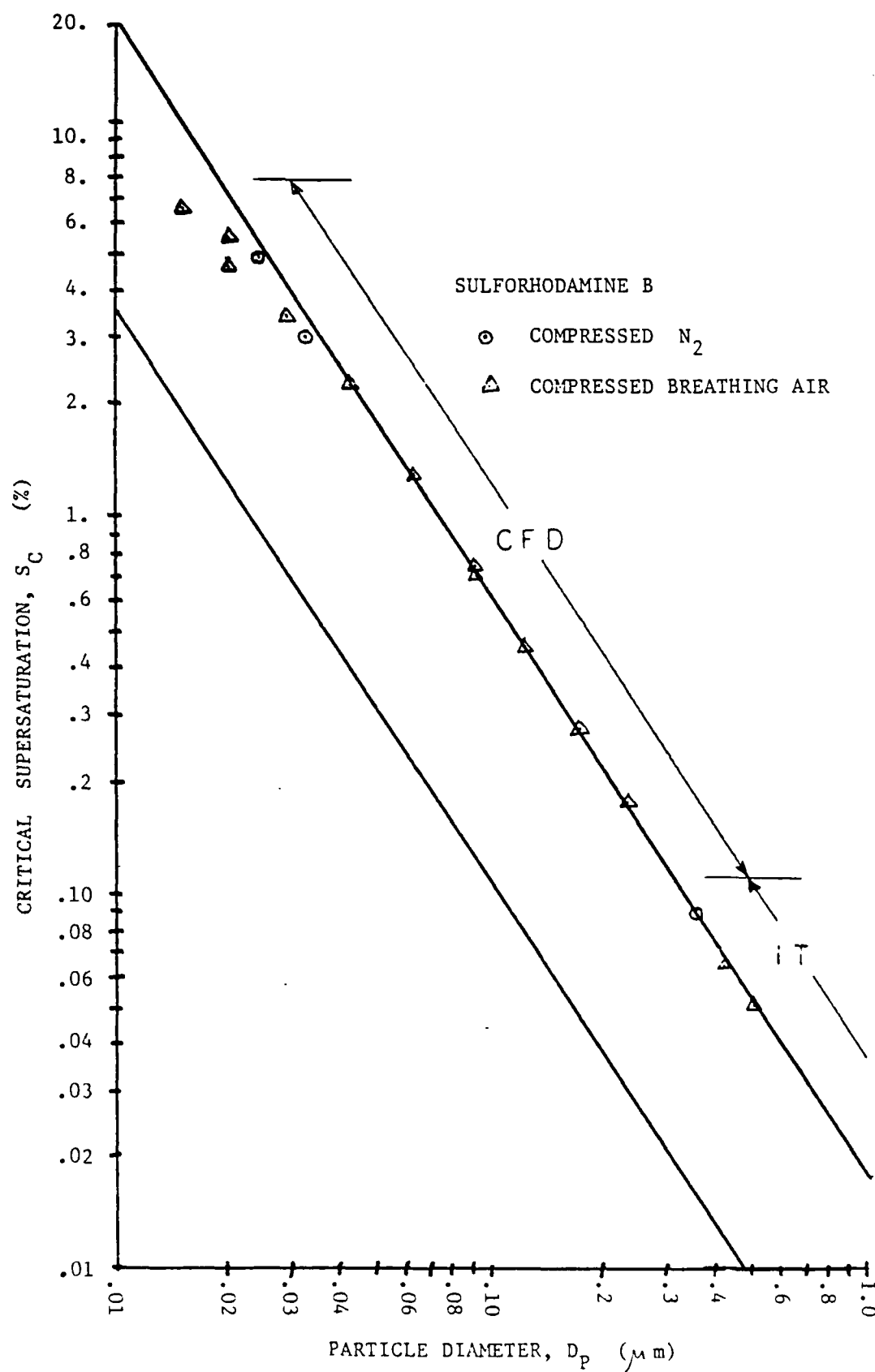
Fig. 20

Fig. 21

Fig. 22
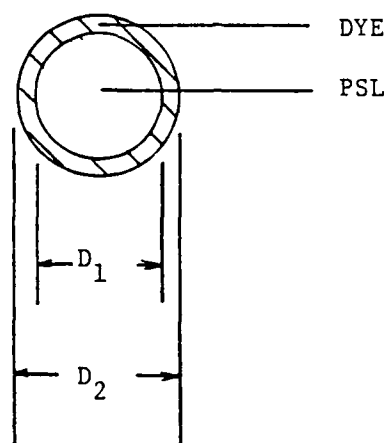
$$D_{EFF} = (D_2^3 - D_1^3)^{1/3}$$

Fig. 23. The hybrid particle.

SULFORHODAMINE   640 + PSL

$D_1 = 0.277 \mu m$

$D_2 = 0.295 \mu m$

$D_{EFF} = 0.164 \mu m$

$S_{C,OBS} = 0.290 \%$

$S_{C,PRED} = 0.280 \%$

$F = C_{CFD}/C_{ALGR}$

S_{CFD} (%)

Fig. 24

Fig. 25

Fig. 26

VI. PUBLICATIONS (including talks, presentations, and papers in preparation)

A. Talks given

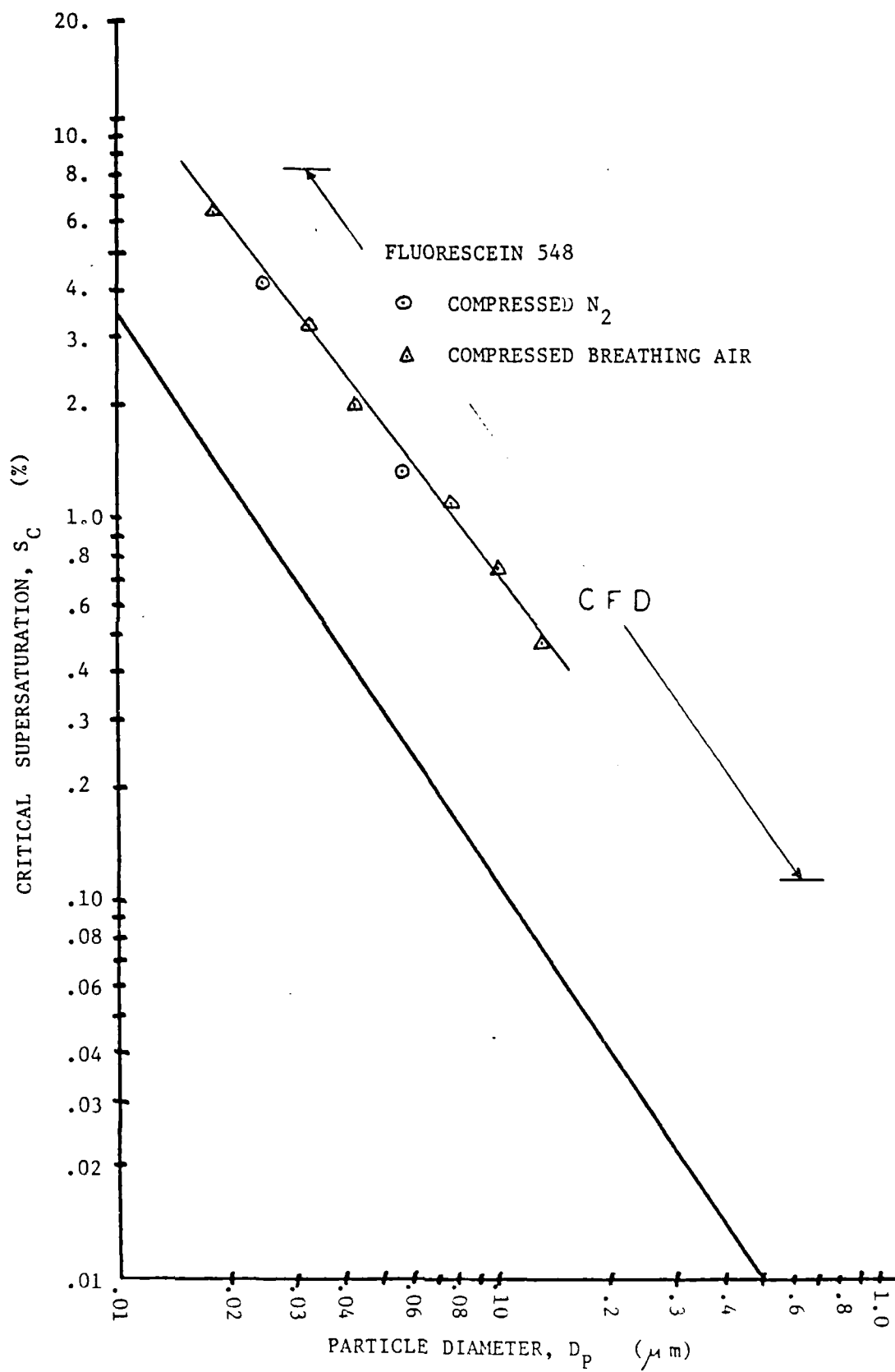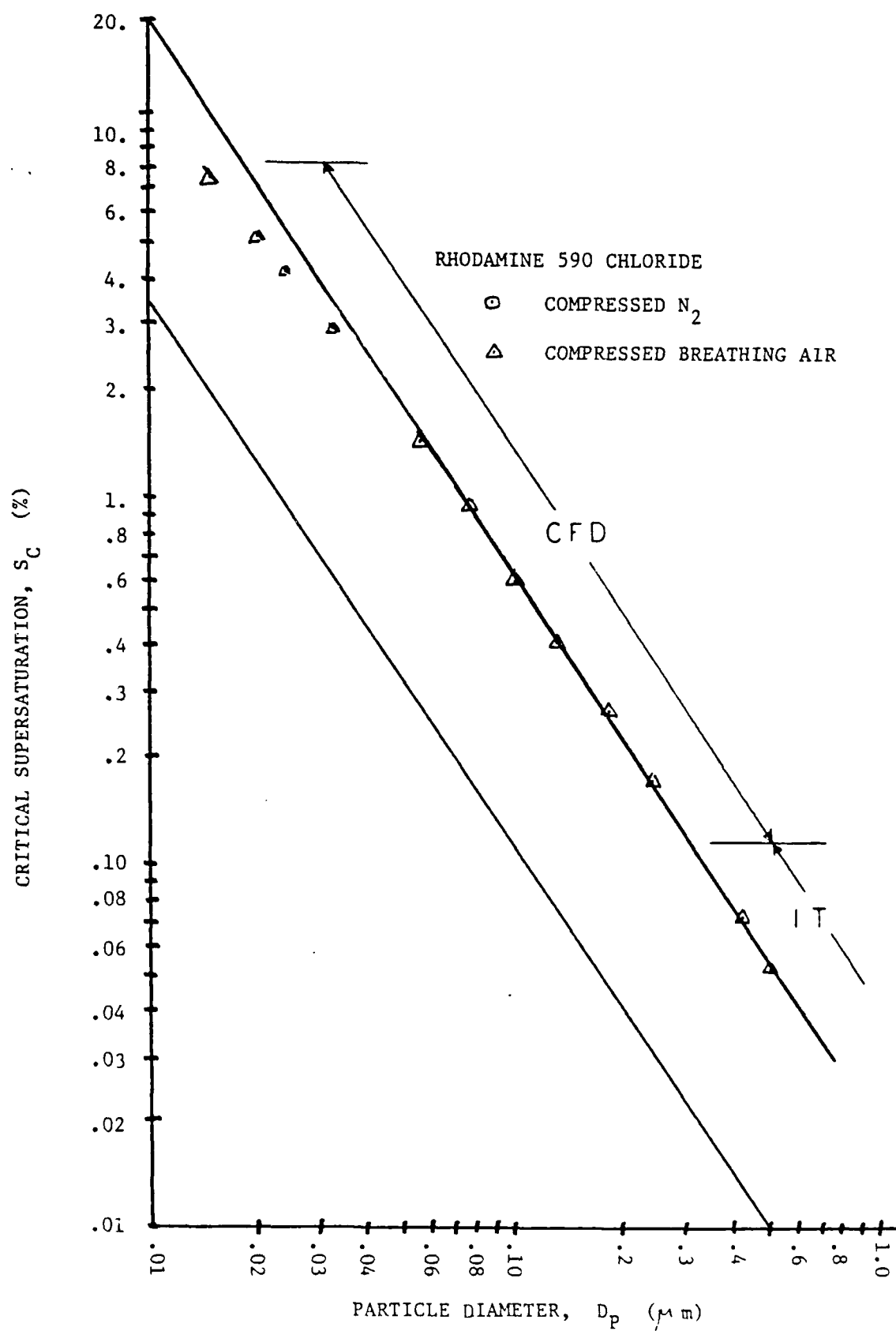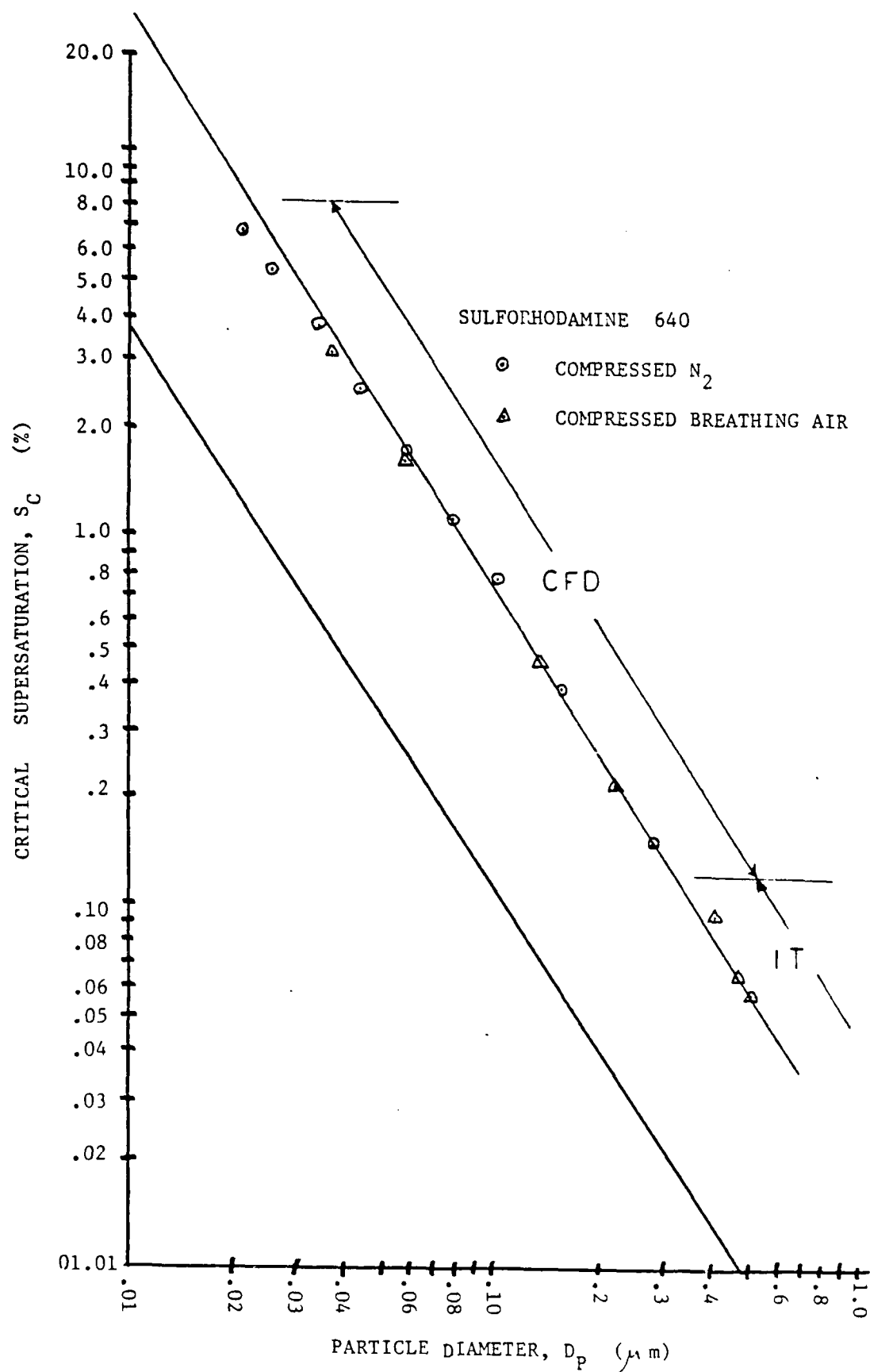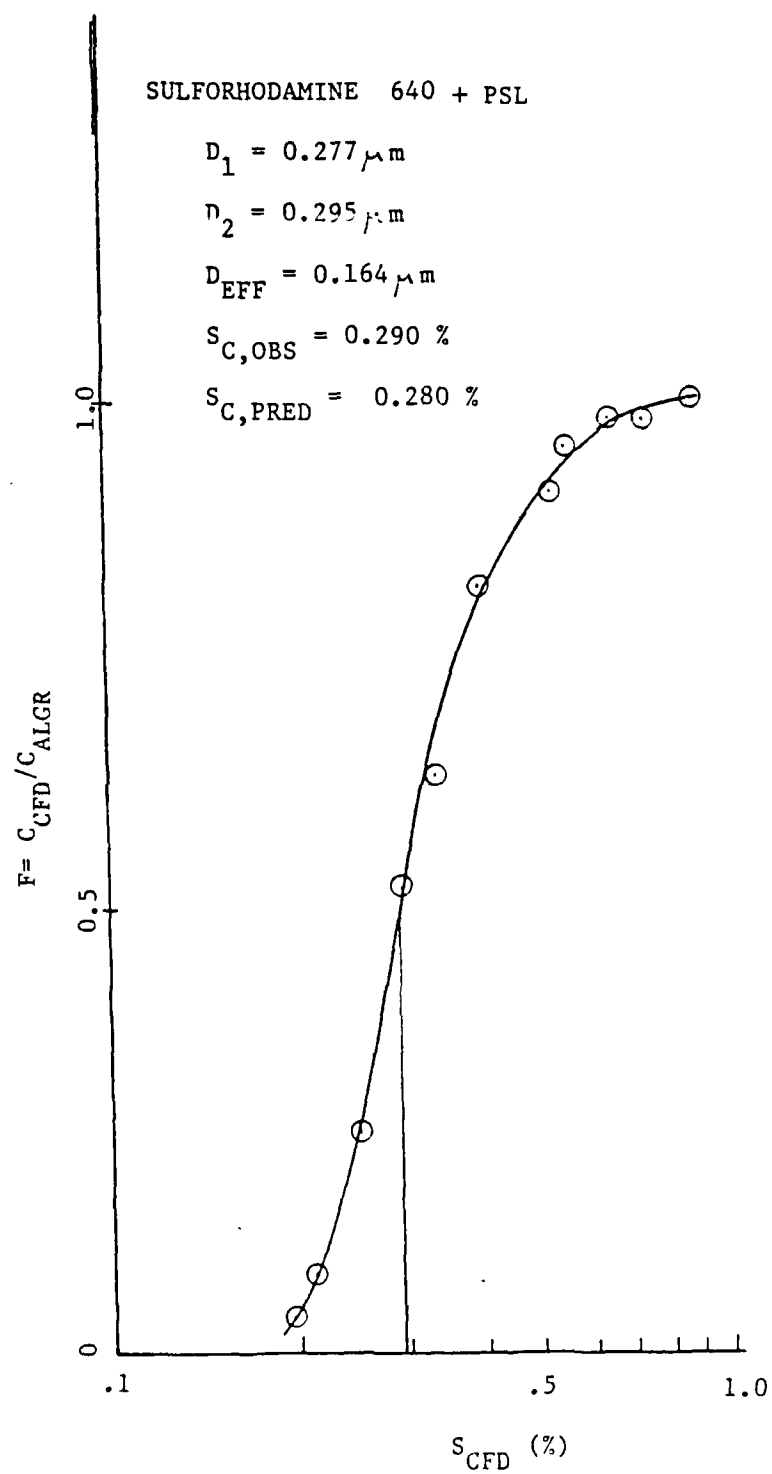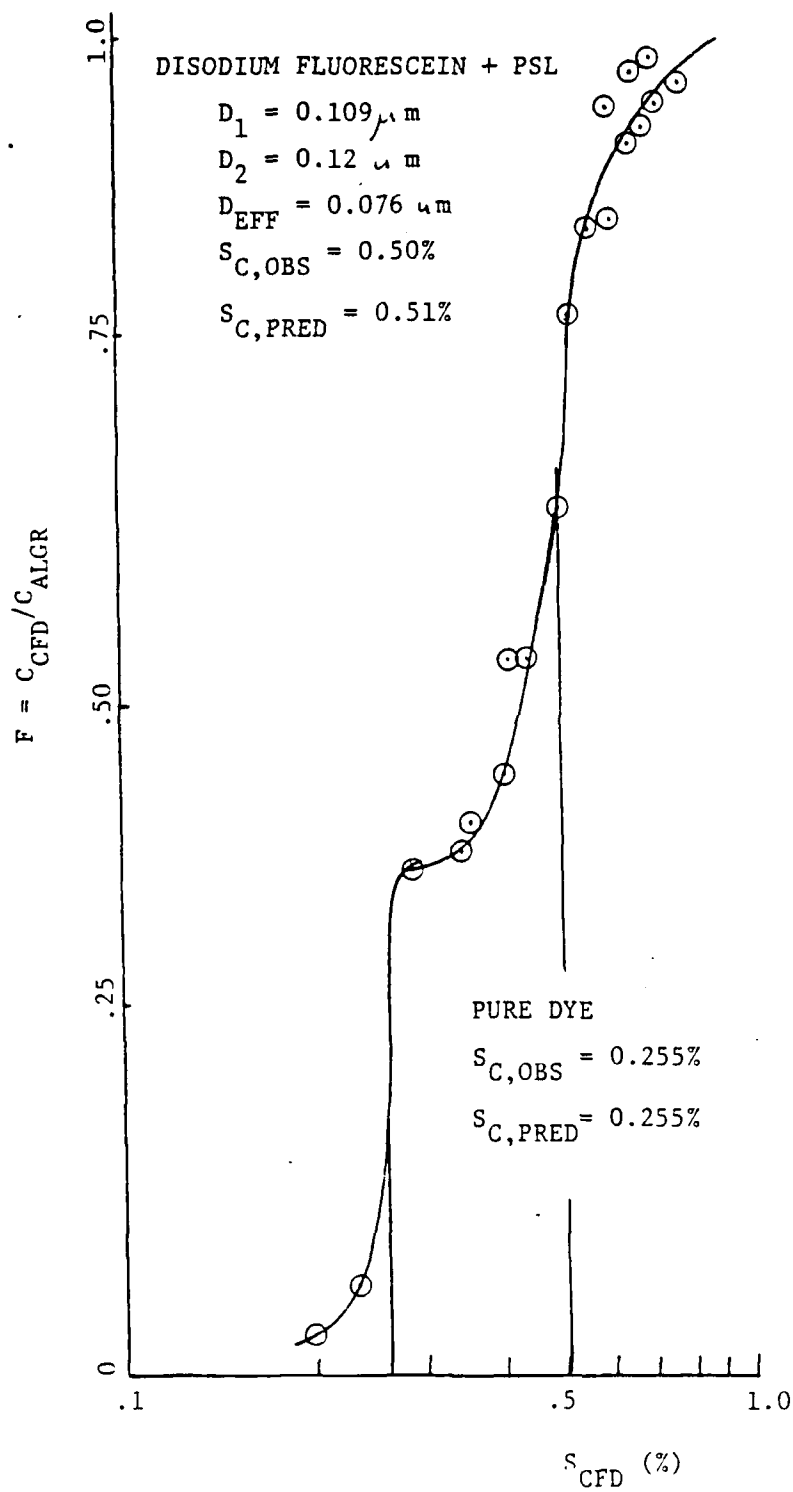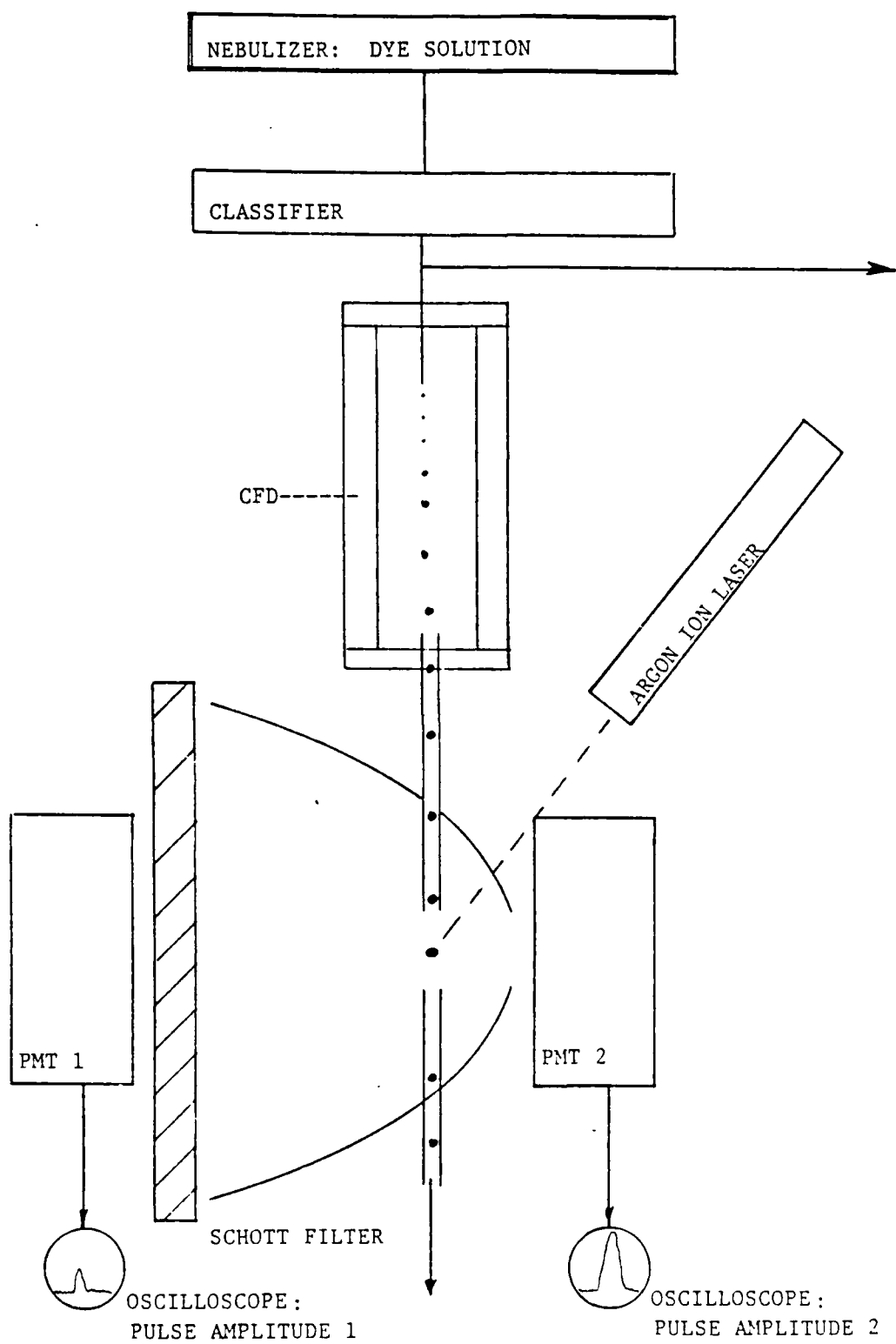1. Technical Workshop for the Future of Laboratory Research and Facilities for Cloud Physics and Chemistry, March 20-22, 1985 NOAA/NCAR, Boulder, CO.

    Reference: List R., J. Hallett, J. Warner, R. Reinking, 1986: The future of laboratory research and facilities for cloud physics and cloud chemistry, Bull. AMS, 67(11), 1389-1397.

    Three talks were given at this Workshop on the simulation facility:

    a. Measurement of microphysical cloud growth parameters in controlled laboratory environments: condensation coefficients and collision-coalescence efficiencies (Carstens).

    b. "UMR cloud simulation studies" (Hagen).

    c. Current status and capabilities of the UMR simulation facility (White).

2. International Symposium on Moisture and Humidity

    White, D.R., A.R. Hopkins, and J.L. Kassner, Jr., 1985: Establishment of a precise dewpoint in air for use in atmospheric science studies, Proc. Moisture & Humidity Int. Symp. (Washington, D.C., April 1, 1985).

3. Workshop on Physics of Laser Propagation in the Atmosphere, January 14, 15, Las Cruces

    UMR cloud simulation facility capabilities and experiments (Hagen, Alcorn, Alofs, Anderson, Carstens, Hopkins, Salk, Schmitt, Trueblood, White)

4. Conference on Cloud Physics, AMS, Snowmass, CO (Sept. 1986)

    a. Hagen, D., M. Alcorn, J. Kassner, J. Carstens, R. Hopkins, J. Schmitt, M. Trueblood, W. Walker, and D. White*, 1986: UMR cloud simulation studies of droplet growth: investigation of the condensation coefficient, Preprints, Conf. on Cloud Phys. 2 (AMS), 1-4.

    b. Carstens, J.C., J. Podzimek, H. Andriambeloma, 1986: Assessment of the impact of insoluble and surface active pollutants on fog evolution, Preprints, Conf. on Cloud Phys., 2 (AMS) 32-35**.

*D. Alofs' name was inadvertently omitted from the list of authors.
**Joint NSF, ONR, and AFOSR support.

5. Third Midwest Cloud and Aerosol Physics Association Meeting, U. of Wisconsin (Madison) Oct. 8, 1985

   Aerosols suitable for fluorescent water drop tagging experiments (D. Hagen, M. Trueblood)

6. Fourth Midwest Cloud and Aerosol Physics Association Meeting, Illinois Water Survey (Urbana) March, 1986.

   a. Results from warm cloud droplet growth experiments, D. Hagen

   b. Simulation chamber applications of Mie scattering, J. Schmitt

   c. A model of drop growth in the presence of an organic surfactant, J. Carstens

7. Fifth Midwest Cloud and Aerosol Physics Associaton Meeting, Argonne Nat. Labs (Argonne, IL)

   Update on condensation coefficient measurement in UMR simulation chamber, D.R. White, D.E. Hagen, M. Alcorn, D. Alofs, J. Carstens, R. Hopkins, J.L. Schmitt, and M. Trueblood

8. Defense Nuclear Agency (DNA), Technical Reviews

   a. White, D., M. Alcorn, D. Alofs, R. Anderson, J. Carstens, D. Hagen, R. Hopkins, J. Schmitt, M. Trueblood, and W. Walker, 1986: UMR cloud simulation facility, DNA, MOffet Field, CA (Feb. 25-27).

   b. Hagen, D.E., M. Trueblood, and D.R. White, 1987: UMR combustion aerosol facility, DNA, Mission Research Corp., Santa Barbara, CA (April 7-9)

   c. Hagen, D.E., D.R. White, 1987: UMR cloud chamber experiments, DNA, Pacific-Sierra Research Inc., Los Angeles, CA (Dec. 8, 1987)

9. 1987 CRDEC Conference on Obscuration and Aerosol Research, 22-26 June, Aberdeen, MD

   White, D.R., J.L. Kassner, J.C. Carstens, D.E. Hagen, J.L. Schmitt, D.J. Alofs, A.R. Hopkins, M.B. Trueblood, W.L. Walker, M.W. Alcorn, 1987: Measurement of the condensation coefficient of water in the UMR cloud simulation chamber, Proc. 1987 CREDC Conf. on Obscuration and Aerosol Res., Aberdeen, MD (1988)

10. American Association for Aerosol Research 1987 Annual
    Meeting, Seattle, WA

    Poster Session: White, D., M. Alcorn, D. Alofs, J.
    Carstens, R. Hopkins, J. Kassner, J. Schmitt, and M.
    Trueblood, "The UMR cloud simulation facility:
    measurement of the condensation coefficient of water

11. Missouri Academy of Science, April 1987, Jefferson City,
    MO

    White, D., Measurement of the condensation coefficient
    of water in the UMR cloud simulation chamber

B. Refereed Articles

1. White, D.R., J.L. Kassner, J.C. Carstens, D.E. Hagen,
   J.L. Schmitt, D.J. Alofs, A.R. Hopkins, M.B. Trueblood,
   M.W. Alcorn, W.L. Walker, 1987: University of Missouri-
   Rolla cloud simulation facility: Proto II chamber, Rev.
   Sci. Instrum., 8(5), 826-834

2. Hagen, D.E., D.R. White, D.J. Alofs, 1988: Condensation
   method for humidity measurement in the UMR cloud
   simulation chamber, accepted for publ., J. Nat. Bureau of
   Standards.

3. Hagen, D.E., M.B. Trueblood, and D.R. White, 1988:
   Hydration properties of combustion aerosols, accepted for
   publ. Aerosol Sci. & Techn.

4. Hagen, D.E., D.R. White, M.B. Trueblood, J.L. Schmitt,
   J.C. Carstens, D. Alofs, 1988: Measurements of a
   condensation coefficient for water in the UMR cloud
   simulation chamber, submitted to J. Atmos. Sci., (March
   1988)

In preparation

5. Carstens, J.C., D. Alofs, and D.E Hagen, 1988: Theory of
   cloud drop growth in the continuum, to be submitted to
   Atmos. Res.

C. UMR Technical Report

   White, D.R., J.L. Kassner, M.W. Alcorn, D.J. Alofs, J.C.
   Carstens, D.E. Hagen, A.R. Hopkins, J.L. Schmitt, M.B.
   Trueblood, and W.L. Walker, 1986: UMR cloud simulation
   facility, Techn. Rep., UMR, Rolla, MO, 56 pp.

D. Seminars

1. J.C. Carstens, D.R. White, and J.L. Schmitt: The cloud
   simulation simulation facility at UMR, given to McDonnell
   Douglas Res. Lab, March 20, 2987

81

2. J.C. Carstens, D.R. White, and J.L. Schmitt: The cloud
    simulation facility at UMR, given to the St. Louis
    Chapter AMS, March 19, 1987

3. J.C. Carstens, Theory of Drop Growth, given to St. Louis
    University Meteorology, March 19, 1987

4. D.R. White, UMR cloud simulation facility, given to
    Atmos. Sci. Lab, White Sands Missile Range, Dec. 7, 1987

VII. REFERENCES

Alofs, D., M.B. Trueblood, D.R. White, and V.L. Behr, 1979: Nucleation experiments with monodisperse NaCl aerosols, J. appl. Meteor., 18(9), 1106-1117.

Anderson, J.B., J. Hallett, and M. Beesley, 1981: An extended classical solution of the droplet growth problem, NASA TM82392, Marshall Space Flight Center, AL, 42.

Baker, M.B., R.E. Breidenthal, T.W. Choularton, and J. Latham, 1984: The effects of turbulent mixing in clouds. J. Atmos. Sci. 41, 229-304.

Barnes, G.T., 1978: Insoluble monolayers and the evaporation coefficient for water, J. Coll. Int. Sci. 65, 566-572.

Bigg, K., 1986: Discrepancy between observation and prediction of concentrations of cloud condensation nuclei. Atmos. Res. 20, 81-86.

Bird, R.B., W.E. Stewart, and E.N. Lightfoot, 1960: Transport Phenomena. Wiley, 779.

Blyth, A.M., and J. Latham, 1985: An airborne study of vertical structure and microphysical variability within a small cumulus. Quart. J. Roy. Meteor. Soc. 10, 773-792.

Bullrich, K., G. Hanel, 1978: Effects of organic aerosol constituents on extinction and absorption coefficients and liquid water contents of fogs and clouds, Pageograph, 116, 243-301.

Cammenga, H.K., 1980: Evaporation mechanics of liquids. Current Topics in Materials Science, Ed. E. Kaldis, 5, North Holland.

Carstens, J., 1979: Drop growth in the atmosphere by condensation: application to cloud physics. Adv. Coll. Int. Sci. 10, 285-314.

Carstens, J.C., and J. Podzimek, and H. Andriambeloma, 1986: Assessment of the impact of insoluble and surface active pollutants on fog evolution. Preprints, 2, Conf. on Cloud Phys., Snowmass CO, AMS, 32-35.

Chodes, N.J., J. Warner, and A. Gagin, 1974: A determination of the condensation coefficient of water from the growth rate of small droplets. J. Atmos. Sci. 31, 1351-135 .

Davis, E.J., 1983: Transport phenomena with single aerosol particles. Aerosol Sci. Tech. 2, 121-129.

Derjaguin, B.V., V.A. Fedoseyev, and L.A. Rosenzweig, 1966: Investigation of the adsorption of cetyl alcohol vapor and the effect of this phenomenon on the evaporation of water drops, J. Coll. Int. Sci., 22, 45-50.

Derjaguin, B.V., L.F. Leonov, S.V. Mogilat, and V.M. Borisova, 1982: Dependence of water condensation coefficient on degree of interface coverage by cetyl alcohol monolayer, Koll. Zhurnal, 44(5), 877.883.

Derjaguin, B.V., Y.S. Kurghin, S.P. Bakanov, and K.M. Merzhanov, 1985: Influence of surfactant vapor on the spectrum of cloud drops forming in the process of condensation growth, Langmuir, 1(3), 278-281.

Dickenson, E., 1978: A hard disk fluid model of monolayer permeation and evaporation resistance, J. Coll. Int. Sci., 63(3), 461-471.

Fitzgerald, J.W., 1970: A re-examination of the classical theory of the growth of a population of cloud droplets by condensation. Preprints, Conf. on Cloud Phys., Ft. Collins, CO, AMS, 111-114.

Fletcher, N.H., 1962: The Physics of Rain Clouds, Cambridge, 386.

Fukuta, N., and L.A. Walter, 1970: Kinetics of hydrometeor growth from a vapor spherical model. J. Atmos. Sci. 26, 1160--1172.

Fukuta, N., and L.A. Walter, 1972: Reply (to Carstens), J. Atmos. Sci. 29, 591-592.

Garnier, J.P., Ph. Ehrhard, and Ph. Mirabel, 1987: Water droplet growth study in a continuous flow diffusion cloud chamber. Atmos. Res. 21, 41-52.

Garrett, W.D., 1978: The impact of organic material on cloud and fog processes, Pageograph, 116, 316-334.

Gill, P.S., T.E. Graedel, and C.J. Weschler, 1983: Organic films on atmosphric aerosol particles, fog droplets, cloud droplets, raindrops, and snowflakes, Rev. Geophys. and Space Phys., 21(4), 903-920.

Graedel, T.E., and C.J. Weschler, 1981: Chemistry within aqueous atmospheric aerosols and raindrops, Rev. Geophys. and Space Phys., 19(4), 505-539.

Hagen, D.E., 1979: A numerical cloud model for the support of laboratory experimentation. J. Appl. Meteor. 18, 1035-1043.

Hagen. D.L., 1987: UMR cloud simulation studies of droplet growth: investigation of the condensation coefficient. Preprints, 2, Conf. on Cloud Physics, Snowmass CO, AMS, 1-8.

Hagen, D.E., D.R. White, and D.J. Alofs, 1988: Condensation method for humidity measurement in the UMR cloud simulation chamber, accepted J. National Bureau of Standards, 1988.

Hickman, K., 1966: Reviewing the evaporation coefficient, Desalinization 1, 13-29.

Jensen, J.B., and M.B. Baker, 1986: An observational study of cloud droplet spectra in continental cumulus clouds. Preprints, 2, Conf. on Cloud Physics, Snowmass, CO, AMS, 145-148.

Jonas, P.R., and B.J. Mason, 1982: Entrainment and the droplet spectrumin cumulus clouds. Quart. J. Roy. Meteor. Soc. 108, 857-869.

Kennard, E.H., 1938: Kinetic theory of gases. McGraw Hill, 475.

LaMer, V.K., 1962: "Retardation of evaporation by monolayers: transport processes", Academic Press, pp. 277.

Lucassen-Reynders, E.H., and J. Lucassen, 1969: Properties of capillary waves, Adv. Coll. Int. Sci., 2, 347-395.

Maa, J.R., 1983: The role of interfaces in heat transfer processes. Adv. Coll. Int. Sci. 18, 227-280.

Manton, M.J., and J. Warner, 1982: On the droplet distribution near the base of cumulus clouds. Quart. J. Roy. Meteor. Soc. 108, 917-928.

Mason, B.J., and P.R. Jonas, 1984: The evolution of droplet spectra and large droplets by condensation in cumulus clouds. Quart J. Roy Meteor. Soc. 100, 23-38.

Mills, A.F., and R.A. Seban, 1967: The condensation coefficient of water. Int. J. Heat Mass Transfer 10, 1815-1827.

Monchick, L., and H. Reiss, 1954: Studies of evaporation of small drops. J. Chem. Phys. 22, 831-836.

Mozurkewich, M., 1986: Aerosol growth and the condensation coefficient of water: A review. Aerosol Sci. Tech. 3, 177-185.

Narasawa, U., and G.S. Springer, 1975: Measurements of evaporation rates of water, J. Coll. Int. Sci., 50(2), 392-395.

Palmer, H.J., and A. Bose, 1981: Bulk phase and intrinsic interfacial resistance to evaporation under a vacuum, J. Coll. Int. Sci., 84(2), 291-300.

Paluch, I.R., and C.A. Knight, 1986: Does mixing promote cloud droplet growth?. J. Atmos. Sci. 43, 1994-1998.

Paluch, I.R., and C.A. Knight, 1987: Reply (to Telford). J. Atmos. Sci. 44, 2355-2356.

Plooster, M., 1979: Atmospheric cloud physics laboratory simultion system: mathematical description, Report under NASA contract NAS8-32688.

Pruppacher, H.R., and J.D. Klett, 1978: Microphysics of clouds and precipitation. Reidel, 714.

Reif, F., 1965: Fundamentals of Statistical and thermal physics. McGraw Hill, 651.

Rubel, G.O., and J.W. Gentry, 1984: Measurements of the kinetics of solution droplets in the presence of adsorbed monolayers: determination of water accommodation coefficients, J. Phys. Chem., 88, 3142-3148.

Rubel, G.O., and J.W. Gentry, 1985: Measurement of water and ammonia accommodation coefficients at surfaces with adsorbed monolayers of hexadecanol, J. Aerosol Sci., 16(6), 571-574.

Sageev, G., R.E. Flagan, J.H. Seinfeld, and S. Arnold, 1986: Condensation rate of water on aqueous droplets in the transition regime. J. Coll. Int. Sci., 113(2), 421-429.

Schmitt, J.L., 1981: Precision expansion cloud chamber for homogeneous nucleation studies, Rev. Sci. Instrum. 52(11), 1749-1754.

Sherwood, T.K., R.L. Pigford, and C.R. Wilke, 1975: "Mass Transfer", McGraw Hill, NY, pp. 182.

Stahley, D.O., 1972: Heat conduction in the vicinity of a growing droplet. J. Atmos. Sci., 206-208.

Telford, J., and S.K. Chai, 1980: A new aspect of condensation theory. Pure Appl. Geophys. 118, 720-742.

Telford, J., and P.B. Wagner, 1981: Observations of condensation growth determined by entity type mixing. Pure Appl. Geophys. 119, 934-965.

Toosi, R., and T. Novakov, 1984: The lifetime of aerosols in ambient air: consideration of the effects of surfactants and chemical reactions, Atmos. Env., 18(0), 1-7.

Wagner, P.E., 1982: Aerosol growth by condensation. Topics in Current Physics, Aerosol microphys II (Ed. W.H. Marlow), Springer-Verlag, Berlinn, 129-178.

Warner, J., 1969: The microstructure of cumulus cloud. Part II. The eifect on droplet size distribution of the cloud nucleus spectrum and updraft velocity. J. Atmos. Sci. 26, 1272-1284.

wnite, D., J.L. Kassner, J.C. Carstens, D.E. Hagen, J.L. Schmitt, D.J. Alofs, A.R. Hopkins, M.B. Trueblood, M.W. Alcorn, and W.L. Walker, 1987: University of Missouri-Rolla cloud simulation facility: Proto II chamber. Rev. Sci. Instr. 58, 826-834.

APPENDIX A

University of Missouri-Rolla Cloud
Simulation Facility: Proto II Chamber

University of Missouri–Rolla cloud simulation facility: Proto II chamber   A1

Daniel R. White

Department of Engineering Mechanics and Graduate Center for Cloud Physics Research, University of Missouri–Rolla, Rolla, Missouri 65401

James L. Kassner

Dexter D. Hulsart Company, Inc., P. O. Box 1878, Tuscaloosa, Alabama 35401

John C. Carstens, Donald E. Hagen, and John L. Schmitt

Department of Physics and Graduate Center for Cloud Physics Research, University of Missouri–Rolla, Rolla, Missouri 65401

Darryl J. Alofs

Department of Mechanical Engineering and Graduate Center for Cloud Physics Research, University of Missouri–Rolla, Rolla, Missouri 65401

Alfred R. Hopkins, Max B. Trueblood, and Max W. Alcorn

Graduate Center for Cloud Physics Research, University of Missouri–Rolla, Rolla, Missouri 65401

William L. Walker

Kel-tec Corp., 84 Hill Avenue, Fort Walton Beach, Florida 32548

The Graduate Center for Cloud Physics Research at UMR has developed a cloud simulation facility to study phenomena occurring in terrestrial clouds and fogs. The facility consists of a pair of precision cooled-wall expansion chambers along with extensive supporting equipment. The smaller of these chambers, described in this article, is fully operational, and is capable of simulating a broad range of in-cloud thermodynamic conditions. It is currently being used to study water drop growth and evaporation for drops nucleated (activated) on well-characterized aerosol particles. Measurements have been made not only for continuous expansions (simulated updraft) but also for cyclic conditions, i.e., sequences of expansion-compression cycles resulting in alternating drop growth and evaporation. The larger of the two cloud chambers is nearing completion and will provide a broader range of conditions than the smaller chamber. The facility is supported by a fully implemented aerosol laboratory which routinely produces well-characterized condensation nuclei. The aerosol laboratory contains extensive instrumentation designed to both shape and measure the size distribution and nucleating characteristics of the generated aerosol. The cloud simulation facility also includes a humidifier to bring an air sample to a known humidity before it is put into the cloud chamber. A systematic program to infer effective condensation coefficients (of water vapor on cloud drop) under a variety of well-controlled simulated in-cloud conditions is now under way. Analysis of current experiments with standard drop growth theory indicates a variation of condensation coefficient with observation time, with values sufficiently low to explain one of the current mysteries in cloud physics: *viz.*, the broad spread of drop sizes observed in natural clouds. This article includes a description and performance specifications of the smaller cloud simulation chamber.

INTRODUCTION

During the past 25 years the Graduate Center for Cloud Physics Research at the University of Missouri–Rolla has been engaged in a balanced theoretical and experimental study of the microphysical processes active in atmospheric clouds and fogs. In 1968 a program was initiated to develop a laboratory facility for simulating cloud thermodynamic processes. Two cooled-wall expansion cloud chambers are the heart of the resulting UMR cloud simulation facility. The two chambers, designated Proto II and Romulus, are designed to subject a sample of moist aerosol-laden air to a predetermined profile of temperature and pressure approximating those observed during various processes which occur in the atmosphere. This article describes the smaller Proto II chamber. A summary of the chamber operating parameters is given in Table I.

Cooling the walls at the same rate as the gas in the chamber greatly reduces the exchange of heat between the sample and the chamber walls, thereby minimizing thermal

TABLE I. Proto II chamber operating parameters.

Temperature		
Range:		40 to − 40 °C
Control:		
Holding:	At fixed temperature rms deviation from spatial average, 40 sensors	0.030 °C
Cooling:	Maximum rate	10 °C//min
	Wall temperature lag from control point rms deviation from spatial average	0.01 °C/(°C/min)[a]
		0.080 °C at 6 °C/min
		0.040 °C at 3 °C/min
Temperature measurement resolution		0.001 °C
Temperature measurement accuracy		± 0.005 °C
Pressure		
Reference pressure absolute accuracy:		± 0.01%, dead weight pressure gauge
Dynamic sensor range:		0–15 kPa differential
Resolution:		± 0.006 kPa
Control:		
Holding:	Standard deviation with time about average	0.065 kPa
Expansion:	Maximum rate	0.5 kPa/s (12 °C/min wet adiabatic)
	Offset from command	0.065 kPa
	Standard deviation with time	0.05 kPa
Wall cooling method		Thermoelectric modules plus fluid thermostating of heat sinks
Sensitive volume dimensions		
Diameter:		46 cm
Height:		
One section:		61 cm
Two sections:		122 cm

[a] Cooling rate.

FIG. 1. Flow diagram of UMR simulation facility.

uncertainties. The facility thus provides an opportunity to observe and study various atmospheric processes under prolonged, controlled, measurable, and repeatable conditions. No comparable facility exists elsewhere, nor to our knowledge is one being planned elsewhere.

An extensive array of support equipment has also been developed. This includes several types of aerosol generators for producing both water soluble and insoluble particles; as well as equipment to modify and characterize the generated aerosol based on both size and ability to nucleate water drops or ice crystals. Measurements can be made on cloud droplets formed in the chambers both *in situ* and by extraction of the sample from within the chamber. Figure 1 shows a flow diagram for the facility with arrows tracing the progress of an aerosol sample flowing through the system. The details of the support equipment either have been[1-3] or will be reported elsewhere.

The philosophy behind this facility embraces the recognition that the development of a cloud is governed by a combination of microphysical and dynamic processes. The simulation facility is intended to investigate the microphysical 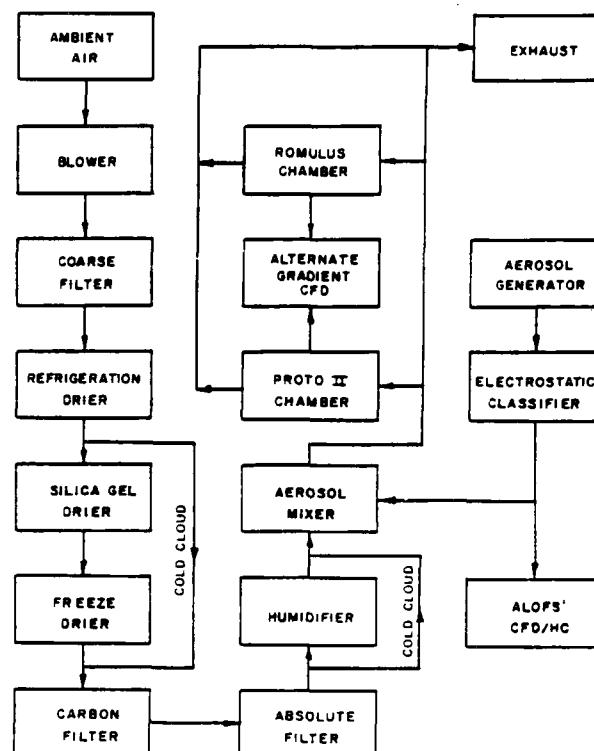processes with the conviction that both types of processes must be understood individually before there is any realistic hope of a clear understanding of their combined interactive effects on the cloud.

Some areas of study under current or proposed investigation include: warm and cold cloud droplet growth, aerosol scavenging by cloud droplets, ice nucleation and growth, collision coalescence, memory effects due to cycles of condensation and evaporation, and optical properties of clouds.

I. PROTO II CHAMBER

A. Physical description

The Proto II chamber is a cooled-wall expansion cloud chamber. The chamber is a 10-sided vertical cylinder with a flat to flat internal dimension of approximately 46 cm (Fig. 2). It is designed to be operated with internal heights of 61 or 122 cm. Initial experiments have been done in the 61-cm configuration.

The design concept for this chamber is to provide the interior wall surfaces with a means of external temperature control so that a temperature match between the walls and gas is maintained as the gas temperature is changed by expansion or compression. In this way the massive flux of heat to or from the walls found in an expansion cloud chamber[4] is avoided, and the interior temperature remains well defined. The chamber can be programmed to carry out expansions at any rate slower than the maximum design rate, stop and hold constant temperature and pressure, reverse and recompress, or any combination of these while maintaining accurate
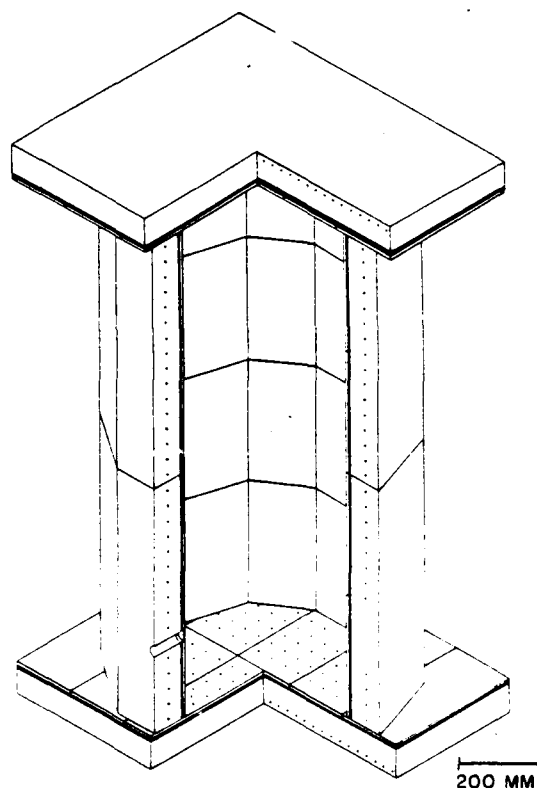
FIG. 2. Proto II chamber.

200 MM

FIG. 3. Cross section of chamber wall.

knowledge of the thermodynamic parameters of the sample.

The chamber can operate with interior wall temperatures between + 40 and − 40 °C. Considerable care has been taken to ensure uniform interior wall temperature. Temperature control is based on the use of thermoelectric modules (TEM's) to pump heat between the thin (0.96 cm) inner wall and the thick (7.6 cm) fluid-thermostated outer wall. Figure 3 shows a cross section of the chamber wall. It should be noted that the inner wall plates are actually two aluminum plates (6.35 and 3.18 mm) laminated together with a heat-cured sheet adhesive. In addition to permitting the use of inserts for the sockets into which the mounting studs screw, the reduced thermal conductivity in the adhesive bond line causes an increased thermal resistance for transfer of heat from the inner chamber surface to the TEM interface. This results in a significant smoothing of the temperature over the inner chamber surface compared to that observed when single solid plates of equal total thickness were tested. The beveling of the plate edges is done because otherwise the row of TEM's near the plate edge would be cooling a greater mass than the other TEM's, resulting in a slower response at the plate edge than the center.

TEM's were chosen because they can provide a more spatially uniform temperature than would be possible, for example, by circulating a liquid through passageways in the walls of the chamber. Moreover, the heat pumping of the TEM's can be precisely controlled by direct electrical
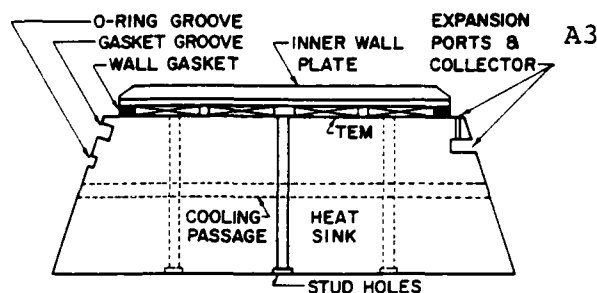
means. The area controlled by a single control loop has been kept small (15.25 × 30.5 cm) with each control loop (40 for the 61 cm height; 60 for the 122 cm height) having its own interior wall temperature sensor, analog control circuit, programmable switching power supply, and set of TEM's. In this chamber each interior wall plate has one control loop.

The TEM's can cool the inner wall surface at rates up to 10 °C/min for temperatures from + 40 to 10 °C below the temperature of the heat sink. Below this range the maximum cooling rate decreases until the lowest temperature of 35 °C below the heat sink temperature is reached. Maximum heating rate exceeds 10 °C/min for all temperatures. At present the chamber at 20 °C regularly shows an rms spread of 0.01 °C or less in the temperature of the 40 measured control sections with a peak-to-peak spread of less than 0.050 °C. For the interior walls 30 °C below the heat sink temperature, the rms increases to 0.075 °C and the peak-to-peak spread approaches 0.5 °C.

B. Temperature measurement

Temperatures are measured using transistor thermometers developed and constructed by the electrical engineering staff of this research center. The thermometers use the temperature characteristics of the base-to-emitter junction of a transistor as the sensor. Their useful range of ± 50 °C covers the temperature range of interest for work with the simulation facility.

The system is calibrated to an output of 0.000 V dc at 0.0 °C and a gain of − 0.100 V dc/°C. The slight quadratic nonlinearity (0.07 °C maximum error) is compensated for by computer corrections when the thermometers are read. The system has a resolution of ± 0.001 °C and can be calibrated to ± 0.005 °C. Long-term zero point drift for 6–12 months is typically less than ± 0.010 °C.

Thermometer calibration is based on a water triple point cell and National Bureau of Standards gallium melting point cell. A commercial electronic quartz thermometer and a commercial direct reading platinum resistance thermometer are used as transfer and interpolation standards.

The chamber wall plate and heat sink transistor sensors are mounted in a threaded brass rod (1.3 cm long and 0.5 cm in diameter) which can be screwed directly into flat bottom-

tapped threaded wells in either the interior wall plate (Fig. 4) or the heat sink. The sensor threads are coated with a small amount of thermal grease which assures maximum thermal contact between the sensor and the part being measured. One sensor is located in the center of each interior wall plate and there is one heat sink sensor for every two interior wall plates.

The facility has 128 thermometers of which 96 can be read directly by the primary control and data-acquisition computer (NOVA 840; Data General Corp.) at a rate of 40 Hz. Sixty of these 96 channels are assigned to the chamber inner wall plate thermometers and 14 to chamber heat sink thermometers. The remaining 22 channels are assigned to thermometers distributed throughout the rest of the facility in such locations as the sample humidification system, various fluid coolant loops, etc.

C. Temperature control

The interior surface temperature of the chamber wall is controlled by separate analog controller circuits for each 15.25×30.5-cm control section of the wall. The controllers are proportional with both integrator and differentiator components. Each controller has two inputs, one from the output of the thermometer mounted in the wall section and the second from the D/A (digital-to-analog) channel of the NOVA 840 control computer (see Sec. II A), which is proportional to the desired wall temperature. The controller generates an error signal by comparing the two signals and, after modifying the error signal with the integrator and differentiator contributions, outputs the result as a command signal to the appropriate programmable switching power supply which then causes the wall section to heat or cool as necessary to drive the error signal to zero. This closed-loop system has a settling time of approximately 30 s.

The desired temperature signal is provided by the control computer as a function of time through a dedicated D/A channel which is updated every 0.5 s. The desired temperature is calculated by linear interpolation between points stored in a computer file. The particular file consisting of 1001 time–temperature–pressure sets is entered as part of the chamber closing sequence after the initial conditions and actual sample characteristics are known, and the appropriate file can be selected from the available control file library.
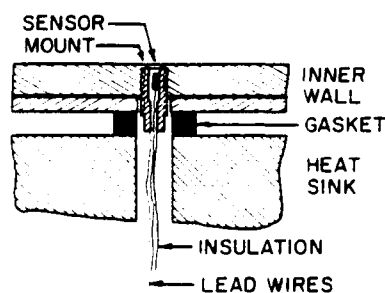
The thermal mass of the inner wall plate introduces a natural delay into the response of the chamber to changes in dT/dt, where T is the temperature. This appears as a lag when the rate is increased and an overshoot when the rate is reduced. However, the response of the chamber is sufficiently repeatable that temperature data collected during previous expansions can be used to modify the control signal to the controllers to provide the required anticipation which minimizes both lags and overshoots.

Even the uncorrected response of the chamber for a typical 10 °C/min linear cooling profile shows a maximum initial error between the measured and desired temperatures of less than 0.8 °C. This decreases to between 0.15 and 0.18 °C within 15 s after the beginning of the cooling and remains relatively constant during the period of linear temperature decrease. At the end of the cooling period there is an overshoot of approximately 0.5 °C with recovery in less than 10 s.

The temperature of the chamber heat sink is controlled by circulating fluid from a constant temperature bath (Forma Scientific, Model 2075A) through passages drilled in the heat sinks expressly for this purpose (Fig. 3). The flow pattern in the chamber heat sink consists of opposing flows in adjacent passages. This ensures a more uniform temperature distribution by averaging the effects of the increase in fluid temperature between inlet and outlet ports. Response of the heat sink and circulator bath to changes in desired temperature is sufficiently slow to preclude effective changes during the course of most individual experiments.

D. Pressure measurement

Pressure is measured in the chamber by a differential strain gauge pressure transducer with its reference side connected to the sensing volume of a vacuum-referenced precision (0.01%) dead weight gauge (Ruska, Model 2465, 0–103 kPa). The pressure sensor is located external to the chamber and connected to the sensitive volume of the chamber by a 3.17-mm-i.d. tube and a hole drilled through the chamber wall. The response of the transducer and connecting tube is much faster than any rates of pressure changes within the design range of the chamber. This arrangement simplifies the exchange of transducers so that the range of the transducer can be matched to the anticipated peak-to-peak pressure change during a particular experiment. Therefore, the sensitivity of the system can be maximized for each type of experiment. The reference pressure can also be varied to center the transducer range on the anticipated absolute pressure range of the chamber. The pressure port is located in one of the lower side wall sections of the chamber.

Calibration of the differential pressure transducers is performed using two of the precision dead weight pressure gauges to apply accurately known pressures to each side of the transducer. At each setting (when both gauge pistons are floating) the difference in the settings is entered into the computer and the output signal of the transducer recorded by the computer through the same A/D (analog-to-digital) system used for experimental readings. Once the full range of calibration readings has been recorded, a least-squares cubic

FIG. 4 Mounting of thermometers in chamber inner wall.

curve is fit to the data. Calibration data are taken for pressure changes in both directions.

During operation, one of the dead weight gauges is covered by a bell jar with a vacuum pump connected to the volume above the piston. The reference side of the transducer is connected to the bottom side of the piston and a precision fine metering valve is used to bleed filtered air into the transducer reference lines. The metering valve is adjusted so that the amount of bleed air entering the system just balances that which is lost by flow past the piston to the vacuum in the bell jar. In this way a steady-state condition with the piston floating can be maintained for periods of time in excess of those required to carry out an experiment.

The accuracy of the system is three parts in 10^4. The effects of electrical noise in the system are reduced by reading the pressure transducer signal 50 times at a 10-kHz rate with the high-level A/D unit of the control computer (NOVA 840) and averaging the readings.

E. Pressure control

The cloud chamber pressure versus time control profile is designed to cause the gas temperature to track the chamber wall temperature (see Sec. I B). Pressure control is maintained by removing or adding air to the chamber by means of isoentropic expansions or compressions. While the amount of air added during compression is restricted to very small volumes the amount removed during expansions can be quite large. The rate of air flow into or out of the system is controlled by an 8-bit digital valve (Digital Dynamics, Inc.). This valve has eight parallel orifices which are individually controlled and have their individual flow rates arranged in a binary sequence. That is, if the orifices are numbered $n = 0,1,2,....,7$, the relative flow through a given orifice for a given set of inlet and outlet pressures is proportional to 2^n. Each bit of the valve is controlled by the corresponding bit of an 8-bit digital word from the NOVA 840 control computer.

During operation the chamber pressure is measured, the desired chamber pressure one update period in the future (normally 1 s) is determined from the preloaded time-temperature-pressure control profile, and the required valve setting is calculated based on pressures and required pressure changes. The valve setting is converted to an 8-bit digit word and sent to the digital output controlling the valve. A major advantage of this system is the speed of valve response since the valve setting can be changed from fully closed to fully open, or anything in between, in a single jump. This reduces the peak-to-peak oscillations in pressure, associated with the control system, by a factor of 50 compared to a former motor-driven rotary valve system. The sign of the calculated pressure change determines whether the expansion or recompression system is used.

F. Expansion system

The expansion system of the chamber removes air radially from the sensitive volume through a series of small ports (16 0.79-mm-diam holes per 61 cm of height) located along

each of the ten vertical joints between side wall heat sink sections (Fig. 5). The individual flows are combined and directed to the expansion manifold located under the chamber. The design provides balanced flow in all the lines so that air can be removed or introduced into the chamber uniformly at all ten joints.

G. Optical systems

A schematic view of the optical system for the chamber is shown in Fig. 6.

1. Chamber windows

The optical cloud diagnostic techniques outlined below access the chamber via 2.3-cm (clear aperture) windows. The chamber has three windows: two directly opposite each other and one at 72° from the forward direction.

All window assemblies are of the same design (Fig. 7). Each has a 1.6-mm-thick sapphire window, mounted in Delrin with an O-ring seal to the inner wall, which is approximately coplanar with the inner surface. Sapphire was selected because it is very tough and has an unusually high thermal conductivity for a transparent material. The sapphire windows are flat to one wavelength, have been cut for minimum birefringence, and are coated. About 4 mm behind the sapphire wall window provisions are made to mount another optical element. This can be a prism, lens, or another sapphire window. The entire system is mounted in a Delrin cylinder that is easily removed without disassembly of any other part of the chamber.

The temperature of the window can be controlled to track the walls. This is accomplished by allowing thermostated carbon dioxide gas to flow between the inner and wall plate windows; the gas temperature determines the temperature of the wall window. A transistor thermometer sensor is in contact with the edge of the wall window and its signal is used for control. Very cold carbon dioxide gas is generated by the phase change from liquid to gas in the compressed gas cylinder and a subsequent nozzle expansion. The gas is then heated by a controlled electrical resistance heater to the required temperature and allowed to flow through the space between the windows.
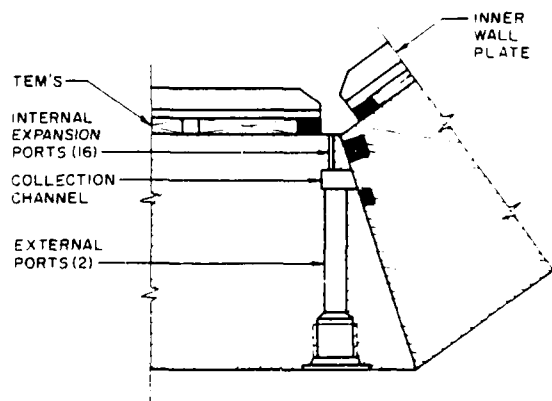

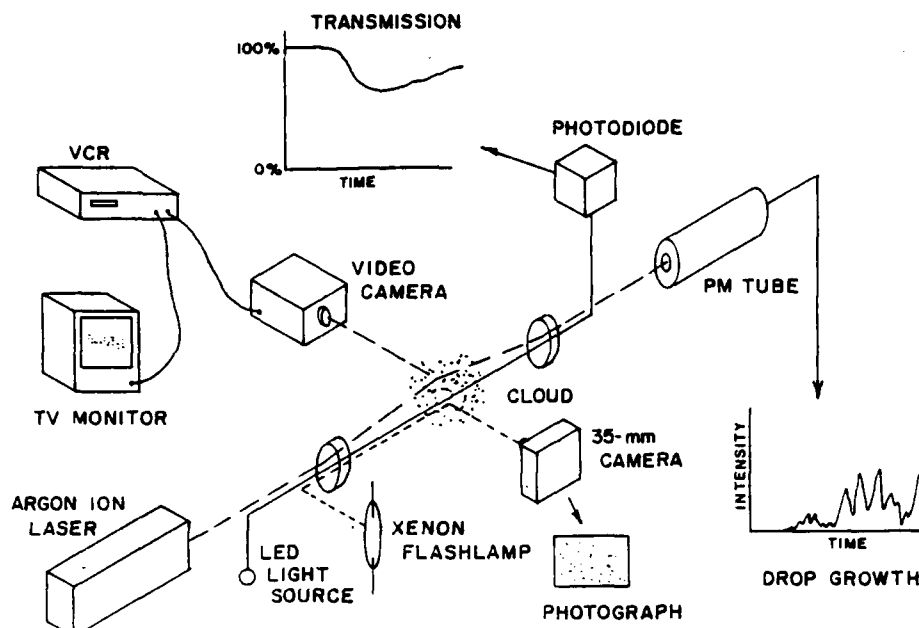FIG. 5 Expansion manifold in chamber wall

FIG. 6. Schematic view of optical systems.

2. Optical table

The optical diagnostic system for the chamber is mounted on a vibration isolated optical table made of 8-in. iron pipe welded into a horizontal "H" configuration and filled with sand. An argon-ion laser sits on the top of this structure and its expanded beam is directed into the chamber with mirrors mounted on the legs of the "H" which extend around two sides of the chamber.

3. Photographic/video

The cloud in the chamber can be either photographed or viewed with a low-light-level TV camera. Photographs are taken with a motorized Nikon (F3) camera that is computer controlled. An $f/3.5$ Macro Nikkor lens is used with a resolving power of about 150 line pairs/mm (at the film) and a

FIG. 7 Observation window design.

depth of field of about 1 cm in the center of the chamber. The camera window is at 72° from the foward direction of the laser beam. The film is Kodak Tri-X or Plus-X developed to ISO (ASA) 1600 or 400, respectively, in Diafine developer. Illumination for the photography is provided by a xenon flash lamp powered by a commercial photography electronic flash power supply (200, 400, or 800 J/flash with a 1.4-s, maximum recycle time). The flash lamp light beam is shaped with lenses and a slit into a vertical sheet of light in the chamber. All drops in the light are in focus for the camera lens (in the depth of field) and only these drops are illuminated and register on the film. Calibration of the camera magnification and the illumination volume yields the drop count per cm^3 in the volume (integrated on the film).

A TV camera with a low-light-level silicon tube can be used in place of the photographic camera. The laser beam that is used for Mie scattering measurements provides illumination. Various lenses are available for the camera with views ranging from about 6 cm diameter in the center of the chamber to an extreme wide-angle view obtained by a fisheye lens. This latter arrangement has poor resolution; the other configurations will detect individual cloud drops. The TV camera image may be recorded on a standard VHS video cassette recorder.

4. Optical attenuation

The attenuation system measures the attenuation (or transmission) of a light beam across the chamber. A modified commercial light-emitting diode (LED) provides the light source. The wavelength of approximately 670 nm (20 nm bandwidth) includes few water vapor lines. The small LED source is collimated to a 1-cm beam diameter and projected across the chamber to a silicon diode detector (1° field of view). The intensity-controlled LED source is electroni-

cally chopped at 1 kHz and the detector electronics synchronously rectify this signal. The system is quite immune to background radiation and noise. The light beam is introduced and extracted from the chamber by wavelength selective beam splitters that also transmit the laser beam for Mie scattering. The accuracy of the system is three parts in 10^4.

5. Mie scattering system

The Mie scattering from a cloud of drops is used to determine the mean size of the drops as a function of time for monodispersed clouds. A 488-nm argon-ion laser beam is introduced into the chamber via a prism at an angle of 2°. A similar prism arrangement on the other side of the chamber views at 2°. Thus the PMT (photomultiplier tube) detector sees the Mie scattering from the cloud drops at 4° from the forward direction. The light scattered from a water sphere (calculated by Mie scattering theory) at 4° is shown in Fig. 8. A similar graph is obtained from the output of the PMT detecting light scattered from a cloud of monodispersed drops growing in time. Comparison of the two graphs (intensity versus radius and intensity versus time) yields radius versus time for the drops in the cloud. One should note in Fig. 8 a very valuable feature of the scattering at 4°. The graph not only displays oscillations of the scattering intensity as a function of radius but reveals that the envelope of the maxima of the oscillations is also modulated. In practice very often the first oscillations in Fig. 8 are difficult to detect due to noise or other factors. The modulation of the envelope allows one to unambiguously correlate a particular oscillation with the correct drop radius.

6. Scanning system

A device to detect, count, and size drops of a polydispersed cloud in a volume of about 1 cm³ in the center of the chamber is under development. It uses the four strong lines from an argon-ion laser in an integrated and focused beam. The focused spot then is scanned in X, Y, and Z through the
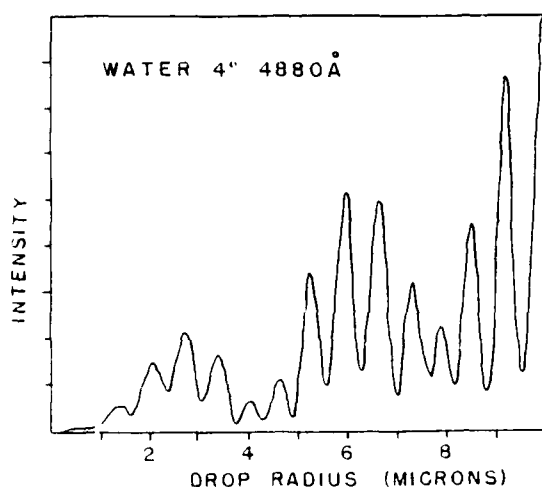

Fig. 8 Four degree Mie scattering intensity vs droplet radius (theoretical calculation)

sample volume. The resulting scattering from the drops is integrated over 15° at 90° from the incoming beam and the height of the pulses are measured. An approximate linear relation has been found theoretically for the height of the pulse as a function of drop size. This system will be mounted at the midpoint of the 122-cm chamber configuration.

II. COMPUTER SYSTEM

A. Proto II

The control and data-acquisition system for the Proto II chamber is build around a NOVA 840 (Data General Corp.) minicomputer (Fig. 9). Two 2.5-Mbyte moving head disk drives with removable cartridges provide on-line storage for both the operating programs and short-term data storage.

A wide-range 15-bit A/D converter with programmable gain and a cycle time of 0.025 s is used for reading temperatures and any routine data acquisition. A high-level 15-bit fixed gain A/D (0–10 V dc) which samples at 10 kHz is used to take measurements requiring a faster acquisition rate (such as the pressure transducer and optical attenuation signals). The high-level A/D can be set to sample at 20 kHz if required.

The digital I/O (input/output) has 12 16-bit channels (seven inputs and five outputs) which are TTL (transistor–transistor logic) compatible. These are used for such functions as reading the external elapsed time clock (10, 100, or 1000 Hz) or outputting on/off commands to the various valves, pumps, recorders, etc. The digital expansion valve command utilizes 8 bits of one output channel. The wall temperature control signal is transmitted through one of the eight D/A analog channels available (five 0–10 V; three ± 10 V).

The operator interacts with the system via both the terminal and the front panel switches on the central processing unit. After an experiment data can be transferred to magnetic tape ($\frac{1}{2}$-in. reels) for long-term storage or printed on the line printer (Tally T-1120). Both the magnetic tape and line printer are used to store back-up copies of the operating programs.

The computer is capable of multitasking which allows a high degree of flexibility in the chamber operation. By setting up each function such as pressure control, thermometer readings, wall temperature control, etc. as a separate task, it is easy to establish individual priorities and frequencies of performance. Also it is simple to cancel a task entirely for a given experiment. Details are given by Hagen et al.[5]

B. Support systems

While the NOVA 840 minicomputer provides control and data-acquisition functions for the simulation facility, a NOVA 3 is used for pre- and post-experiment cloud modeling, experiment preparation, and data analysis. The two minicomputers transfer data by a hardwire link. It is necessary to have a numerical model which simulates the physical processes, e.g., thermodynamics and droplet growth, that occur within the expansion chamber. (This model[6] runs on the NOVA 3.) The model is used to design and optimize
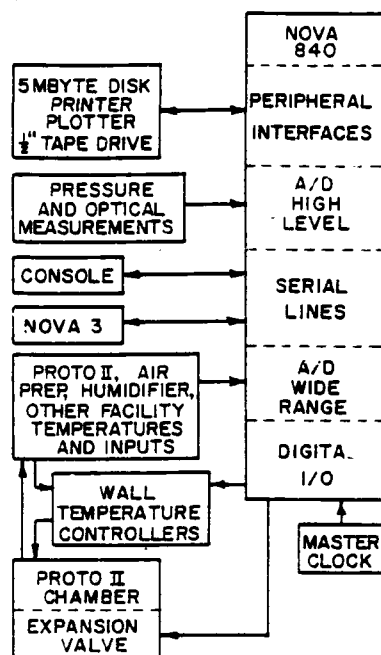
FIG. 9. Block diagram of the computer data-acquisition and control system.

experiments. i.e., choose the best aerosol concentration. expansion profile, data-acquisition times, etc. In the development of a typical experiment. the designer runs the cloud model several times to find variables (initial temperature and pressure, expansion profile, aerosol concentration. etc.) that will yield the conditions desired (e.g.. a monodisperse cloud of 4.0-μm radius at 280 K and 90.0 kPa with a growth rate of 0.2 μm/s). Computer disk files are generated with this information and then are transferred to the NOVA 840 for real time use in controlling the cloud chamber.

The NOVA 3 also plays a role in the analysis of experiments. i.e., comparing experimental observations such as droplet growth rates with theory under the known conditions. Data files containing results of the experiments are transferred from the NOVA 840 to the NOVA 3 for analysis.

The NOVA 3 also provides computer support for various other cloud simulation facility subsystems. A cold CFD (continuous flow diffusion cloud chamber) with ice on its plates is being developed. The NOVA 3 runs a numerical model that simulates the physical processes (e.g., particle motion. ice nucleation. phoretic forces. ...) that occur in this chamber. It was used for chamber design optimization studies and for data analysis. The aerosol generation and characterization laboratory uses the NOVA 3 to run an inversion program to process electric mobility classifier aerosol size distribution data. Another program is used to analyze warm (above freezing) CFD aerosol concentration versus supersaturation data to determine the volume soluble fraction spectrum of the aerosol.

III. SAMPLE PREPARATION AND CHAMBER FLUSHING

A8

A. Preparation

Samples for use in the cloud simulation chambers are produced continuously with total volumetric flow rates of 1–2 l/s. Exterior ambient air is drawn in, filtered (particles: 99.97% efficient at 0.3 μm; organics: activated carbon), and dried (refrigeration and desiccant: dew point < -40 °C) to produce clean dry air to which the required water vapor and aerosol concentrations can be added. Water vapor content is established by passing the air through a precision flowing water humidifier. (For dew or frost points below 0 °C the initial drying process is adjusted to leave the desired vapor content.) The aerosol-laden air is added to the clean moist air using a mixing ratio of 1 : 100 or less. The resulting sample is then flushed through the appropriate cloud simulation chamber.

B. Humidifier

The vapor density of the sample air for warm cloud experiments is established by means of a precision flowing-water humidifier.[8] Air is exposed to a flowing water surface under closely controlled thermal conditions and allowed to become nearly saturated at the temperature of the system.

The humidifier consists of two thick wall aluminum cylinders (98 cm high by 16.5 cm i.d.) each containing 60 7-mm-diam glass rods. The cylinders and rods are mounted vertically and water is pumped to the top of the cylinders and allowed to flow down over the surfaces of the glass rods. The air which flows around the rods is never further than 13 mm from a flowing water surface during the 30 s residence time of air in the humidifier.
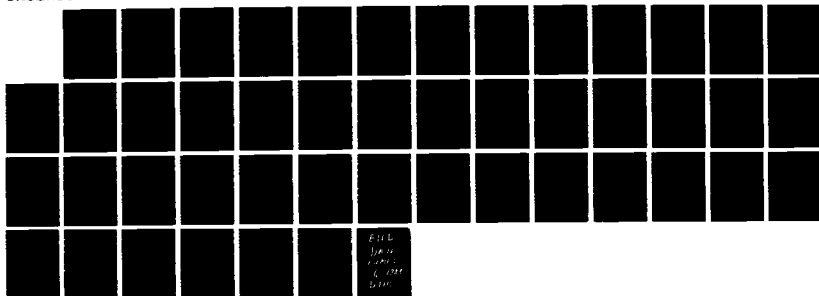
Temperatures of both the cylinders and flowing water are closely thermostated (0.010 °C peak-to-peak fluctuation during a sample flush) by a multiloop feedback control system based on transistor thermometers located in the walls of both cylinders, the water flow, and the outlet air flow. Most of the evaporation and the associated latent heat release occur in the first cylinder, so that the second cylinder acts as a fine adjustment.

Calibration of the humidifier controls, using the simulation chamber as a precision hygrometer. has shown that the actual dew point of the air at 17 °C is consistently 0.355 °C below the temperature of the outlet air flow. During normal steady-state operation of the system. the controls force the outlet air to the system set-point temperature and maintain it there with fluctuations of less than 0.010 °C peak to peak during the period of a sample flush. The error from changes in water-vapor content caused by changes in residence time due to normal variations in the sample air flow rate are smaller than those from other experimental uncertainties.

C. Chamber flushing

A sample is introduced into the chamber using top to bottom flow. It first enters the inlet manifold chamber which is located directly above the simulation chamber top section. The sample then flows into the chamber through 104 sepa-

rate ports. This technique ensures a more uniform flow of sample into the top of the sensitive volume than a single large port. It thus greatly reduces the likelihood of stagnant regions being formed in some corners of the chamber during flushing. An additional very important advantage is that each individual port is small enough to fit in the space between TEM's and does not interfere with their normal physical layout. This inlet system is duplicated as an outlet system on the bottom of the chamber where it is connected to the exhaust line.
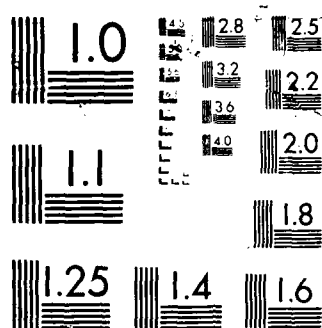
The chamber is flushed for a minimum of 15 min. Flushing typically continues until a measurement of the aerosol concentration in the chamber shows an acceptably stable value for 5 min. The sample is drawn from the chamber expansion system which is being flushed with the chamber. When both flushing conditions have been satisfied and all other chamber systems are operating normally, the chamber inlet and outlet valves are closed to seal the chamber.

At this time, pressure control of the chamber by the control computer is activated and a very slow isothermal expansion or compression brings the chamber to the desired initial pressure. A sample line which bypasses the chamber directly to the exhaust line is also opened as the chamber is closed (to allow the steady-state conditions existing in the sample preparation system to be maintained and ready for use in flushing the chamber for the next experiment).

[1] D. J. Alofs, M. B. Trueblood, D. R. White, and V. L. Behr, J. Appl. Meteorol. **18**, 1106 (1979).
[2] D. J. Alofs, J. Appl. Meteorol. **17**, 1286 (1978).
[3] D. J. Alofs and M. B. Trueblood, J. Rech. Atmos. **15**, 219 (1981).
[4] J. L. Schmitt, Rev. Sci. Instrum. **52**, 1749 (1981).
[5] D. E. Hagen, K. P. Berkbigler, J. L. Kassner, and D. R. White, in *Minicomputers and Large Scale Computations*, edited by P. Lykos, ACS Symposium Series No. 57 (American Chemical Society, Washington, DC, 1977), pp. 77–93.
[6] D. E. Hagen, J. Appl. Meteorol. **18**, 1035 (1979).
[7] D. E. Hagen and D. J. Alofs, Aerosol Sci. Technol. **2**, 465 (1983).
[8] D. R. White, A. R. Hopkins, and J. L. Kassner, in *Proceedings of the Moisture and Humidity International Symposium* (Instrument Society of America, Research Triangle Park, NC, 1985).

APPENDIX B: List of Symbols

English symbols

symbol	definition
a	drop radius
$\dot{a}$	time derivative, drop radius
B	slope of (water) saturation vapor pressure curve
D_p	particle diameter
D	diffusion coefficient, water vapor in air
e	vapor pressure of water
$e_{eq}(T)$	saturation vapor pressure of water at temperature T
K	Thermal conductivity of air
L	latent heat of condensation of water
M_a	molecular wt., air
M_v	molecular wt., water
$n(T)$	gas concentration at temperature T
N	drop concentration
p	total pressure
R	gas constant
r	mixing ratio
r_o	initial mixing ratio
S	supersaturation
S_c	critical supersaturation
T	temperature
T_a	temperature in gas at surface of drop

Greek symbols

α thermal accommodation

β condensation coefficient

γ ratio of specific heat at constant pressure to
                       that at constant volume (air)

ϵ ratio of molecular wt. of water to that of air

ρ_s density of NaCl

APPENDIX C

CONDENSATION METHOD FOR HUMIDITY MEASUREMENT

IN THE UMR CLOUD SIMULATION CHAMBER

D.E. Hagen
Department of Physics

D.R. White
Department of Engineering Mechanics

D.J. Alofs
Department of Mechanical Engineering
and

Graduate Center for Cloud Physics Research
University of Missouri-Rolla
Rolla, MO 65401

ABSTRACT

The University of Missouri - Rolla has developed a cloud simulation facility for the study of various atmospheric cloud processes. The initial relative humidity of the air sample put into the cloud chamber is a key parameter in virtually any experiment and needs to be known accurately. This report describes how the cloud simulation chamber itself has been used as a condensation type hygrometer to calibrate the system's humidifier. Two distinct and physically different methods for inferring mixing ratio are used, one exploiting the sensitivity of aerosol activation to humidity, and the other exploiting the sensitivity of the rate of growth of cloud droplets to humidity. The two methods give agreement with each other to within a precision of one part per thousand in mixing ratio.

Key words: humidity measurement, mixing ratio, water vapor, aerosol activation, cloud drop growth, expansion cloud chamber.

1. Introduction

Several countries have developed facilities for accurately measuring humidity. Such a national facility ideally includes both an ultra stable humidity generator, and a primary standard for measuring relative humidity. The primary standard is used to calibrate the humidity generator, and the humidity generator is used to calibrate other portable instruments which have been sent to the national facility for calibration. The gravimetric hygrometer described by Wexler and Hyland [1] utilizes absorption of water vapor by a solid desiccant, and precision weighing of the absorbed water. The uncertainty is about plus or minus one part in a thousand for the measurement of mixing ratio (mass of water vapor per unit mass of dry gas). Gravimetric hygrometers are currently the primary standards in the United States [2], in Japan [3] and in the United Kingdom [4]. A chilled mirror condensation hygrometer [5] is utilized in France as a transfer humidity standard. This instrument is periodically calibrated at the National Bureau of Standards in the US and then returned to France for use as a standard in France. The accuracy is about plus and minus 0.03 °C in dew point. This corresponds to an uncertainty in mixing ratio of plus or minus 2 parts per thousand, or twice that of the gravimetric hygrometer. The chilled mirror hygrometer however, has the great advantage of portability.

The University of Missouri at Rolla has developed a cloud simulation facility, for studying the processes that occur in clouds in the atmosphere. Part of the facility is a humidifier, which has an air flow rate of 1 liter/sec, and which produces relative humidities close to 100 percent at temperatures which can be set to within 0.01 °C over the range 5 to 25 °C [6]. Another part of the facility is a cooled wall expansion cloud chamber, which produces a supersaturated environment so that water droplets can be grown on a sample of cloud condensation nuclei (CCN). A third part of the facility is the optical system used to observe the Mie scattering from the water droplets, thus determining the mean size of growing water droplets as a function of time. A fourth part of the facility is the aerosol generation system, used to supply the CCN sample to the simulation chamber. The cloud chamber, optical system, and aerosol generation system, and other components have been described by White et al [6].

This report describes how the cloud simulation chamber has been used as a condensation type hygrometer to calibrate the humidifier with a precision of one part per thousand in mixing ratio. An error analysis to determine whether the absolute accuracy is as good as the precision has not been made. Since an error analysis for the gravimetric hygrometer has been made [1], there is more confidence in the absolute accuracy of the gravimetric hygrometer than in our facility. It would therefore

be desireable to intercompare a gravimetric hygrometer to our facility, but this direct intercomparison wouldn't be feasible since neither facility is portable. It would be feasible to compare our humidity measurement technique to a portable hygrometer such as the chilled mirror instrument described by Merigourx and Cretinon [5] and our Center would welcome such an opportunity.

2. Expected Humidity From Humidifier

The humidifier consists of two columns each with 60 vertical glass rods, 0.7 cm diameter, spaced on alternate points of a 1.27 cm grid, and enclosed in an aluminum cylinder 16.5 cm inside diameter. Water flows downward on the glass surfaces, and air flows downward in the space between the glass rods. The two humidifier columns, each with an effective length of 89 cm, are connected is series with respect to the air flow. Thus the length of the humidifier is in effect 178 cm. The air flow rate is 1.0 liter/sec., and the water flow rate is 0.25 liter/sec.

The first concern addressed was whether the glass rods were isothermal over their length. As water evaporates at the rod surface the rods are cooled due to the latent heat absorbed. To calculate the amount of cooling an energy balance is performed. To humidify originally dry air the latent heat flux is 35.6 watts. This heat when supplied by the 0.25 liter/sec. liquid water flow produces only a 0.034 °C temperature drop in the

water. Thus the glass rods have essentially no axial temperature gradients.

The next concern is how to model the vapor diffusion in the humidifier. The problem is three dimensional, and would need to be solved numerically if one wished an accurate analysis. Instead a crude analysis was performed in which the three dimensional problem is approximated as a two dimensional problem for which an analytical solution exists. Specifically, the humidifier is modeled as a round tube, having the same hydraulic diameter as the cross section of the humidifier. The air velocity in the model tube equals the average air velocity in the actual humidifier (5.25 cm/sec), and the length of the model tube equals the total length of the two humidifier columns (178 cm). The wall of the model tube is wet and isothermal. The air enters the model tube dry and at the wall temperature. The outlet relative humidity from the model tube is sought.

The solution to the above idealization of the vapor diffusion in the humidifier has been given by Shah [7]. The hydraulic diameter is 4A/P, where A is the cross sectional area of the flow and P is the perimeter wetted by the flow. Applied to the humidifier, A is the area of a 16.5 cm circle minus the area of 60 circles of 0.7 cm diameter. P is the circumference of 60 circles 0.7 cm diameter. This gives an hydraulic diameter of 5.66 cm. The Reynolds number based on a 5.66 cm length and an

air velocity of 5.25 cm/sec is about 200, so the air flow is laminar. The Peclet number is about 115, so that vapor diffusion in the flow direction is small compared to that in the transverse direction. The 178 cm length divided by the 5.66 cm length and by the Peclet number is a non-dimensional quantity called x* by Shah. The mean outlet relative humidity, called $(1 - \theta_m)$ in Shah's analysis, is a function of only x^*. For our x^* (0.272) the predicted mean outlet relative humidity is 98.45 %, equivalent to a mean outlet dew point lower than the wall temperature by 0.256 °C. This result should be treated as a crude estimate. The resulting predicted dew point deficit of 0.256 °C is an order of magnitude estimate. It turns that the observed humidity deficit is 0.29 °C, so the agreement is better than one could reasonably expect. Shah also gives an analytical solution for the equivalent diffusion problem between parallel plates. If the humidifier is evaluated in terms of equivalent parallel plates, the predicted dew point deficit is about an order of magnitude smaller (i.e., about 0.03 °C).

3. Humidity Measurement In The UMR Cloud Simulation Chamber

The initial relative humidity in the chamber, prior to expansion, is a key parameter in virtually any experiment. Despite the care that has gone into sample humidification, this has proved to be a difficult parameter to fix experimentally, and we have had to enlist additional means over and above the

humidifier analysis given above in order to infer the humidity's value.

Two distinct and novel methods of inferring the initial mixing ratio from Mie scattering on a monodispersed cloud are described below. These have proved sufficiently accurate and reliable that we have adopted them in all subsequent experiments. The variable chosen to represent the initial water vapor content is mixing ratio, i.e. the number of grams of water vapor per gram of dry air and is denoted by r_o.

3.1 Experiment Description.

The experiment begins with a moist aerosol laden air sample at temperature T_o and pressure p_o. Usually T_o is near 20 °C and p_o is near 14.1 psi. The aerosol consists of NaCl particles of size near 0.025 μm radius and concentration near $100/cm^3$. The sample's initial relative humidity is typically near 83%. It is lowered below 100% by immediately raising the sample's temperature after it leaves the humidifier to avoid condensation loss of vapor (see [6]). At a relative humidity of 83%, the aerosol particles consist of very small (~0.05 μm) solution droplets instead of dry particles. The sample is expanded to give a cooling rate of 10°C/minute, and the resulting cloud is observed via Mie scattering of laser light to determine drop size as a function of time. The aerosol exerts a negligible influence on the measurements of interest here. At our smallest observable

drop size, 0.70 μm, a 10% change in the NaCl particle mass would only change the solution drop's equilibrium supersaturation ratio by 0.000006; an amount negligible in comparison to unity. Small variations in the critical supersaturation of the aerosol would have no appreciable effect on droplet growth rates.

3.2 Multiple Droplet Growth Rate Method

The condensational growth of water droplets is quite sensitive to humidity. Hence droplet growth rates can be used to give a measure of the air's water vapor content. In our method we take a small set of droplet growth rate data containing at least two growth rate measurements and covering a short period of time. This data set is analyzed using drop growth theory to extract two unknowns, mixing ratio and sticking coefficient (β). A whole experiment can be subdivided into numerous small data sets, and a separate determination of r_o made for each one. In each case the amount of water converted into the liquid state is accounted for in the determination of initial (before expansion) mixing ratio r_o. r_o should of course be constant.

The droplet growth rate equation [8] for the i-th droplet growth rate measurement can be written

$$r_o = \epsilon / [P_i e_s (T_i)^{-1} \{(a_i + \ell_i) \dot{a}_i / D_{eff} \rho_{sat,i} + S_i^* \}^{-1} - 1]^{-1}$$

(1)

$$+ (4/3) \pi N a_i^3 ,$$

with $\epsilon = .62197$, p is the total pressure, N is the droplet concentration per gram of dry air, e_s is water saturation vapor pressure, T is absolute temperature, a is the droplet radius, a is the droplet growth rate, D_{eff} is an effective diffusion coefficient (see [9]) for water vapor in air, ρ_{sat} is the saturation water vapor density over a flat surface, S^* is the equilibrium supersaturation ratio over a droplet of radius a, and

$$\ell = D_{eff} (\ell_\alpha LB/K R_v T + \ell_\beta/D) , \qquad (2)$$

$$\ell_\alpha = (1-\alpha/2)K(\gamma-1)(8\pi T/R_a)^{1/2}[\alpha p(\gamma+1)]^{-1} \qquad (3)$$

$$\ell_\beta = (1/\beta - 1/2)D(2\pi/R_v T)^{1/2} . \qquad (4)$$

Here D is the diffusion coefficient for water vapor in air, L is the latent heat of condensation for water, B is the slope of the e_s vs. temperature curve, K is the thermal conductivity of moist air, R_v is the gas constant for water vapor, R_a is the gas constant for dry air, α is the thermal accommodation coefficient (here we use $\alpha=1$), and γ is the specific heat ratio of moist air. The amount of water in the system is constant, so Eq. (1) should have the same value for all drop growth rate measurement points.

This fact can be used to eliminate the unknown β. Define a minimization parameter as:

$$\text{chisq} = \frac{\sum\limits_{i=1}^{I} \sum\limits_{j=1}^{i-1} (r_{oi} - r_{oj})^2 / [\delta(r_{oi} - r_{oj})]^2}{\sum\limits_{ij} [\delta(r_{oi} - r_{oj})]^{-2}} \qquad (5)$$

where $\delta(r_{oi} - r_{oj})$ denotes the uncertainty in the knowledge of $r_{oi} - r_{oj}$. This uncertainty is calculated based on a 0.05 μm uncertainty in "a", a 20% uncertainty in $\dot{a}$, and a 5% uncertainty in N. The condensation coefficient enters into chisq through ℓ. Since r_o is constant chisq should be zero or at least small. Using the computer routine STEPIT, β can be varied to minimize chisq. This yields a value for β which can be put back into Eq. (1) to get r_o. This process can be repeated for each data subset taken during the experiment to give multiple measurements of the same quantity r_o.

3.3 Cloud Arrival Time Method

During a given expansion, the cloud is observable soon after saturation (100% relative humidity) is reached, and this observation provides a good determination of the saturation event. The cloud droplets can be observed starting at 0.70 μm radius. The small time increment, on the order of one second, between saturation and first cloud observation, can be accounted

for by droplet growth modeling. For the special case of expansions using constant cooling rates (temperature is a linear function of time), this time increment is very insensitive to r_o. The method simply involves observing the cloud arrival time, subtracting the above time increment from this to determine the time at which the gas sample reacned 100% relative humidity, noting the gas temperature and pressure at this time (100% relative humidity), and finally calculating the mixing ratio r_o of the gas from this information.

This method is only applicable to experiments using constant cooling rates which make the above time increment independent of r_o. Also the method is applied only to experiments using monodispersed CCN aerosols and fairly fast expansion rates. These conditions lead to monodisperse clouds (all drops are the same size), and allow the use of Mie scattering of laser light as the drop sizing method [6].

The time increment between the 100% relative humidity point and the cloud first observation point is calculated from droplet growth theory, and does depend on sticking coefficient. However this particular situation involves freshly produced droplets, and fresh water surfaces are thought to have large sticking coefficients near unity [10]. The sticking coefficient results taken from the droplet growth rate method described above confirm this for the early stage of the cloud's lifetime. Hence in the

time increment calculation, a sticking coefficient of unity is assumed. The influence of sticking coefficient is modest here in any case. A change in sticking coefficient by a factor of 2 (or 5) leads to a change in r_o by an amount 0.000006 (or 0.000023).

The cloud arrival time method hasn't been optimized and therefore improvements could be achieved. For instance the influence of the sticking coefficient could be minimized by choosing a slower expansion rate and a more sharply monodispersed CCN aerosol. This would reduce the change in temperature, pressure, and humidity during the time interval during which the cloud drops grew to observable size.

3.4 Numerical Cloud Model Tests

As discussed above a numerical cloud model, which calculates gas thermodynamics and water droplet growth processes, is used in this analysis. For this we use the numerical model presented by Hagen [9]. This model has been successfully tested against older results in the literature [9] and against the NASA Analytic Simulator [11,12]. Anderson, Hallett, and Beesley [13] presented an extended solution to the droplet growth problem and gave an intercomparison among the leading droplet theories. They conclude that Carsten's [8] solution of the droplet growth problem is quite adequate. This is the solution on which our cloud model is based. Furthermore Anderson, et. al. [13] presented numerical results from their extended model for

numerous test cases. We calculated these cases with our model
and agreed with their results to within 2% for drop size.

4. Results

The experimental results from five different days of work are
given in Table I. The run number gives a unique identification
number for each experiment. The first six digits of the run
number give the date (month-day-year) on which the experiment was
performed. These experiments run from September 1986 to November
1987. The column labeled r_o(MDG) gives the values for mixing
ratio obtained from the multiple drop growth rate method. This
represents the average of repeated measurements of this quantity
during the course of the experiment. Since r_o represents the
initial value of mixing ratio, it is fixed and all of these
repeated measurements should yield the same value. σ(MGR)
denotes the standard deviation of the individual results around
the average and is a measure of experiment consistency. Note
that σ(MGR) is usually small, indicating good consistency between
the various measurements taken in a given run. r_o(CAT) denotes
the initial mixing ratio as determined by the cloud arrival time
method. Δr_o denotes the difference between the two methods, i.e.
$\Delta r_o = r_o$(CAT) $- r_o$(MGR). ΔT_h gives the difference between the
measured humidifier temperature and the humidified air sample's
dew point. Recall that the humidifier does not quite bring the
sample up to 100% relative humidity.

The average of the absolute difference between r_o(MDG) and r_o(CAT) is 0.000010, with standard deviation around the average of 0.000007. This average difference between the two methods corresponds to a difference of 0.012°C in dew point. Hence the two methods are in good agreement with each other. The average difference between measured humidifier temperature and dew point is 0.29°C, corresponding to a relative humidity of 98.1% for the air coming from the humidifier. This figure is in agreement with the rough estimate of expected humidifier performance under these conditions (0.26°C difference between humidifier temperature and dew point, or 98.45% relative humidity for air leaving the humidifier) that was given above.

5. Conclusion

The problem of determining the water vapor content of a gas sample is addressed using the condensational growth of airborne water droplets as the measurement tool. Two distinct methods are employed. One is based on multiple measurements of droplet growth rate; the other is based on the fact that cloud is observable almost immediately after the gas sample is brought through 100% relative humidity. These two quite different methods give good agreement with each other. The average difference in calculated initial mixing ratio is 0.000010 grams of water per gram of dry air (corresponding to about 8 parts in 10^4), with a standard deviation of 0.000007 gram/gram-air. This

corresponds to a dew point difference of 0.012°C. This agreement gives us substantial confidence in our determination of water vapor content.

6. Acknowledgment

References

[1]   Wexler, A., and R.W. Hyland.   The NBS standard hygrometer. In Humidity and Moisture, Wexler, ed., Vol. III, Reinhold Publ. (1965)

[2]   Hasegawa, S.   National basis of accuracy in humidity measurements.   In Moisture and Humidity, Instrument Society of America, Proc. 1985 Int'l Symp. on Moisture and Humidity, Washington, D.C., April, pg. 15-28 (1985).

[3]   Takahashi, C., and T. Inamatsu.   Construction of a gravimetric hygrometer.   In Moisture and Humidity, Instrument Society of America, Proc. 1985 Int'l Symp. on Moisture and Humidity, Washington, D.C., April, pg. 91-100 (1985).

[4]   Forton, A.G., and R.F. Pragnell.   "Development of the primary gravimetric hygrometer for the U.K. national humidity standard facility.   In Moisture and Humidity, Instrument Society of America, Proc. 1985 Int'l Symp. on Moisture and Humidity, Washington, D.C., April, pg. 79-89 (1985).

[5]   Merigoux, J., and B. Cretinon.   A transfer humidity standard for dew point temperatures in the range from -20°C and +60°C.   In Moisture and Humidity, Instrument Society of America, Proc. 1985 Int'l Symp. on Moisture and Humidity, Washington, D.C., April, pg. 401-410 (1985).

[6]   White, D.R., J.L. Kassner, J.C. Carstens, D.E. Hagen, J.L. Schmitt, D.J. Alofs, A.R. Hopkins, M.B. Trueblood, M.W. Alcorn, and W.L. Walker.   Rev. Sci. Instrum. 58:826 (1987).

[7]   Shah, R.K.   Thermal entry length solutions for the circular tube and parallel plates.   Proc. 3rd Natl. Heat Mass Transfer Conf., Indian Institute of Technol., Bombay, Vol. I, Paper No. HMT-11-75 (1975).

[8]   Carstens, J.C.   Adv. Colloid Interface Sci. 10:285 (1979).

[9]   Hagen, D.E.   A numerical cloud model for the support of laboratory experiment.   J. Appl. Meteor. 18:1035 (1979).

[10] Pruppacher, H.R., and J.D. Klett.   Microphysics of clouds and precipitation.   D. Reidel, Boston (1978).

[11] Plooster, M. Atmospheric cloud physics laboratory simulation system; mathematical description. Report under NASA contract NAS8-32668 (1979).

[12] Plooster, M. Atmospheric cloud physics laboratory simulation system; users guide. Report under contract NAS8-32668 (1979).

[13] Anderson, B.J., J. Hallett, and M. Beesley. An extended classical solution of the droplet growth problem. NTIS #NASA TM-82392 (1981).

TABLE I

RUN	$r_O(MGR)$	$\sigma(MGR)$	$r_O(CAT)$	Δr_O
091086.04	.012582	.000008	.012591	.000009
091086.05	.012574	.000012	.012550	-.000024
091086.06	.012580	.000022	.012570	-.000010
091086.07	.012605	.000005	.012615	.000010
111886.A1	.012618	.000010	.012630	.000012
111886.A3	.012733	.000007	.012752	.000019
111886.A4	.012551	.000010	.012565	.000014
121786.01	.012480	.000005	.012488	.000008
121786.02	.012483	.000007	.012485	.000002
121786.03	.012503	.000006	.012512	.000009
121786.04	.012521	.000013	.012533	.000012
121786.05	.012509	.000006	.012519	.000010
121786.06	.012520	.000008	.012524	.000004
121786.07	.012530	.000011	.012526	-.000004
121786.08	.012523	.000008	.012541	.000018
121786.09	.012525	.000012	.012523	-.000002
121786.10	.012528	.000045	.012524	-.000004
080787.01	.012668	.000018	.012689	.000021
100687.01	.012510	.000008	.012506	-.000004

APPENDIX D

HYDRATION PROPERTIES OF COMBUSTION AEROSOLS

D.E. Hagen*, M.B. Trueblood, and D.R. White**

Department of Physics, Department of Mechanical Engineering**,

and Graduate Center for Cloud Physics Research

University of Missouri-Rolla

Rolla, MO 65401

*Send proofs to D.E. Hagen

ABSTRACT

There has been considerable recent interest in the hydration properties of combustion aerosols. Both their warm cloud condensation behavior and ice nucleating ability have important atmospheric implications. At UMR we have a substantial cloud simulation facility designed for the laboratory study of atmospheric processes under realistic conditions (i.e., temperature, pressure, and supersaturation) and time scales. A combustion aerosol capability has been added to this facility. We can generate a variety of combustion aerosols, under controlled and observed conditions, characterize and shape (modify their size distribution) these aerosols, and then examine their hydration behavior under either warm or cold conditions. Here we describe this combustion system and present results (size distributions and critical supersaturation distributions) for aerosols resulting from the combustion of various liquid fuels. The hydration of these aerosols is found to obey Kohler theory, and soluble mass fraction results from this analysis are shown.

INTRODUCTION

Carbon aerosols have long been recognized as one of the important constituents of the overall atmospheric aerosol (Pruppacher and Klett, 1978; Hidy, 1984; Novakov, 1979; Appel, et al., 1983). A major portion of atmospheric particles found in both urban and rural areas consists of carbonaceous material derived from both biogenic and anthropogenic sources. This aerosol has implications to atmospheric chemistry, atmospheric physics, climate, public health, etc. The hydration properties of carbonaceous aerosols are becoming increasingly important (Ogren and Charlson, 1983; Malone, et al., 1986; Penner, 1986). They influence the evolution and residence time for these aerosols in the atmosphere. Both their warm cloud condensation behavior and ice nucleating ability have important atmospheric implications.

At UMR we have a substantial cloud simulation facility (White, et al., 1987) designed for the laboratory study of atmospheric processes (e.g., nucleation, droplet growth, scavenging, coagulation, ...) under realistic conditions (i.e., temperature, pressure, and supersaturation) and time scales. A combustion aerosol capability has recently been added to this facility. In this paper we describe the facility, exhibit size distributions and critical supersaturation distributions for some combustion aerosols, and analyze these results in terms of Kohler theory.

FACILITY

The Graduate Center for Cloud Physics Research at UMR has

developed a cloud simulation facility to study phenomena occurring in terrestrial clouds and fogs. The facility consists of a pair of precision cooled-wall expansion chambers along with extensive supporting equipment. The facility is supported by a fully implemented aerosol laboratory which routinely produces well-characterized condensation nuclei and ice nuclei upon demand. The aerosol laboratory contains extensive instrumentation designed to both shape and measure the size distribution and nucleating characteristics of the generated aerosol. These characteristics can be examined under well-controlled static and/or dynamic conditions. The cloud simulation facility also includes a humidifier to bring an air sample to a known humidity before it is put into the cloud chamber. Full details of the simulation facility are given elsewhere (White, et al., 1987).

A recent addition to this facility has been the capability to treat combustion aerosols. This capability can be divided into parts: combustion aerosol generators (burners) and a combustion vessel designed to hold the generator and capture the resulting aerosol for delivery to the rest of the aerosol laboratory instrumentation.

Several types of combustion aerosol generators (burners) are in use. The simplest is just a kerosene lantern, of the type used for camping. It has the advantage of being inexpensive and extremely stable. It has the disadvantage of having the fuel tank integrated into the burner assembly which prevents control of the fuel temperature as it is fed to the burner and presents

safety problems. Furthermore the fuel is limited to kerosene. A

second aerosol generator is a liquid fuel blowtorch (torch 1),

originally designed to burn white-gas with a horizontal flame.

This unit was modified to separate the burner itself from the

fuel tank which allows the tank to be outside the combustion

vessel and allows operator control of the fuel vaporization

temperature via an electrical heating collar and temperature

controller. A shroud was built around the burner to allow better

control of the combustion air. A third burner is an in-house

constructed blowtorch (torch 2) featuring temperature controlled

fuel and air supplies, a vertical flame, and a combustion region

which can produce either a laminar fuel/air flow (diffusion

flame) or a very turbulent fuel/air mixing.

The combustion vessel is a cylindrical (44 cm diameter X 61

cm height), steel bell jar, which was originally part of a vacuum

system. It features an observation window to view the flame,

provisions to externally control the torch's fuel needle valve,

and provisions for electrical, fuel, combustion air, and dilution

air feed throughs. The bell jar can be raised about 60 cm by

means of a counterbalanced hoist, allowing convenient access to

the torch for routine maintenance and/or torch exchanging. The

combustion exhaust gases are mostly vented outdoors with a small

fraction being diverted into the aerosol sampling/characterizing

instruments.

A schematic diagram of the instrumentation is shown in Fig.

1. The EAC (electric aerosol classifier) is an electric mobility

device which charges the aerosol and uses mobility to select one

aerosol size to pass. The EAC was developed by Liu and Pui (1974) and by Knutsen and Whitby (1975) and is commercially available (Model 3071, TSI, St Paul, MN). We use it to extract a monodisperse slice of the aerosol. The AGCFD is an alternating gradient continuous flow thermal diffusion cloud chamber (Hoppel, et al., 1979a,b). It exposes the aerosol to a fixed and high supersaturation that is sufficient to activate all cloud condensation nuclei. The OPC (optical particle counter) sizes and counts the resulting cloud droplets. The CFD (continuous flow thermal diffusion cloud chamber) exposes the aerosol to a certain operating supersaturation, the value of which is determined by the operator and is stepped through a series of values as the experiment proceeds (Alofs, 1978; Alofs, et al., 1979; Alofs and Trueblood, 1981). Aerosol particles with a critical supersaturation at or below the operating supersaturation will grow to detectable size during their transit through the CFD. The left leg of the system is used for the size distribution measurement and the right leg is used for the critical supersaturation spectrum measurement.

METHOD

In these experiments various fuels were burned in various burners. The resulting combustion aerosols were collected in the combustion vessel and then sent through the aerosol laboratory instrumentation for examination. In particular the aerosol's size distribution (concentration vs particle size) and critical supersaturation spectrum (the supersaturation which is just sufficient to activate the particle into a freely growing drop vs

particle size) were studied. The EAC downstream from the combustion vessel (Fig. 1) performs the task of sizing the aerosol. A small number of multiply charged particles may be passed and need to be accounted for. These aerosols are fairly small, in the 0.01 μm to 0.10 μm diameter range. The aerosols are exposed to substantial humidity in the combustion vessel and during their transit to the EAC. At the EAC the aerosol is mixed with relatively dry laboratory sheath air. This humidification and dehumidification cycle tends to result in a more spherical particle (Penner, 1986; Goldsmith, et al., 1966) and gives meaning to the particle sizing via mobility analysis. The resulting monodisperse aerosol is then sent to either the AGCFD-OPC facility for size distribution analysis, or to the CFD-OPC facility for critical supersaturation analysis. These techniques are described elsewhere (Alofs, et al., 1979; Alofs and Trueblood, 1981).

RESULTS

The aerosol particles produced by our burners are predominantly in the 0.01 μm to 0.1 μm diameter size range. The size distribution for the combustion aerosol from the kerosene lamp is shown in Fig. 2A. Fig. 2B shows the aerosol size distribution for the combustion of white gas (Coleman Camp Stove Fuel, Coleman Co., Wichita KS) in the horizontal flame blowtorch (torch 1). Fig. 2C shows the aerosol size distribution for the combustion of ethanol in the vertical flame torch (torch 2). The size distributions consist of concentration vs size information. Here we report the concentration of the aerosol after it has

passed through the EAC. This is reduced from the concentration at the exit port of the combustion vessel because of need to charge the particles (with probability less than unity) before the aerosol is passed through the EAC. Since this probability (size dependent) is known (Alofs and Balakumar, 1982) the initial concentrations can be calculated if needed.

Two different size distributions are shown for the kerosene lamp corresponding to otherwise identical experiments done on two different days (Fig. 2A). This indicates the reproducibility of the lamp aerosol. The mean size is about 0.039 μm with a sigma of .021 μm. Fig. 2B shows two size distributions for torch 1 burning white gas, again for two different experiments. In the experiment designated by the triangles an additional stage of dilution was employed. For this torch and white gas we find a mean size of 0.031 μm and a Gaussian sigma of .024 μm. Hence we find a size distribution that is somewhat smaller in size and of about the same width as for the case of kerosene in the lamp. Fig. 2C shows two size distributions for torch 2 burning ethanol. Here the mean size is about 0.027 μm while the sigma is about .013 μm. Two different flame conditions are involved here. For the circle data the flame was half blue and half yellow; for the triangle data the flame was all blue. Both runs used the same airflows, but the fuel exit oriface was smaller for the case of the all blue flame (triangles). Thus one sees that the flame condition can change the aerosol's size distribution.

The aerosol's ability to hydrate is given by its critical supersaturation (the supersaturation needed to activate the

particle, i.e., convert it into a freely growing drop). Critical supersaturation spectra (critical supersaturation vs particle size) are given in Fig. 3A for the aerosol from white gas burning in torch 1, and in Fig. 3B for the aerosol from ethanol burning in torch 2. Fig. 3A shows that the white gas combustion aerosol behaves much like a salt obeying Kohler (Pruppacher and Klett, 1981) theory. For reference we include (dotted line) the critical supersaturation spectrum for NaCl. A line through the combustion aerosol data is almost parallel to the NaCl line but lies much higher in supersaturation. Hence the combustion aerosol is much harder to activate. The scatter in the combustion aerosol data is attributed to difficulties in maintaining a stable flame in the torch during the measurements. Fig. 3B shows the critical supersaturation spectrum for ethanol combustion in torch 2. The circles again refer to half blue and half yellow flame conditions; the triangles refer to all blue flame conditions. This gives a measure of the impact of flame conditions on critical supersaturation. A line through the circle data is again parallel to that for NaCl indicating a Kohler type of behavior. The critical supersaturation spectrum for the ethanol combustion aerosol is surprisingly similar to that from white gas. Since ethanol is a cleaner fuel we had expected to obtain higher critical supersaturations for ethanol.

ANALYSIS

Combustion processes are known to produce carbon aerosols containing water soluble impurities, e.g., sulfuric acid (Chang, et al., 1979; Malone, et al., 1986; Ogren and Charlson, 1983).

An analysis was performed on this critical supersaturation data using Kohler theory (Pruppacher and Klett, 1978) in order to determine the amount of soluble material present. For the aerosol resulting from white gas combustion we assume that the soluble material is sulfuric acid, since the fuel contains sulfur as an impurity, and this combustion process can produce sulfuric acid on the resulting aerosol (Chang, et al., 1979; Ogren and Charlson, 1983). For the ethanol aerosol we assume that the soluble material is nitric acid, which results from nitrogen in the air during the combustion process.

Standard Kohler theory (Pruppacher and Klett, 1978) was used in the analysis. The analysis was performed twice corresponding to two different assumptions concerning the relationship between the carbon particle and the growing solution droplet. Method 1 assumes that the carbon particle is not immersed within the drop, while method 2 assumes that it is completely immersed. Kohler theory gives the equilibrium supersaturation for a solution drop containing a fixed amount of solute (Pruppacher and Klett, 1978, page 142 for method 1 and page 146 for method 2). The maximum of this function is the critical supersaturation, and it depends on the solute mass. We simply invert this relation to determine solute mass from the measured critical supersaturation. The results are shown for white gas in Table I, and for ethanol in Table II. Here D_p denotes the particle diameter as given by the EAC, S_c is the critical supersaturation (taken from the straight line through our data), m_s is the solute mass, and R is the ratio of solute mass to total particle mass. $\langle R \rangle$ denotes the value of

R averaged over the size range shown, and sigma is the standard deviation about this average. A value of 2.0 g/cm^3 was used for the density of carbon (amorphous). We find the amount of soluble material to be about 4% of the total particle mass. There is only a small variation with particle size, fuel type, and theory (methods 1 or 2) used to do the analysis.

CONCLUSIONS

A laboratory system for the study of the hydration properties of combustion aerosols is described. The combustion aerosol instrumentation is a subsystem for the cloud simulation facility at UMR. Size distributions are presented for several fuels and aerosol generators (burners). The particle sizes are concentrated in the region 0.01 μm to 0.1 μm diameter. Critical supersaturation spectra are presented for the aerosols from the fuels white gas and ethanol. The combustion aerosols are found to exhibit a behavior following classical Kohler theory, but with critical supersaturations considerably higher than that for NaCl. This however is a result for freshly prepared aerosols. Aging effects could modify this result. These high critical supersaturations would make it unlikely that the smaller carbon particles would be able to serve as condensation nuclei in the atmosphere. This would enhance the possibility that they would pass through the condensation level and reach levels where ice nucleation would become important, therefore their ice nucleating ability should be studied.

A calculation was performed to determine the amount of solute needed to give these particles their observed critical

supersaturations, assuming Kohler theory behavior. It was found under various assumptions that about 4% of the particles mass needed to be solute.

REFERENCES

Alofs, D.J. (1978). J. Appl. Meteor. 17:1286.

Alofs, D.J., Trueblood, M.B., White, D.R., and Behr, V.L. (1979). J. Appl. Meteor. 18:1106.

Alofs, D.J. and Trueblood, M.B. (1981). J. Rech. Atmos. 15:219.

Alofs, D.J., and Balakumar, P. (1982). J. Aerosol Sci. 13:513.

Appel, B.R., Tokiwa, Y., and Kothny, E.L. (1983). Atmos. Environ. 17:1787.

Chang, S.G., Brodzinsky, R., Toossi, R., Markowitz, S.S., and Novakov, T. (1979). in Carbonaceous Particles in the Atmosphere, p. 122, (T. Novakov, ed.), NTIS #LBL-9037, Berkeley CA.

Goldsmith, P., May, F.G., and Wiffen, R.D. (1966). Nature 210:475

Hidy, G.M. (1984). Aerosols, An Industrial and Environmental Science. Academic, New York.

Hoppel, W.A., Twomey, S., and Wojciechowski, T.A. (1979a). J. Aerosol Sci. 10:369.

Hoppel, W.A., Twomey, S., and Wojciechowski, T.A. (1979b). J. Aerosol Sci. 11:421.

Knutson, E.O. and Whitby, K.T. (1975). J. Aerosol Sci. 6:443.

Liu, B.Y.H. and Pui, D.Y.H. (1974). J. Colloid Interface Sci. 47:155.

Malone, R.C., Auer, L.H., Glatzmaier, G.A., and Wood, M.C. (1986). J. Geophys. Res. 91:1039.

Novakov, T., ed. (1979). Carbonaceous Particles in the Atmosphere, NTIS LBL-9037, Berkeley CA.

Ogren, J.A. and Charlson, R.J. (1983). Tellus B35:241.

Penner, J. (1986). Nature 324:222.

Pruppacher, H.R., and Klett, J.D. (1978). Microphysics of Clouds and Precipitation, D. Reidel, Boston.

White, D.R., Kassner, J.L., Carstens, J.C., Hagen, D.E., Schmitt, J.L., Alofs, D.J., Hopkins, A.R., Trueblood, M.B., Alcorn, M.W., Walker, W.L. (1987). Rev. Sci. Instrum. 58:826.

FIGURE CAPTIONS

1. Schematic diagram of the combustion aerosol facility.

2. Combustion aerosol size distributions: (A) from kerosene burned in lamp, (B) from white gas burned in torch 1, (C) from ethanol burned in torch 2.

3. Combustion aerosol *critical supersaturation* spectra for: (A) white gas burned in torch 1 (the dashed line is the critical supersaturation spectrum for a NaCl aerosol), (B) ethanol burned in torch 2.

TABLE I

COMBUSTION (WHITE GAS) AEROSOL
SOLUBLE MASS FRACTION

D_p (micron)	.013	.02	.03	.06	.10
S_c (%)	11.43	6.55	3.87	1.58	.816
$m_{s1} (10^{-18}g)$	.159	.537	1.58	9.44	34.6
R_1	.069	.065	.056	.042	.033
$m_{s2} (10^{-18}g)$	.0784	.311	1.05	7.41	28.1
R_2	.034	.037	.037	.033	.027

$$\langle R_1 \rangle = .053 \qquad \langle R_2 \rangle = .034$$

$$\sigma = .015 \qquad \sigma = .004$$

TABLE II

COMBUSTION (ETHANOL) AEROSOL

SOLUBLE MASS FRACTION

D_p (micron)	.013	.02	.03	.06	.10
S_c (%)	12.33	6.73	3.80	1.434	.699
$m_{s1}(10^{-18}g)$	.108	.366	1.14	7.93	32.9
R_1	.048	.044	.041	.035	.032
$m_2(10^{-18}g)$	.0370	.192	.763	6.59	29.8
R_2	.020	.028	.033	.036	.035

$$\langle R_1 \rangle = .040 \qquad \langle R_2 \rangle = .030$$

$$\sigma = .007 \qquad \sigma = .007$$

Fig 1

Fig 2

PARTICLE DIAMETER, D_p (μm)

SUPERSATURATION, S (%)

(A)

(B)
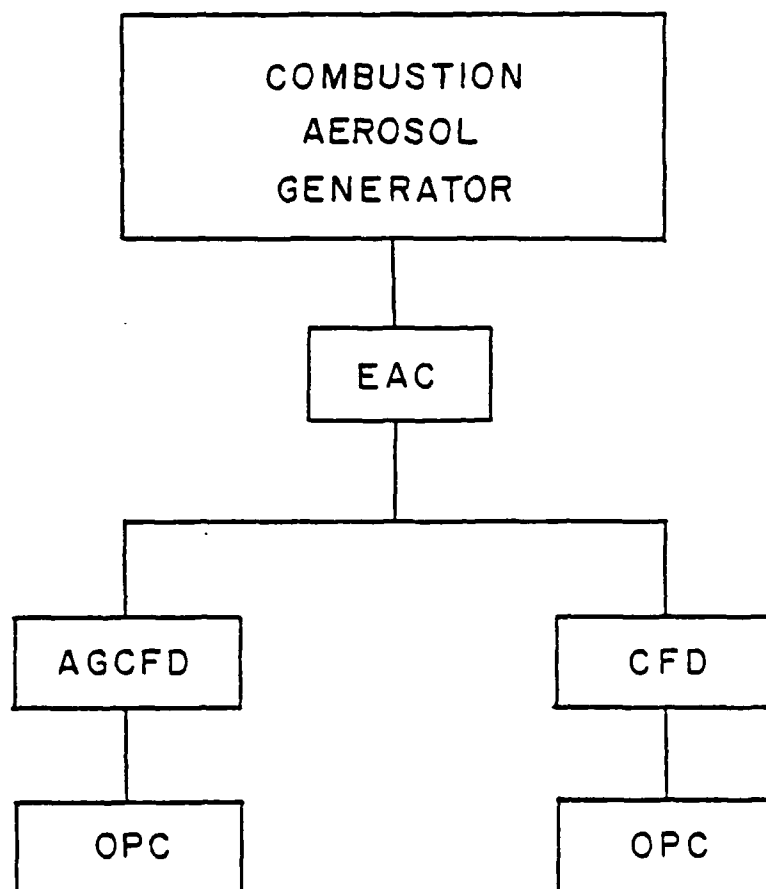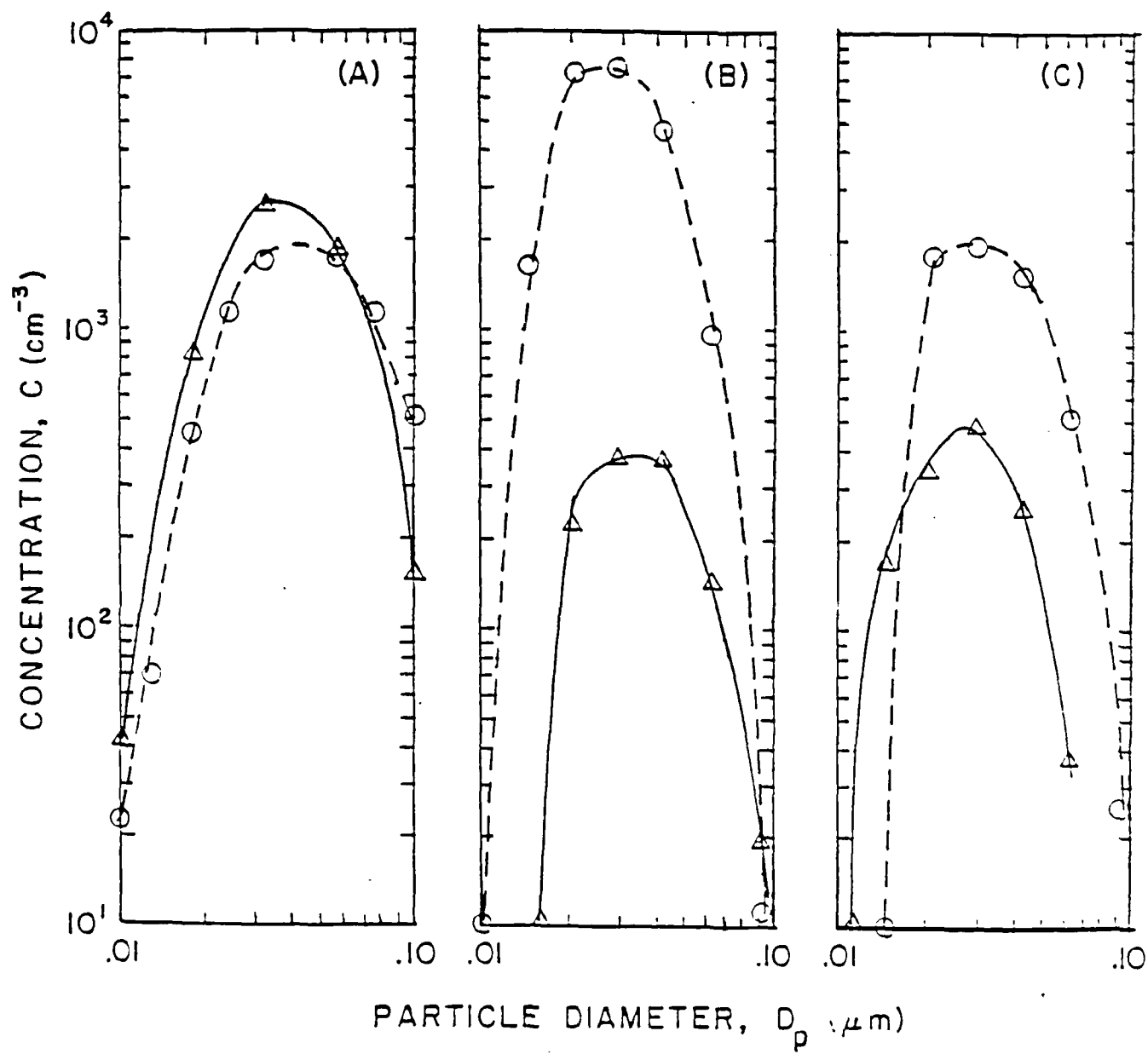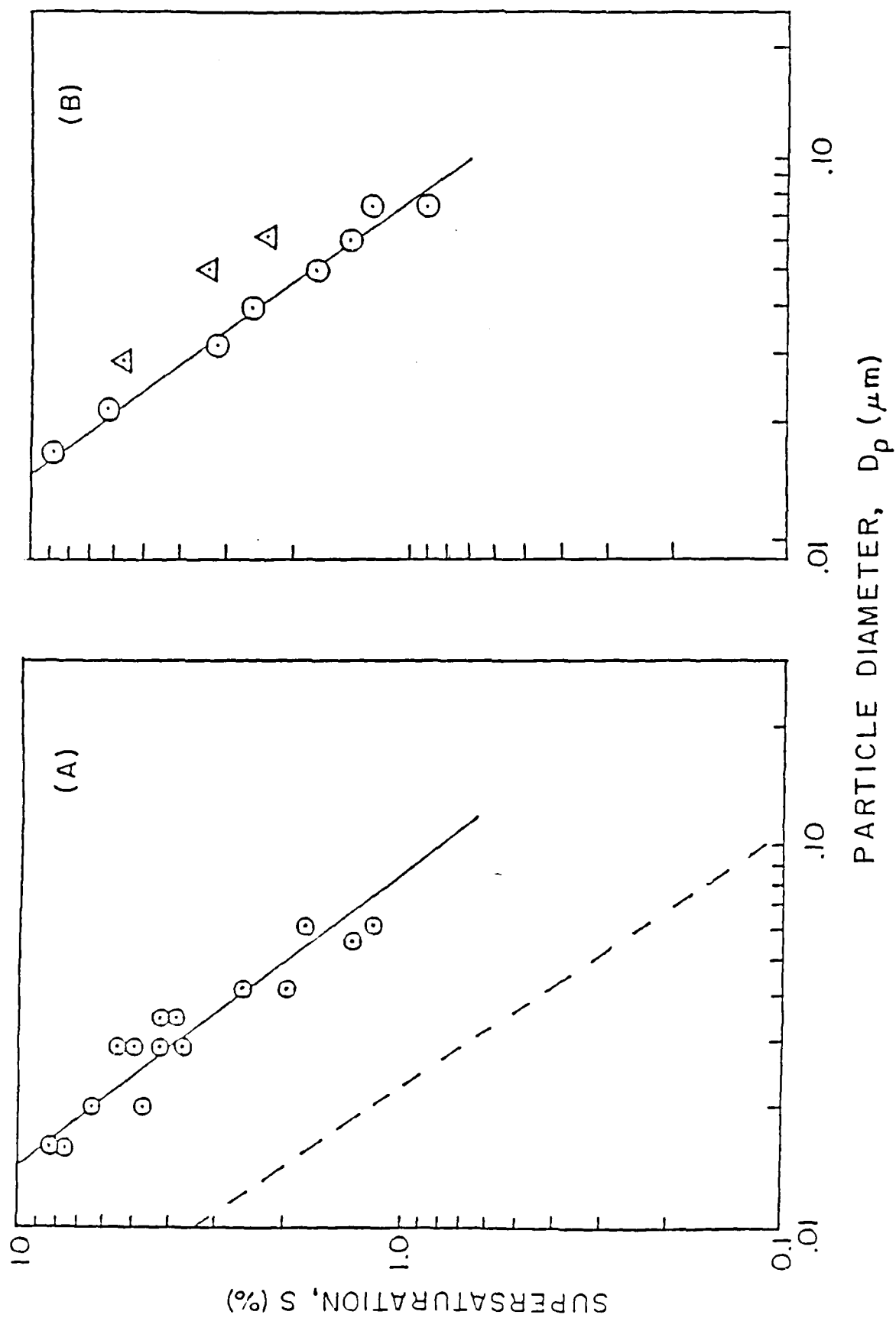
Fig 3

APPENDIX E

MODEL OF DROP GROWTH UNDER CONDITIONS OF PARTIAL
CONTAMINANT COVERAGE OF DROP SURFACE

Consider a supersaturated atmosphere with a component of contaminant. Let us suppose it to be insoluble in water and to reside on the water surface, e.g. insoluble surfactant. We want to look at a rate of coverage for cloud drops, and for simplicity we consider a monodisperse cloud.

This constituent diffuses to the surface of the growing drop and, we suppose that the contaminant molecule sticks to the drop surface only if it encounters a surface element which is not covered; otherwise it bounces off (Derjaguin, B.V., 1971: Aerosol Sci., 2, 261).

A similar assumption adapted from Dickenson's "hard disk" model (Dickenson, E., 1978: J. Coll. Int. Sci., 63, 461) is that the vapor molecules bounce off that portion of the surface which is already covered, i.e., off the effective disk area assigned to the surface contaminant, and otherwise stick with a coefficient β_0 which we here take to be unity. A pivotal parameter in this model is the effective hydrophobic area of the contaminant molecule which resides on the drop surface. It can range from about 20 A^2 to about 110 A^2 depending on orientation (Gill et al., 1983: Rev. Geophys. Space Phys., 21, 903). Furthermore, as coverage increases, more and more of the uncovered liquid area becomes inaccessible to incoming molecules due to the non-zero

disk radius.

Drop growth is described by the standard theory (e.g. Carstens, J. 1979: Adv. Coll. Int. Sci., 10, 285). The flux of surface contaminant to a growing drop, of instantaneous radius a, is given by the usual matching of diffusive and kinetic terms

$$\beta_o \frac{\bar{v}}{4} (\rho_\infty - \rho_{eq}) \frac{4\pi a^2 - N_S \pi a_s^2}{4\pi a^2} = D_N n M \frac{dx}{dr} \bigg|_a \qquad (1)$$

where β_o is the condensation coefficient of pure water, $\bar{v}$ the average molecular speed of contaminant molecule, ρ_∞ the ambient density of contaminant, ρ_{eq} its equilibrium density corresponding to the coverage, πa_s^2 the effective hydrophobic area of contaminant molecule, D_N the bulk diffusion coefficient (in air), n the molar gas concentration, N_S, the number of contaminant molecules on a drop, M the contaminant molecular weight, and x the contaminant mole fraction. Note that the term

$$\rho_S = \frac{4\pi a^2 - N_S \pi a_s^2}{4\pi a^2} = 1 - \frac{N_S}{4} \left(\frac{a_s}{a}\right)^2 \qquad (2)$$

represents the effective condensation coefficient associated with partial coverage. Quasi-steady state is assumed, with the profile

$$x(r) = x_\infty - \frac{a}{r} \frac{x_\infty - x_{eq}}{1 + \beta_S \ell_o/a} \qquad (3)$$

where the length parameter is given by $\ell_o = 4D_N/\bar{v}$.

The balance between contaminant vapor and drop coverage is given approximately by:

$$4\pi a^2 \, D_N n M \left. \frac{dx}{dr}\right|_a \frac{n_o}{g} = -\frac{d}{dt}\left(\frac{\rho}{\rho_g}\right) \tag{4}$$

where n_o is the drop concentration, ρ_g the dry air density, and ρ/ρ_g the contaminant mixing ratio. Because this calculation is meant only to test parameters and show trends, rather than secure quantitative accuracy, we will neglect the effect of air expansion and rewrite (4) in the simple form

$$4\pi a^2 \, D_N \left. \frac{d\rho}{dr}\right|_a \cong -\frac{1}{n_o}\frac{d\rho_\infty}{dt} \tag{5}$$

or, using the steady state profile,

$$-\frac{1}{n_o}\frac{d\rho_\infty}{dt} = 4\pi a \, D_N \frac{\rho_\infty - \rho_{rq}}{1 + \beta_S \ell_o/a} \tag{6}$$

At this point ρ_{eq} can be evaluated from the Langmuir isotherm,

$$\text{surface coverage} = \frac{\eta \, \rho_{eq}}{1 + \eta \rho_{eq}} \tag{7}$$

where η is a constant equal to the ratio of adsorption and desorption rates for a given surface. Solving for ρ_{eq} and substituting into (6) yields:

$$\frac{dN_S}{dt} = 4\pi a \ D_N \ \frac{n_o\left(\frac{N_o}{n_s} - N_S\right) - \frac{N_A}{M_S} \frac{1}{\eta} \frac{1-\beta_S}{\beta_S}}{1 + \frac{\ell_o/a}{\beta_S}} \tag{8}$$

where N_A is Avagadro's number. Equation (8) describes the rate at which the contaminant covers a drop of instantaneous radius a. It, along with the usual equation for drop growth, provides the description afforded by the "hard disk" model.

The figure shows some typical results for Cetyl alcohol. Here an updraft of about 3.4 m/sec. (starting at 20° and 1000 mb) produces growth on monodisperse NaCl nuclei ($100/cm^3$, dry radius .025 micron) which is retarded by the presence of Cetyl Alcohol vapor. Arrows show drop radii. Data on Cetyl alcohol is taken from Derjaguin et al., 1966: J. Coll. Int. Sci., 22, 45, including the saturation concentration 3.45 x 10" molecules/cm^3. In these calculations the effective surface coverage πa^2_s per surface molecule is based upon a value of $a_s = 3$ Å. The role of surfactant concentration is clear from these calculations. Even at 1/10 saturation (▣) the role of surfactant in retarding growth is non-negligible. (Beta is the condensation coefficient of water.)
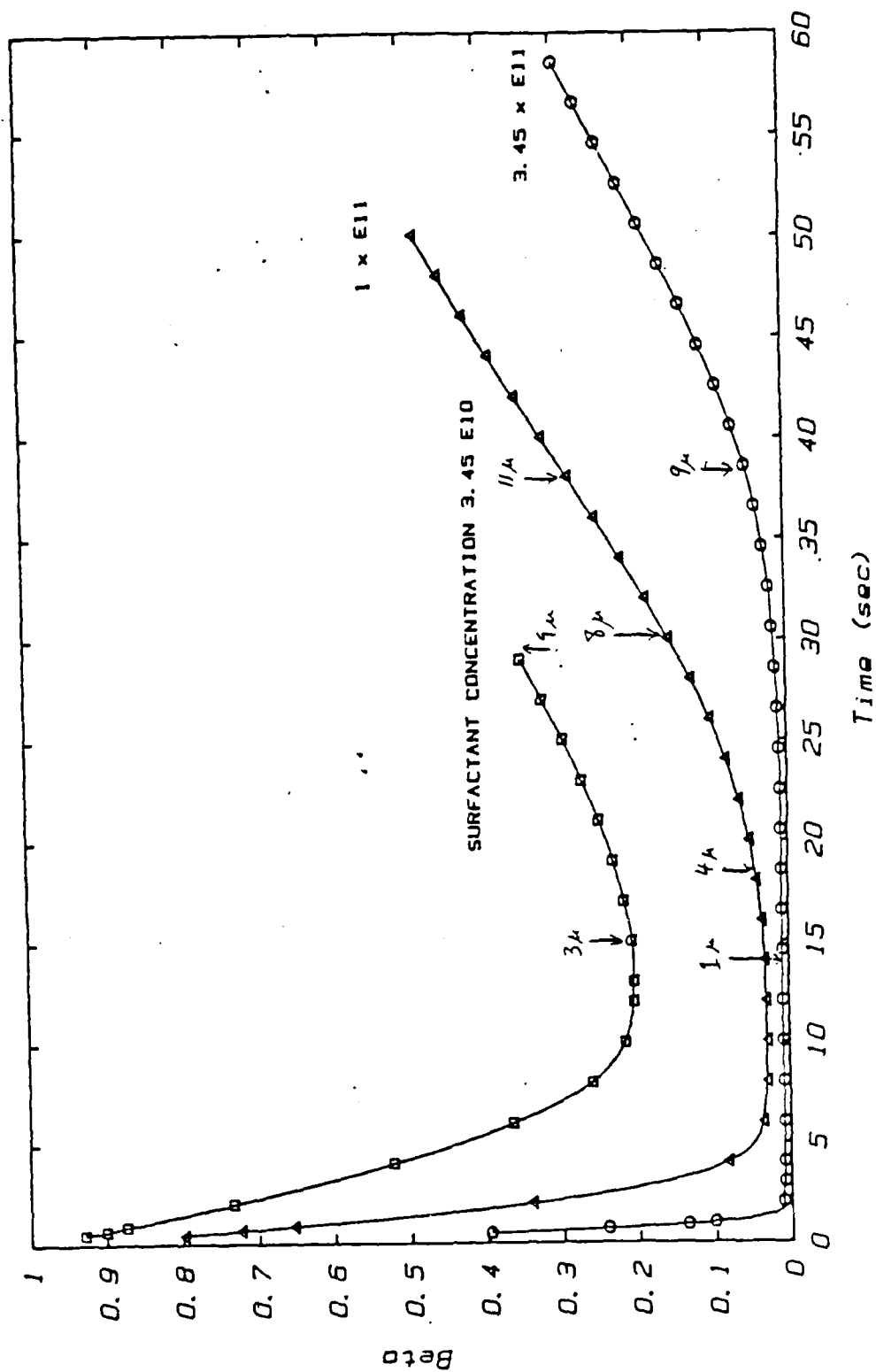
BETA vs TIME

END

DATE

FILMED

6- 1988

DTIC